

UNIVERSITÀ DEGLI STUDI DI NAPOLI

“Federico II”



FACOLTÀ DI SCIENZE MATEMATICHE, FISICHE E NATURALI

Dottorato di Ricerca in Scienze Chimiche XXIV Ciclo

**ORGANIC AND/OR METALLOORGANIC FUNCTIONAL MOLECULES AND THEIR
POLYMERS FOR APPLICATIONS IN ELECTRONICS AND PHOTONICS.**

Laura Ricciotti

A DISSERTATION PRESENTED TO THE UNIVERSITY OF NAPLES “FEDERICO II” IN
CANDIDACY FOR THE DEGREE OF DOCTOR OF PHILOSOPHY

Tutor

Prof. Antonio Roviello

Supervisor

Prof. Claudio De Rosa

Session 2010-2011

ABSTRACT

Organic materials have a tremendous potential to transform the world of circuit, display communication technology and renewable energy in near future. In fact organic materials have attracted much interest as possible inexpensive and flexible alternatives to inorganic devices.

The aim of this work was the synthesis and characterization of different classes of organic semiconducting materials for possible applications as active layer in electronic and photonic devices.

Several synthetic strategies have been developed and promising classes of p and n-type organic semiconductors have been prepared. As p-type materials, polythiophenes 3-substituted by alkoxyphenilic and alkeneoxyphenilic groups were synthesized by adapting a synthetic methodology previously reported in the literature [44], based on oxidative coupling of thiophene monomers using vanadyl acetylacetonate ($\text{VO}(\text{acac})_2$) complex as catalyst. In this way, using a very simple and inexpensive procedure we have obtained regioregular polythiophenes with over 90% HT content. This promising materials were successfully employed as active layers in the field of sensor devices for VOCs detection.

Successively, we have developed a new synthetic procedure for obtaining poly[3-(4-alkoxyphenyl)thiophene]s with regioregularity similar to that obtained by McCullough and Rieke methods in the synthesis of poly-3-alkylthiophenes, in order to use this class of materials in a broader field of applications in organic electronics. This novel synthetic methodology, that keeps simplicity and cheapness of the method based on oxidative catalysis using $\text{VO}(\text{acac})_2$ complex, allows to prepare poly[3-(4-alkoxyphenyl)thiophene]s

by oxidative catalysis using different Cu(II) complexes with very high regioselectivity, up to 99% of HT content and represents an interesting alternative to the more expensive classical procedures for the synthesis of poly-3-substituted thiophenes. Remarkable potentialities of highly regioselective poly[3-(4-alkoxyphenyl)thiophene]s have emerged from preliminary FET measurements, that have shown hole mobility up to $1.0 \cdot 10^{-4} \text{ cm}^2 \text{ V}^{-1} \text{ s}^{-1}$ and a high stability even when device operated in air.

For what concerns the developing of new n-type semiconductors, we have synthesized PDI derivatives functionalized at the imide nitrogen with a thiazole and triazole groups. Using the new PDI derivatives as active materials in OTFT devices, we have achieved air stable electron mobility up to $1.6 \cdot 10^{-2} \text{ cm}^2 \text{ volt}^{-1} \text{ sec}^{-1}$.

Finally we have investigated the suitability of one of the synthesized highly regioselective polythiophene, PT8 and one thiazole derivative of PDI, TDZ-C7 as possible, respectively, donor and acceptor materials in a heterojunction solar cell. Preliminary analysis were carried out through cyclic voltammetry (CV) in combination with UV-Vis optical absorption and photoluminescence emissions. The low bandgap of PT8 ($\sim 1.6 \text{ eV}$), its very stable HOMO energy (-5.55 eV) along with a favorable band offset of PT8 and TDZ-C7 and quenching of the photoluminescence of the latter upon mixing with the former, make this couple of materials excellent candidates to assemble photovoltaic cells.

RINGRAZIAMENTI

Alla fine di questo lungo ed intenso percorso formativo, vorrei ringraziare il mio Tutore Prof. Antonio Roviello per la sua costante presenza ed il grande supporto a tutta l'attività sperimentale.

Ringrazio il Prof. Roberto Centore per il suo grande contributo ed il mio relatore Prof. Claudio De Rosa per la sua grande disponibilità.

Un ringraziamento particolare va ai miei colleghi Antonio Carella e Fabio Borbone che mi hanno costantemente aiutato durante la dura attività di laboratorio, sempre con grande disponibilità. In particolare Antonio mi è stato di grande supporto anche per la stesura della tesi.

Ringrazio il Prof. Ugo Caruso sempre ben disposto a dare saggi consigli ed intervenire tempestivamente in alcuni momenti critici dell'attività sperimentale.

Ringrazio il Dr. Antonio Cassinese ed il Dr. Mario Barra del Dipartimento di Fisica, "Università Federico II" di Napoli per la fondamentale ed assidua collaborazione in tutta l'attività di ricerca.

Ringrazio il Prof. Bruno Pignataro ed il Dr. Sebastiano Cataldo del Dipartimento di Chimica "S. Cannizzaro" Università di Palermo per la preziosa collaborazione.

Con grande affetto voglio ringraziare tutta la mia famiglia.

In particolare Gabriele, che ha condiviso con me questa grande avventura, standomi sempre accanto e dandomi sempre ottimi consigli. Voglio inoltre ringraziarlo perché ha spinto affinché dessi sempre il meglio di me e riuscissi a raggiungere traguardi importanti. Veramente poche persone al mondo hanno la sua forza e la sua lungimiranza.

Ringrazio i miei genitori per la grande comprensione e la costante presenza anche nei momenti difficili.

Grazie a Lina ed Antonio che con grande simpatia ed affetto mi hanno sempre sostenuta.

Grazie ai miei grandi compagni di vita Kimi e Molly che hanno rallegrato e riempito in maniera buffa ed affettuosa le mie dure giornate, soprattutto durante la scrittura della tesi.

TABLE OF CONTENTS

1	INTRODUCTION	1
1.1	Organic Electronics	1
1.2	Historical Background of Organic Electronics	4
1.3	Electrical Conductivity	6
1.4	Conduction in Organic Semiconductor Materials	8
1.4.1	Band Theory of Solids	9
1.4.2	Mechanism of Polymer Conductivity	13
1.4.3	Molecular Electron-Transfer Theory	17
1.4.4	Organic Charge-Transporting Materials: Hole- and Electron-Transport Classification.....	20
1.4.5	Determination of Frontier Orbital Levels.....	22
1.4.6	Organic polymer film-forming processes	24
1.4.7	Organic Electronics: Commercial Applications	28
1.5	ORGANIC FIELD-EFFECT TRANSISTORS (OFETs).....	31
1.5.1	Introduction	31
1.5.2	Working Principle of FETs	31
1.5.3	Current-Voltage Characteristics	35
1.5.4	Device Structure	38
1.5.5	Organic Functional Materials for OFET Devices.....	39
1.6	ORGANIC SENSORS.....	46
1.6.1	Introduction	46
1.6.2	Volatile Organic Compounds (VOCs) Detection: Transduction Mechanism.....	47
1.6.3	Conducting Polymers for Volatile Organic Compounds (VOCs) Detection	50
1.7	ORGANIC SOLAR CELLS	53
1.7.1	Introduction	53
1.7.2	Principle of Operation.....	54

1.7.3	Electronic Donor-Acceptor Interactions	56
1.7.4	Determination of Photovoltaic Performance	58
1.7.5	Organic Functional Materials for Photovoltaic Cells	62
2	EXPERIMENTAL.....	65
2.1	Materials and Methods	65
2.1.1	Proton Resonance Magnetic Nuclear (¹ H NMR).....	65
2.1.2	Optical Microscopy.....	65
2.1.3	Differential Scanning Calorimetry.....	65
2.1.4	UV-Vis Spectroscopy	66
2.1.5	Photoluminescence Spectroscopy (PL).....	66
2.1.6	Thermogravimetric Analysis (TGA).....	66
2.1.7	Spin Coating	66
2.1.8	Mass Spectrometry.....	66
2.1.9	Single Crystal X-Ray Crystallography	67
2.2	Monomers Synthesis.....	67
2.2.1	Synthesis Monomer I	68
2.2.2	Synthesis Monomer IV	69
2.3	Synthesis Cu(II) Complexes	71
2.3.1	Synthesis Cu(Ald1).....	72
2.3.2	Synthesis Cu(Im)	72
2.4	Synthesis Polythiophenes	73
2.4.1	Synthesis PT8-VO(acac) ₂	74
2.4.2	Synthesis PT8-Cu(Ald1)	74
2.4.3	PT8-Cu(Im)	75
2.5	Perylene-3,4,9,10-tetracarboxylic acid diimide (PDI) derivatives synthesis.....	76
2.5.1	Synthesis TDZ-C7	76
2.5.2	Syntesis TR-C7.....	78

3	POLYTHIOPHENES 3-SUBSTITUTED FOR APPLICATIONS IN ELECTRONICS.....	80
3.1	Introduction	80
3.2	Polythiophenes 3-Substituted for Applications in Organic Sensors	82
3.2.1	Synthesis Methods	85
3.2.2	Characterization Methods	89
3.2.3	Detection of VOCs Compounds Using Polythiophenes 3-Substituted.....	95
3.3	Synthesis of Highly Regioregular Poly[3-(4-alkoxyphenyl)-thiophene]s by Oxidative Catalysis Using Copper Complexes for Application in Photovoltaics.....	105
3.4	Measurement of FET Mobility of PT8-Cu(Ald1)	125
4	SYNTHESIS OF ALKYLTHIADIAZOLE AND ALKYLTRIAZOLE-SUBSTITUTED PERYLENEBIS (DICARBOXIMIDES) FOR APPLICATION IN FET DEVICES	127
4.1	Introduction	127
4.2	Alkylthiadiazole and alkyltriazole-substituted perylenebis(dicarboximides).....	129
4.3	Measurement of FET Mobility of PDI Derivatives.....	138
5	OPTOELECTRONIC AND ELECTRICAL PROPERTIES INVESTIGATION OF PT8- Cu(Ald1) AND TDZ-C7 AS DONOR AND ACCEPTOR MATERIALS IN SOLAR ORGANIC CELLS	147
5.1	Introduction	147
5.2	Chemical-Physically Characterizations	147
6	CONCLUSIONS	155
7	REFERENCES	161

LIST OF FIGURES

Figure 1: Conductivity of conductive polymers compared to those of other materials, from quartz (insulator) to copper (conductor). Polymers may also have conductivities corresponding to those of semiconductors “Ad. from [16]”.....	7
Figure 2: The conductivity of conductive polymers decreases with falling temperature in contrast to the conductivities of typical metals, e.g. silver, which increase with falling temperature “Ad. from [16]”... 8	8
Figure 3: Band formation obtained by mixing of electronic states.	10
Figure 4: The allowed energy states for an metal, semiconductor, and insulator.	11
Figure 5: Molecular orbitals in polyacetylene. Each carbon atom is in hybridized sp^2p_z double-bond configuration. Depending on the mathematical sign (illustrated in blue or red color), the p_z -orbital is either bonding or anti-bonding, and forms a π - or π^* -bond, respectively. Optical or thermal excitation can promote electrons from π - into π^* -orbitals that exhibit lower binding energies “Ad. from ”.....	12
Figure 6: Radical cation (“polaron”) formed by removal of one electron on the 5 th carbon atom of a undecaheptaene chain (a \rightarrow b). The polaron migration shown in c \rightarrow e “Ad. from [16]”.....	14
Figure 7: A soliton is created by isomerisation of cis polyacetylene (a \rightarrow b) and moves by pairing to an adjacent electron (b \rightarrow e). However, generally solitons made by doping are more important than “bond alternation defects” like the one illustrated in the figure “Ad. from [16]”.....	16
Figure 8: Intersoliton hopping: charged solitons (bottom) are trapped by dopant counterions, while neutral solitons (top) are free to move. A neutral soliton on a chain close to one with a charged soliton can interact: the electron hops from one defect to the other “Ad. from [16]”.....	17
Figure 9: electron transfer reaction between a naphthalene cation with an anthracene molecule “Ad. from [16]”.....	18
Figure 10: representation of energy surface of reactant state and product state for electron transfer reaction between a naphthalene cation with an anthracene molecule “Ad. from [16]”.....	18

Figure 11: Two parabolic potential energy graphs corresponding to the energy for reactant and product states in an electron transfer reaction. ΔG^* is the activation barrier that has to be overcome and λ is the “reorganization energy” “Ad. from [16]”	19
Figure 12: Spin-coating process.	25
Figure 13: The LB sequence: spreading, compression, and deposition.....	26
Figure 14: (a) Schematic structure of a field-effect transistor and applied voltages: L = channel length; W = channel width; V_d = drain voltage; V_g = gate voltage; V_{Th}) threshold voltage; I_d) drain current. (b-d) Illustrations of operating regimes of field-effect transistors: (b) linear regime; (c) start of saturation regime at pinchoff; (d) saturation regime and corresponding current-voltage characteristics “Ad. from [25]”.....	32
Figure 15: Representative current-voltage characteristics of an n-channel organic field-effect transistor. (a) output characteristics indicating the linear and saturation regimes; (b) transfer characteristics in the linear regime ($V_d \ll V_g$), indicating the onset voltage (V_{on}) when the drain current increases abruptly; (c) transfer characteristics in the saturation regime ($V_{ds} > V_g - V_{Th}$), indicating the threshold voltage V_{Th} , where the linear fit to the square root of the drain current intersects with the x -axis “Ad. from [25]”...	37
Figure 16: Common field-effect transistor configurations. (a) bottom contact, top gate (BC/TG); (b) bottom contact, bottom gate (BC/BG); (c) top contact, bottom gate (TC/BG). “Ad. from [25]”.....	38
Figure 17: Small molecule semiconductors, which are commonly known for their hole channel characteristics in field-effect transistors “Ad. from [25]”.....	40
Figure 18: Conjugated semiconducting polymers that have shown hole and, in some cases, electron field-effect transport “Ad. from [25]”.....	42
Figure 19: Organic semiconductors that show predominantly n-channel behavior in transistors with SiO_2 as a gate dielectric and gold source-drain electrodes “Ad. from [25]”.....	44
Figure 20: Comparison between the work-function responses of conducting polymer layers to different vapors. Initial work function (versus Au reference) was adjusted electrochemically to different initial values “Ad. from [28]”.....	49

Figure 21: Chemiresistor. B:bulk of the conducting polymer. S:surface. I:interface with the insulating substrate. C:interface with the contacts “Ad. from [28]”.....	49
Figure 22: A PV device (right) is the reverse of a LED (left). In both cases an organic material is sandwiched between two electrodes. In PVs electrons are collected at the metal electrode and holes are collected at the ITO electrode. The reverse happens in a LED: electrons are introduced at the metal electrode (cathode), which recombine with holes introduced at the ITO electrode (anode) “Ad. from [33]”.	54
Figure 23: Energy levels and light harvesting. Upon irradiation an electron is promoted to the LUMO leaving a hole behind in the HOMO. Electrons are collected at the Al electrode and holes at the ITO electrode. Φ : workfunction, χ : electron affinity, IP: ionization potential, E_g : optical bandgap “Ad. from [33]”....	55
Figure 24: Band structure diagram illustrating the HOMO and LUMO energies of MDMO-PPV, P3HT, and an “ideal” donor relative to the band structure of PCBM. Energy values are reported as absolute values relative to a vacuum “Ad. from [34]”.....	58
Figure 25: The quantum efficiency of a silicon solar cell “Ad. from [36]”.....	60
Figure 26: I-V curves of an organic PV cell under dark (left) and illuminated (right) conditions. The opencircuit voltage (V_{oc}) and the short-circuit current (ISC) are shown “Ad. from [33]”.....	62
Figure 27: Several polymers employed in prototypical solar cells “Ad. from [34]”.....	64
Figure 28: Molecular structure of the monomers.	67
Figure 29: Molecular structure Cu(II) complexes.	71
Figure 30: Molecular structures of polythiophenes.	73
Figure 31: Molecular structures of PDI derivatives.....	76
Figure 32: Different configurational triads in polythiophenes 3-substituted.	81
Figure 33: Synthesis scheme of polythiophenes.....	83
Figure 34: Mechanism of polymerization of thiophenes.	84
Figure 35: A catalytic cycle of the oxivanadium catalytic system.	84
Figure 36: Synthesis of 1-bromo-(4-esiloxy)benzene by Williamson etherification.	86
Figure 37: Synthesis of monomer (I) by Grignard reaction.	86
Figure 38: Scheme of synthesis of monomer (IV).....	87

Figure 39: Scheme of synthesis of the polythiophenes.....	88
Figure 40: ¹ H-NMR spectrum of PT5-6(II)	90
Figure 41: UV-Vis spectra by polymer films before and after annealing.....	92
Figure 42: Supposed chemical structure consequent to crosslinking reaction.....	94
Figure 43: Structure of a chemiresistor device.....	95
Figure 44: Cycle sensor device is subdivided in three faces: baseline, step and recovery.	96
Figure 45: Sensor responses of PT8 to various VOC vapors.....	98
Figure 46: Concentration analytes versus variation of the current.....	100
Figure 47: Sensor responses of P5-6(I) to various VOC vapors.....	101
Figure 48: Concentration analytes versus variation of the current.....	103
Figure 49: Vanadyl complex experimented.....	106
Figure 50: Molecular structure of Cu(II) catalyst.....	107
Figure 51: Synthesis Scheme of Cu(II) complexes.....	107
Figure 52: Thermogravimetric analysis of Cu(Ald2) complex.....	108
Figure 53: Ortep-3 view of Cu(Im) with ellipsoids drawn at 30% probability level. Hydrogen atoms are omitted for clarity. Symmetry transformation used to generate equivalent atoms: _i -x, -y, -z (the molecule lies on a crystallographic inversion centre). Selected bond distances and angles (Å, °): Cu1-O1 = 1.887(3), Cu1-N1 = 1.983(3), O1-Cu1-N1 = 91.5(1), O1-Cu1-N1 _i = 88.5(1), N1-Cu1-N1 _i = 180.0, O1-Cu1-O1 _i = 180.0, N1-C1-C2-C3 = -8.2(6), N1-C1-C2-C7 = 174.8(3), O3-C8-C9-C10 = 0.1(7).....	111
Figure 54: Synthesis scheme of polythiophenes using Cu(II) complexes.....	112
Figure 55: UV-Vis spectra of polymer films.....	114
Figure 56: ¹ H-NMR spectrum of PT8 prepared by Cu(Ald1) complex.....	115
Figure 57: Deconvolution process applied to thiophenic singlets.....	117
Figure 58: Diads that can be formed in polymerization process. F and B denote the forward and the opposite orientations of monomer units defined for propagating terminal radicals, respectively.	118
Figure 59: Deconvolution process applied to thiophenic singlets of PT8 prepared using VO(acac) ₂	120

Figure 60: Synthesis scheme of PT6-8 and PT8Iso.....	122
Figure 61: UV-Vis spectra of PT6-8 and PT8Iso.....	123
Figure 62: Deconvolution process applied to thiophenic singlets.....	124
Figure 63: Film of PT8-Cu(Ald1) deposited via spin-coating onto FET device.....	125
Figure 64: Current-voltage characteristics of PT8-Cu(Ald1) based device.....	126
Figure 65: Synthesis scheme of PDI functionalized with thiadiazole group.....	130
Figure 66: Synthesis scheme of TR-C7.....	131
Figure 67: Thermogravimetric analysis of TDZ-C13.....	132
Figure 68: Absorbance and emission spectra of the PDI derivatives functionalized with thiadiazole group.....	134
Figure 69: Absorbance and emission spectra of TR-C7.....	135
Figure 70: Substrate functionalization with HMDS.....	139
Figure 71: Current-voltage characteristics and mobility trends of OTFT devices.....	142
Figure 72: AFM images of TDZ-C13 films obtained by thermic evaporation.....	144
Figure 73: AFM images of TDZ-ST film obtained by thermic evaporation on functionalized substrate.....	145
Figure 74: AFM images of TDZ-ST film obtained by spin-coating on functionalized substrate.....	146
Figure 75: Cyclic voltammograms of PT8-CuAld1 and TDZ-C7.....	148
Figure 76: Energy diagram of the orbital frontiers belong to PT8-CuAld1 and TDZ-C7.....	149
Figure 77: Absorbance and emission spectra of PT8(CuAld1) and TDZ-C7 film obtained by Langmuir-Blodgett method.....	152

LIST OF TABLES

Table 1: Quantitative evaluation of monomer I and IV contained in the copolymers compared to stoichiometric amounts of monomers are allowed to react: ^a experimental values found; ^b theoretical values.	91
Table 2: Data related to redshift of λ_{\max} for polymer films before and after annealing.	93
Table 3: Characteristics of the PT8 based devices.	99
Table 4: Characteristics of the PT5-6(I) based devices.	104
Table 5: Thermogravimetric analysis of Cu(II) complexes.	109
Table 6: Crystal data and structure refinement details for Cu(Im).	110
Table 7: Dates related to λ_{\max} values and vibronic structure of polymer films.	114
Table 8: The HT values of PT8 synthesized through Cu(II) complexes.	120
Table 9: The HT values of PT6-8 and PT8Iso.	123
Table 10: Temperatures of decomposition of PDI derivatives.	133
Table 11: Values of the fluorescence quantum yields of the PDI derivatives.	136
Table 12: Contact angle values of some substrates functionalized with HMDS.	140
Table 13: Comparison of the mobility values of TDZ-ST and TDZ-C13.	141

1 INTRODUCTION

1.1 Organic Electronics

Organic electronics has been the focus of a growing body of investigation in the fields of physics and chemistry for more than 20 years. The enormous technological interest of organic electronics originates from the special features of polymeric and molecular π -conjugated compounds which combine optical and electrical properties of inorganic semiconductors with chemical-physical characteristics and easy processability of organic polymeric and molecular materials [1]. Furthermore, The attraction of this field has been the ability to modify chemical structure in a ways that could directly impact properties of the materials when deposited in thin film form [2]. In fact, organic thin films have proven useful in a number of applications, some of them now are reaching the consumer market. Organic materials used in electronic and optoelectronic devices are generally split into two groups: i.e., small molecules and polymers. The former are typically deposited by vapor methods in low or high vacuum environments and have a well-defined molecular weight. Polymers, on the other hand, must be processed from solution and have a molecular weight distribution that is described by the polydispersity of materials, giving polymers good glass-forming and mechanical properties. Dendrimers are a class of materials that in some ways fall between molecular and polymeric materials. Dendrimers are highly branched molecules, whose branches originating from the molecular core They typically have very high but at the same time well-defined molecular weights. Thus, while dendrimers are molecular in nature, their high molecular weight and irregular shape give them bulk properties resembling those of a polymer. While many of the electronic

properties of organic materials and their associated devices are similar, the methods used for fabricating organic and inorganic based devices are considerably different. The use of organic compounds as active materials in electronic and optoelectronic devices opens the door to a large number of efficient and potentially low-cost methods for fabricating useful, and, in some cases, complicated structures that are inaccessible by conventional methods using conventional semiconductors. For example, the techniques available for processing and patterning organic materials move far beyond the lithographic methods that govern inorganic devices. In fact there are a range of low-cost processes that are unique to organic materials, including embossing, imprint lithography, capillary molding and printing, roll-to-roll and spin-coating. A main challenge is to develop efficient opto-electronic devices, such as light-emitting diodes (LEDs), field-effect transistors (FETs), or solar cells, in which the inorganic materials traditionally used as active elements are replaced with organic materials. Such devices can benefit from the many attractive features of organic materials, in particular the possibility to tailor their synthesis to match specific needs and the ease of processing thin films over large surfaces at low cost. The transport of charges in the organic layers plays a key role in defining the overall performance of these devices. The most highly advanced organic devices are organic light emitting diodes (OLEDs). In fact, it has been demonstrated that these devices have internal quantum efficiencies near unity, and they have been developed so much that they are commercially available in small, hand-held, full color displays. While the demonstrated efficiencies for OLEDs are very high, their operating voltages can be high, limiting their power efficiencies (optical power/electrical power). Incorporating p- and n-type dopants in the transporting layers of the devices lowers their operating voltages to levels close to the theoretical limits, i.e.,

where the operating voltage approaches that of the emitted photon energy. Organic materials for use in laser emission have been a subject of investigation since the first report of a dye laser. However, the lasers that have become ubiquitous in society for use in applications ranging from optical communications, to optical memories, and to biomedical testing are entirely based on inorganic semiconductor materials. Nevertheless, organic semiconductors combine novel optoelectronic properties with simple fabrication techniques and offer the scope for tuning the chemical structure to give desired features (such as emission wavelength), making them attractive for using in many laser applications. Transistors based on inorganic semiconductors form the basis for a wide range of electronic devices that utilize their high speed and small size for integration on a massive scale. Organic transistors (OFETs) have the potential to have a great impact. However, they will not compete directly with silicon or gallium arsenide due to the lower charge mobilities and device lifetimes of organic based systems. Nevertheless, organic transistors and circuits are technologically interesting because they have potential to serve in inexpensive (perhaps disposable) and flexible electronic circuits. Major applications include radio frequency identification tags and flexible display backplanes. These circuits can be potentially fabricated by simple printing methods, not requiring the demanding environment needed for silicon based circuitry. One of the earliest applications of organic optoelectronic devices is in solar cells. Inorganic semiconductor solar cells are well developed and are being deployed worldwide; however, the high cost of their manufacture ultimately limits their widespread acceptance as a source of renewable energy. The potential for low-cost manufacturing afforded by organic devices gives organic solar cells the potential to significantly impact the energy landscape, making them useful in a wide

range of environments. Chemical sensing is also emerging as an important application for organic materials. Uses in military, biomedical, and industrial environments are ubiquitous, and having the ability to sensitively detect specific chemicals, both accurately and inexpensively, could vastly expand their applications. Research on advanced organic materials has led to marked improvements in the sensitivity and versatility of chemical sensors.

1.2 Historical Background of Organic Electronics

The first studies of the dark and photo-conductivity of anthracene crystals dates back to the early 20th century by an Italian scientist named Pochettino [3]. The study of the dark conductivity in anthracene was dealt simultaneously with the silicon's one in 1910 by Konigsberger and Schilling in Germany. A prototype of an organic photovoltaic cell was presented in 1913 by Volmer [4]. Anthracene has been used as a model organic photoconductor for quite a while. Soon after the invention of the very efficient purification method called zone refinement [5],[6], the experimental determination of intrinsic energy levels [7], charge-transport properties, effects of impurities, charge generation mechanisms [8], recombination, space-charge-limited conduction, electroluminescence [9], and trapping effects have been studied in detail, also for other materials. The physical fundamentals can be found about studies of Pope and Swenberg [10]. Since the 1970s, the successful synthesis and controlled doping of conjugated polymers established the second important class of organic semiconductors. In fact The Royal Swedish Academy of Sciences decided to award the Nobel Prize in Chemistry for 2000 to Alan J. Heeger, Alan G. MacDiarmid and Hideki Shirakawa for the discovery and development of electrically conductive

polymers [11]. Conducting polymers have afforded the first applications of organic materials as conductive coatings or photoreceptors in electrophotography. Two major breakthroughs followed in the 1980s. An efficient photovoltaic cell incorporating an organic hetero-junction of p- and n-conducting materials [12] as well as the first thin film transistor were successfully demonstrated on the basis of undoped organic semiconductors [13]. The main impetus, however, came from the demonstration of high-performance electroluminescent diodes from vacuum-evaporated molecular films by Tang and Van Slyke in 1987 [14] as well as from conjugated polymers in 1990 [15]. During the last twenty years, organic light-emitting devices have progressed and rapidly lead to various commercial products.

1.3 Electrical Conductivity

Conductivity is defined by Ohm's law:

$$U = R I \quad (1)$$

where I is the current (in Amperes) through a resistor and U is the drop in potential (in Volts) across it. The proportionality constant R is called the “resistance”, measured in Ohms (Ω). R is measured by applying a known voltage across the resistor and measuring the current through it. The reciprocal of resistance (R^{-1}) is called *conductance*. Ohm's law is an empirical law, related to irreversible thermodynamics (Ilya Prigogine, Nobel Prize in Chemistry 1977), the flow I as a result of a gradient in potential leads to energy being dissipated ($RI^2 \text{ J s}^{-1}$). Not all materials obey Ohm's law. Gas discharges, vacuum tubes, semiconductors and what are termed onedimensional conductors (*e.g.* a linear polyene chain) generally all deviate from Ohm's law. In Ohmic material the resistance is proportional to the length l of the sample and inversely proportional to the sample cross-section A :

$$R = \rho l / A \quad (2)$$

where ρ is the resistivity measured in $\Omega \text{ cm}$ (in SI units $\Omega \text{ m}$). Its inverse $\sigma = \rho^{-1}$ is the *conductivity* (Figure 1). The unit of conductance is the Siemens ($\text{S} = \Omega^{-1}$). The unit of conductivity is S m^{-1} .

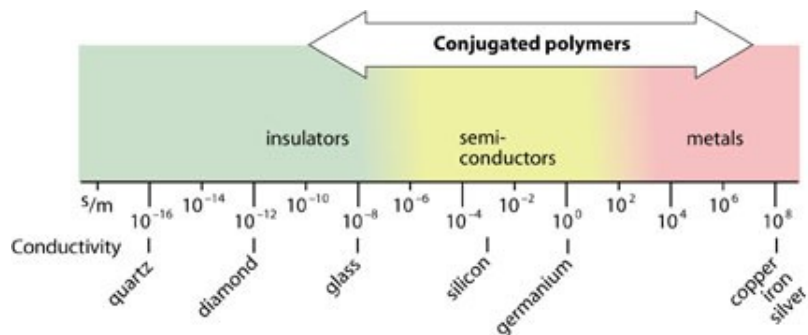


Figure 1: Conductivity of conductive polymers compared to those of other materials, from quartz (insulator) to copper (conductor). Polymers may also have conductivities corresponding to those of semiconductors “Ad. from [16]”.

Conductivity depends on the number density of charge carriers (number of electrons n) and how fast they can move in the material (mobility μ):

$$\sigma = n \mu e \quad (3)$$

where e is the electron charge. In semiconductors and electrolyte solutions, one must also add in Equation (3) an extra term due to positive charge carriers (holes or cations). Conductivity depends on temperature: it generally increases with decreasing temperature for “metallic” materials (some of which become superconductive below a certain critical temperature T_c), while it generally decreases with lowered temperature for semiconductors and insulators (Figure 2) [16].

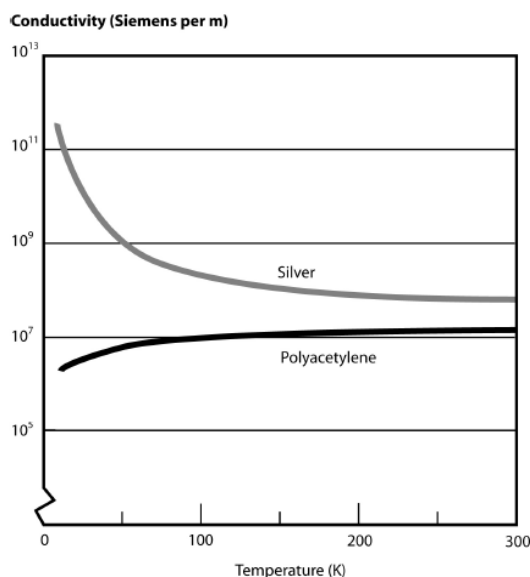


Figure 2: The conductivity of conductive polymers decreases with falling temperature in contrast to the conductivities of typical metals, e.g. silver, which increase with falling temperature “Ad. from [16]”.

1.4 Conduction in Organic Semiconductor Materials

Electrical conductivity refers to the transport of charge carriers through a medium under the influence of an electric field or temperature gradient and is so dependent on the number of charge carriers and their mobility. The charge carriers may be generated intrinsically or from impurities, in which case they may be electrons, holes, or ions. Alternatively, electrons or holes may be injected from electrodes. Therefore conduction may be of two types ionic and electronic both and for them there have been a focus of intense research, particularly ionic conduction, which has been studied for many years and has been the subject of several books. In general, organic systems are insulating materials having conductivities ranging from $10^{-10} (\Omega \text{ cm})^{-1}$ to $10^{-18} (\Omega \text{ cm})^{-1}$, which are many orders

of magnitude below the conductivities associated with metals. Indeed, low conductivity (and consequent low dielectric constant) is one of the major reasons polymers have found widespread acceptance in a myriad of insulating and structural applications throughout the electronics industry. Nevertheless, the discovery in 1973 that poly(sulfur nitride) was intrinsically conducting provided proof that polymers could be conducting and greatly stimulated the search for other conducting organic materials [17].

1.4.1 Band Theory of Solids

When a large number of atoms (e.g., as in metals or semiconductors) or molecules (e.g., organic metals) are brought together in the crystalline state, the electronic states mix so as to form bands, each band consisting of electronic states whose energies form a continuous range. This situation is analogous to the splitting of atomic energy levels as two atoms are brought together to form a molecule. For example, the ethylene molecule consists of two sp^2 -hybridized carbon atoms, each containing an unpaired electron in a p orbital; the two orbitals overlap to form a π bond. According to Hückel theory, the interaction of these two p orbitals forms two molecular orbitals corresponding to the π bonding and π antibonding (π^*) orbitals (Figure 3), separated by an energy Δ . If these orbitals are allowed to interact with the π and π^* orbitals of a second ethylene molecule stacked directly above the first, two sets of two molecular orbitals are formed that are separated by energy 2δ , where δ is the resonance or transfer integral. Likewise, if n ethylene molecules are allowed to interact, n states from each of the π and π^* orbitals are formed. For large values of n , the energy states are close enough together to correspond to

a continuous band. The $2n$ electrons are then allowed to fill the bands in a manner analogous to the Aufbau principle for atoms (i.e., electrons are placed in these states in pairs starting with the lowest energy state and filling the higher energy states successively). The highest occupied state is called the Fermi level.

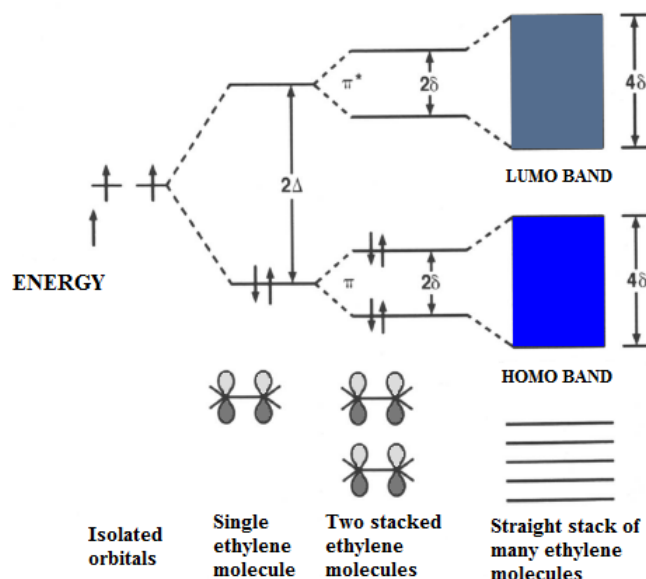


Figure 3: Band formation obtained by mixing of electronic states.

As seen in Figure 3, the band formed from the highest occupied molecular orbital (HOMO) in the stack of ethylene molecules is entirely full, but the band formed from the lowest unoccupied molecular orbital (LUMO) is entirely empty. According to band theory, if the highest filled band (referred to as the valence band) is only partially full, the empty states which exist close to the Fermi level will facilitate conduction. In the case of the hypothetical stack of ethylene molecules, the HOMO band is completely full. For the stack

to be conductive, energy must be supplied to move an electron into the next lowest state, which in this case happens to be the lowest energy level in the LUMO band (also called the conduction band). This energy gap separating the two bands is called the band-gap energy (E_g in eV), and its magnitude determines whether such a material is a semiconductor or an insulator (Figure 4).

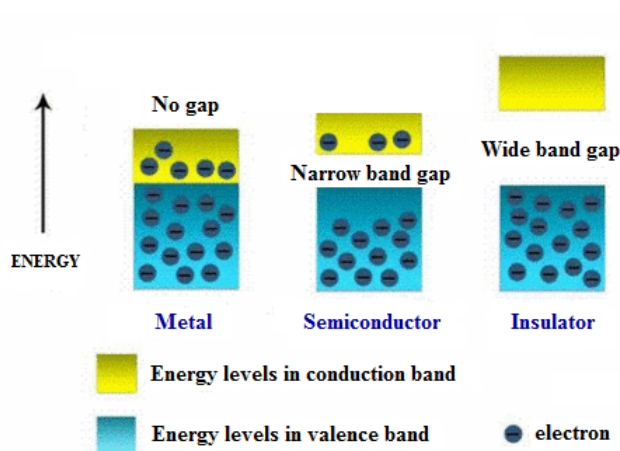


Figure 4: The allowed energy states for an metal, semiconductor, and insulator.

Polyacetylenes and related π -conjugated systems, for example, have conductivities that classify them as semiconductors. The carbon atom in polyacetylene is sp^2 hybridized, which leaves one p electron out of the bond-forming hybrid orbitals. In principle, such a structure might be expected to give rise to extended electronic states formed by overlap of the p (π) electrons and thus provide a basis for metallic behavior in polymers. In practice, the quasi-one-dimensional structure just described is not stable. Instead, the π electrons overlap in an alternating fashion, resulting in the familiar conjugated π -bond structure of

polyacetylene. In energetic terms, bond alternation causes a gap energy (E_g) to be opened at the Fermi level that converts the system from a conductor to a semiconductor (Figure 5).

Physicists refer to this as a *Pierls transition*.

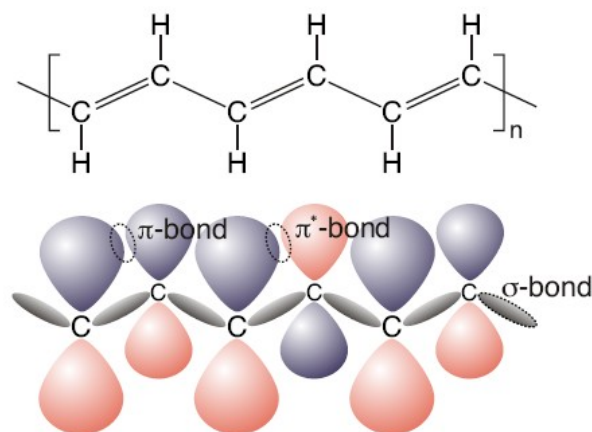


Figure 5: Molecular orbitals in polyacetylene. Each carbon atom is in hybridized sp^2p_z double-bond configuration. Depending on the mathematical sign (illustrated in blue or red color), the p_z -orbital is either bonding or anti-bonding, and forms a π - or π^* -bond, respectively. Optical or thermal excitation can promote electrons from π - into π^* -orbitals that exhibit lower binding energies “Ad. from”.

A major breakthrough in the search for conducting polymers occurred in 1977 [11] with the discovery that polyacetylene could be readily oxidized (by electron acceptors such as iodine or arsenic pentafluoride) or reduced (by donors such as lithium). The resulting material had a conductivity that was orders of magnitude greater than the original, untreated sample. This process is often referred to as *doping* by analogy with the doping of inorganic semiconductors, but it contrasts with the inorganic semiconductor doping in that doping in polymers is a redox process involving charge transfer with subsequent creation

of charged species. The redox reaction may be carried out in the vapor phase, in solution, or electrochemically.

1.4.2 Mechanism of Polymer Conductivity

The origin of the conduction mechanism has been a source of controversy ever since conducting polymers were first discovered. At first, doping was assumed to simply remove electrons from the top of the valence band (oxidation) or add electrons to the bottom of the conduction band (reduction). This model associates charge carriers with free spins (unpaired electrons). However, the measured conductivity in doped polyacetylene (and other conducting polymers such as polyphenylene and polypyrrole) is far greater than what can be accounted for on the basis of free spin alone. To account for this phenomenon of spinless conductivity, physicists have introduced the concept of transport via structural defects in the polymer chain. In a conventional semiconductor, an electron can be removed from the valence band and placed in the conduction band, and the structure can be assumed to remain rigid. In contrast, an electronic excitation in polymeric materials is accompanied by a distortion or relaxation of the lattice around the excitation, which minimizes the local lattice strain energy. The combined structural and electronic excitation will now look like a defect on the chain. From a chemical viewpoint, this defect is interpreted as a radical cation (or radical anion in the case of reduction). Physicists refer to it as a *polaron* (Figure 6). Because these defects represent localized distortions of the lattice, the associated energy level must be split off from the continuum of band states.

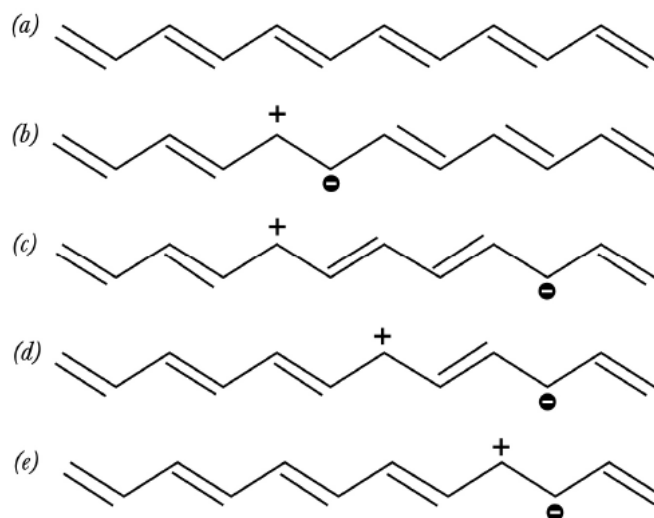


Figure 6: Radical cation (“polaron”) formed by removal of one electron on the 5th carbon atom of a undecaheptaene chain (a → b). The polaron migration shown in c → e “Ad. from [16]”.

The two polaron states corresponding to a radical cation and radical anion are symmetrically disposed around the Fermi level (i.e., the midpoint of the gap). Removal of an electron leaves an unpaired spin near the valence band edge (*p* doping), and addition of an electron fills the corresponding state near the conduction band edge (*n* doping). Further oxidation (or reduction) results in the formation of what physicists call a *bipolaron*. In the oxidation case, it is energetically much more favorable to take the second electron from the polaron than to form a second polaron [18]; thus, the oxidation process may be viewed as leading to the formation of a localized doubly charged species (i.e., a dication, or dianion in the case of reduction). The bipolaron is thus identified as a dication or dianion associated with a strong local lattice distortion. Because the lattice relaxation around the charges is stronger than in the case of a single charge, the electronic states appearing in the band edge are further away from the band edges (closer to the Fermi level) than they are for polarons.

Coulombic repulsion might be expected to result in charge separation, but separation is only feasible if the polymer possesses a degenerate ground state. As discussed earlier, bipolarons contain no free spins. All energy levels in the gap are either empty or full. These species are believed to be involved in the conduction process. Evidence for their existence comes from spectroscopic studies, although the precise mechanism of charge conduction is not really known. For one thing, the charges should be fixed in position along the chain by the counterion derived from the dopant species. Furthermore, polymers themselves contain many defects such as cross-links, chain ends, and bends, and it is difficult to see how even a mobile bipolaron or polaron could move past such obstacles. Conduction mechanisms have been proposed, at least in the case of polyacetylene itself, that involve a different type of defect structure called a *soliton*. (Figure 7). In fact *cis*-polyacetylene chain by undergoing “thermal” isomerisation to *trans* structure may create a defect, a stable free radical: this is a *neutral* soliton which although it can propagate along the chain may not itself carry any charge. On the other hand, it may contribute to charge transfer between different chains. Bulk conductivity in the polymer material is limited by the need for the electrons to jump from one chain to the next, i.e., in molecular terms an intermolecular charge transfer reaction. It is also limited by macroscopic factors such as bad contacts between different crystalline domains in the material.

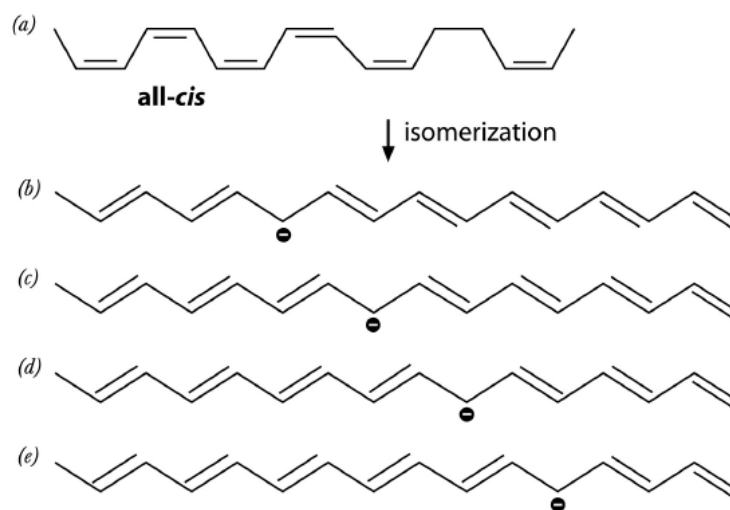


Figure 7: A soliton is created by isomerisation of cis polyacetylene ($a \rightarrow b$) and moves by pairing to an adjacent electron ($b \rightarrow e$). However, generally solitons made by doping are more important than “bond alternation defects” like the one illustrated in the figure “Ad. from [16]”.

One mechanism proposed to account for conductivity by charge-hopping between different polymer chains is “intersoliton hopping” (Figure 8). Here an electron is jumping between localized states on adjacent polymer chains; the role of the soliton is to move around and to exchange an electron with a closely located charged soliton, which is localized. The mechanism at work in intersoliton hopping is very similar to that operating in most conducting polymers somewhere in between the metallic state at high doping and the semiconducting state at very low doping. All conjugated polymers do not carry solitons, but polarons can be found in most of them. Charge transport in polaron-doped polymers occurs via electron transfer between localized states being formed by charge injection on the chain.

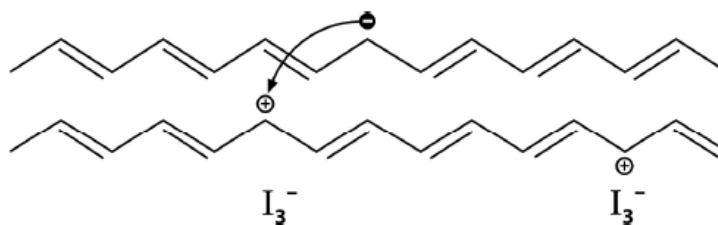


Figure 8: Intersoliton hopping: charged solitons (bottom) are trapped by dopant counterions, while neutral solitons (top) are free to move. A neutral soliton on a chain close to one with a charged soliton can interact: the electron hops from one defect to the other “Ad. from [16]”.

1.4.3 Molecular Electron-Transfer Theory

Electron transfer (ET) reactions, which are also redox reactions, are among the most common and simple chemical reactions. The electron donor is oxidised and the acceptor reduced. The free energy that drives the reaction is the difference in reduction potentials between donor and acceptor. One type of ET reaction, charge separation, takes place after photo-excitation to an upper potential energy surface (PES). For example, in photosynthesis a series of ET reactions all start from a photo-induced charge separation. The molecular electron transfer theory based on contributions by Rudolph Marcus (Nobel Prize in Chemistry 1992) [19], so far mainly applied to biopolymers rather than truly conductive polymers. An electron transfer reaction corresponds to motion on a potential energy surface between two minima, corresponding to different stable localizations of an electron. With a naphthalene cation together with an anthracene molecule, the following electron transfer reaction may then take place (Figure 9):

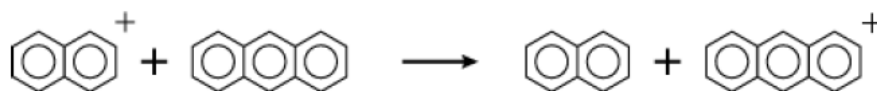


Figure 9: electron transfer reaction between a naphthalene cation with an anthracene molecule “Ad. from [16]”.

Consider the whole system $[(C_{10}H_8)(C_{14}H_{10})]^+$. There are two local minima on its energy surface: one for $[(C_{10}H_8)^+(C_{14}H_{10})]$ corresponding to the reactant state and one for $[(C_{10}H_8)(C_{14}H_{10})^+]$ corresponding to the product state. The latter corresponds to the lowest minimum (Figure 10):

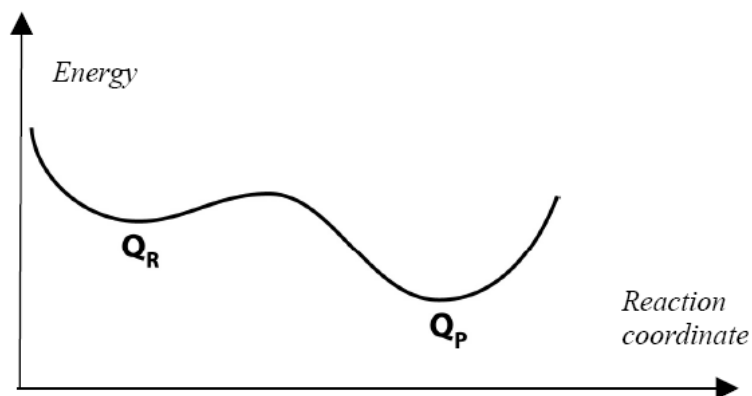


Figure 10: representation of energy surface of reactant state and product state for electron transfer reaction between a naphthalene cation with an anthracene molecule “Ad. from [16]”.

In this system there is a barrier between the two minima. At the left (reactant) minimum the bond lengths are those for the naphthalene cation-neutral anthracene combination. At the right (product) minimum the bond lengths refer to neutral naphthalene and anthracene

cation. The local minima, Q_R for the reactant state and Q_P for the product state, are each approximately parabolic: if we move any of the atoms away from its equilibrium position by change dQ in bond length or bond angle, the energy would increase by $(k/2)dQ^2$, where k is a force constant corresponding to this deformation. Another contribution to the barrier comes from the solvent. If a dissolved charged molecule changes its charge distribution, the solvent molecules reorient themselves to minimize the total energy. In the *Marcus model* the PESs are approximated by interacting parabolas. This model uses the important fact that the structure undergoes only a rather small change, compared to other chemical reactions, in the ET reaction. Figure 11 assumes that $\Delta G^\circ = 0$ (parabolas of equal height).

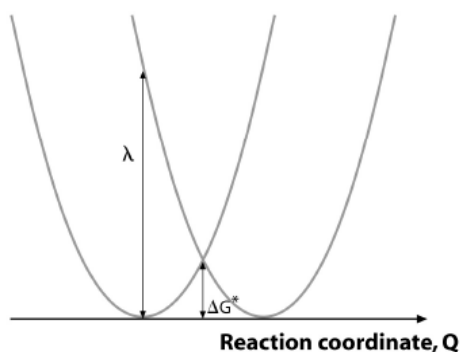


Figure 11: Two parabolic potential energy graphs corresponding to the energy for reactant and product states in an electron transfer reaction. ΔG^* is the activation barrier that has to be overcome and λ is the “reorganization energy” “Ad. from [16]”.

The fundamental equation for the rate in the Marcus model derives from the Arrhenius and Eyring rate equation:

$$k = \nu \kappa e^{(-\Delta G^*/kT)} \quad (4)$$

where ν is the frequency of a vibration corresponding to the number of attempts per unit time to ascend the barrier. κ is a transmission coefficient. ΔG^* is the height of the barrier. In the Marcus model another quantity is needed: reorganization energy (λ). If the free energy change ΔG^0 for the reaction is zero, λ is in the simplest case the vertical energy difference from the minimum of one parabola up to the other parabola. If ΔG^0 is negative the ET reaction is spontaneous and will run from left to right. In this case the right parabola is lower than the left by the amount $-\Delta G^0$. We then have the following activation energy:

$$\Delta G^* = (\lambda/4)(1 + \Delta G^0/\lambda)^2 \quad (5)$$

The activation energy obviously disappears if $-\Delta G^0 = \lambda$. If an electrical field is applied so that, *e.g.*, the right (product) parabola is lowered, *i.e.*, ΔG^0 is more negative, this will also lead to a reduction in the activation energy ΔG^* . From this follows that if a field is applied, the electron leaps more easily between donor and acceptor. The Marcus model has been mainly applied to electron transfer reactions in biomolecular contexts and in a few cases also to semiconductive polymers [20].

1.4.4 Organic Charge-Transporting Materials: Hole- and Electron-Transport

Classification

Organic semiconductor materials can be classified as hole- or electron-transport (HT or ET) materials according to whether the majority charge carriers, under a given set

of conditions, arise from removal of electrons from the manifold of filled molecular orbitals or from the addition of electrons to empty orbitals, respectively. Therefore, materials which have low ionization potentials together with low electron affinities usually function as hole-transporting materials, whereas materials which have high electron affinities together with high ionization potentials usually function as electron-transporting materials. Organic HT and ET materials differ from classical inorganic p- and n-type semiconductors in that they are generally undoped, and so that very few charge carriers are typically present except under an applied field, in which case carriers can be injected from electrodes, from other proximate organic materials, or are generated via photoexcitation. Charge transport can be described as a series of successive electron-transfer reactions between neutral and charged molecular or polymeric repeat units. In the hopping transport regime this process involves essentially localized radical cations (HT) or anions (ET) and the corresponding neutral species, while the orbitals of a π -conjugated polymer chain can facilitate intrachain electron transfer in the superexchange or coherent tunneling regime. The tendency of the holes (electrons) to migrate under the influence of a field can be described by the hole (electron) mobility, μ , of the material; this has units of velocity per unit field and is, in general, dependent on both the electric field and temperature. An additional class of materials, ambipolar materials, have similar hole and electron mobilities and can act as either HT or ET materials, depending on the dominant injection processes occurring under the experimental conditions of interest. In general, development of high-performance (environmentally stable, high-mobility) organic ET materials has lagged behind that of HT materials despite their importance for fabricating organic photovoltaic (OPV) cells and n-channel OFETs, which are particularly valuable as components of

organic complementary logic circuits, which require both p- and n-channel transistors. In fact, HT materials usually show high mobility and these materials can be obtained through simple synthesis procedures. Instead, ET materials show low mobilities, environmental instability (radical anions can easily be oxidized by oxygen and water) and difficulties in synthesis. To achieve acceptable performance, ET materials must have high electron affinity (ideally greater than ≈ 3 eV, but not exceeding ≈ 5 eV) to facilitate injection from contacting electrodes in OFETs or to facilitate exciton separation in conjunction with typical HT materials for OPV applications. Moreover, ET materials must have good intermolecular electronic orbital overlap to facilitate high mobility and good air stability, ideally both as neutral and radical anion materials under device operating conditions. [21]

The criteria for useful ET materials described above can often be met by appending strong electron-withdrawing substituents, such as fluoro, cyano, or acyl, to π -conjugated cores such as acenes and oligothiophenes, which, in the absence of these substituents, exhibit HT properties. Other classes of ET materials, such as the fullerenes, which have been widely studied for a variety of applications, have inherently moderate to high electron affinities in the absence of electron-withdrawing substituents.

1.4.5 Determination of Frontier Orbital Levels

The frontier orbital levels can be determined or estimated using a number of spectroscopic techniques, including x-ray photoemission spectroscopy (XPS), ultraviolet photoemission spectroscopy (UPS), and inverse photoemission spectroscopy (IPES). The central microscopic process in all optoelectronic devices is the absorption or the generation of a photon by an electron. The photon generation can happen spontaneously or can be

triggered by another photon. We distinguish the following three key processes and corresponding device types: photon absorption in photodetectors, spontaneous photon emission in light-emitting diodes and stimulated photon emission in laser diodes. Typically, photon absorption and generation involve the generation and recombination of an electron-hole pair, respectively. The photon energy $h\nu$ must be equal or larger than the energy gap E_g between valence and conduction band (h , Planck's constant; and ν , light wave frequency). Correspondingly, the maximum light wavelength $\lambda = c/\nu$ is equal to the so-called gap wavelength

$$\lambda_g \text{ (nm)} = \frac{hc}{E_g} = \frac{1241}{E_g \text{ (eV)}} \quad (6)$$

where c denotes the free-space light velocity.

The spectroscopic techniques above mentioned, probe directly the occupied and unoccupied electronic structure in the molecular interface region. Alternatively, the molecular frontier orbital levels can also be estimated from electrochemical analysis such as cyclic voltammetry (CV) in combination with UV-Vis optical absorption spectra. The Fermi level of a standard or reference electrode (typically silver or platinum) is located between the LUMO and HOMO of organic materials. In order for a working electrode (correlated to the standard electrode) to grab an electron from the HOMO of the molecule, a positive potential (oxidation potential, in reference to the standard electrode) needs to be applied to the working electrode and gradually lower the Fermi level of the working electrode until it reaches the HOMO level of the organic molecule where an electron can

then transfer from the HOMO of the molecule onto the Fermi state of the electrode. This electron transfer would exhibit the first oxidation peak E_{ox} in the CV measurement. When the working electrode is applied a negative potential (reduction potential, in reference to the standard electrode) and gradually increase its Fermi level until it reaches the LUMO level of the molecule, an electron can then transfer from the working electrode onto the LUMO orbital of the molecule. this corresponds to the first reduction potential peak E_{red} . Once the reductive and the oxidative potentials of both the sample and the ferrocene (X) are measured, the sample LUMO and HOMO levels can then be calculated using equation:

$$\text{HOMO/LUMO level} = [-E_{\text{ox/red}} - (4.8 - X)] \text{ eV} \quad (7) [26]$$

where X is the Ferrocene oxidation onset (a positive value) versus reference electrode, $E_{\text{ox/red}}$ is either a HOMO positive oxidation onset E_{ox} (typically for donors) or a LUMO negative reduction onset E_{red} (typically for acceptors). The Ferrocene HOMO is assumed to be 4.8 below vacuum level.

1.4.6 Organic polymer film-forming processes

Many techniques can be employed to make organic polymer films. Some of the most commonly used methods are described below.

✓ *Spin-Coating*

Spin coating has been used for several decades for the application of thin films. A typical process involves depositing a small puddle of a polymer solution onto the center of a substrate and then spinning the substrate at high speed (typically expressed in rpm). Centripetal acceleration will cause the resin to spread to, and eventually off, the edge of the substrate leaving a thin film of polymer on the surface (see Figure 12). Final film thickness and other properties will depend on the nature of the material (viscosity, drying rate, percent solids, surface tension, etc.) and the parameters chosen for the spin process. Factors such as final rotational speed, acceleration, and fume exhaust contribute to how the properties of coated films are defined. One of the most important factors in spin coating is repeatability. Subtle variations in the parameters that define the spin process can result in drastic variations in the coated film [22].

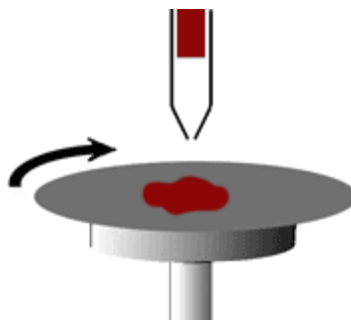


Figure 12: Spin-coating process.

✓ *Langmuir-Blodgett films*

The Langmuir-Blodgett (LB) technique is one of the few methods available for manipulating the architecture of an assembly of organic molecules. The LB technique offers the means to construct similar organic analogs by building up organic layers one monolayer at a time and enables precise geometries (e.g., molecular orientation and thickness) to be constructed. The technique involves spreading some suitable organic molecule onto a water surface, compressing the film to form a compact monolayer, and then transferring this layer to a suitable, substrate.

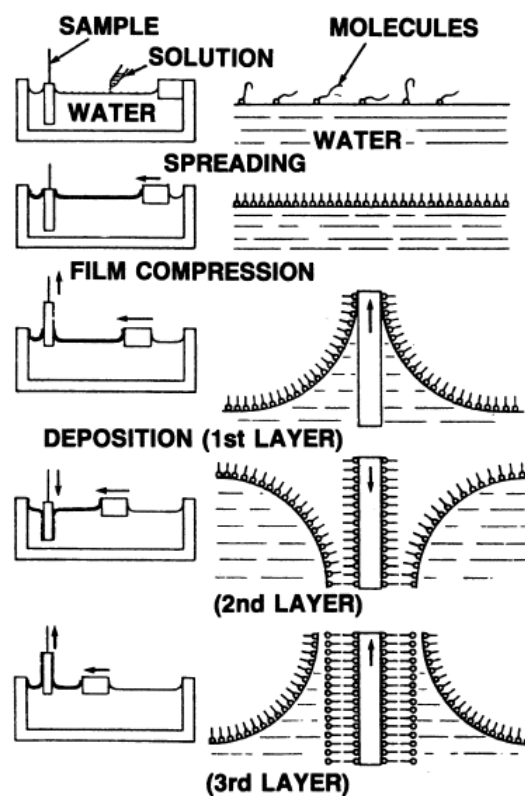


Figure 13: The LB sequence: spreading, compression, and deposition.

The material is usually dissolved in an organic solvent and carefully spread onto the surface of water contained in a Langmuir trough. The concentration is such that the molecules spread to a depth of one monolayer. If the surface pressure F is small, the monolayer behaves as a two-dimensional gas obeying the equation

$$FA = kT \quad (8)$$

where A is the area per molecule, k is Boltzmann's constant, and T is absolute temperature. The surface pressure is increased by compressing the film by means of a sliding barrier. Eventually, a point is reached where all the molecules touch, forming a "perfect" pinhole-free monolayer. The change in surface pressure as the area per molecule is decreased is shown in

Figure 13. The correct degree of compression is determined by monitoring the surface tension of the water, which starts to drop when the molecules are nearly dense-packed. At higher pressures, the monolayer will buckle and collapse. Below the collapse pressure, the monolayer can be transferred to a suitable substrate by lowering the substrate carefully through the film into the water and slowly withdrawing it (

Figure 13). Alternatively, transfer may be effected horizontally by contacting the surface with the substrate oriented horizontally to the film surface. These procedures may be repeated successively until the required number of monolayers is obtained. The thickness will thus be an integral multiple of the length of the amphiphilic species. In this way,

ultrathin, compact, pinhole-free (at least in theory) films of constant, well-controlled thickness can be prepared [17].

1.4.7 Organic Electronics: Commercial Applications

Organic materials have a tremendous potential to transform the world of circuit, display and communication technology in near future. In all of these sectors there is a demand for innovation and development of new technologies and applications leading to great social benefits as well as economical and ecological advantages. Organic materials offer enormous opportunities: They can be readily and cost-effectively synthesized in large amounts. They can be chemically tailored in order to full a specific function with high performance. Furthermore, they are compatible with low-temperature ($< 250\text{ }^{\circ}\text{C}$) and low-cost manufacturing techniques. In the context of consumer electronics can be obtained large-area and low cost manufacturing, especially interesting for large-area full color displays. Moreover, it is possible to obtain flexible and light devices, that hitherto have not been found in other fields of research based on inorganic materials.

Among the most promising electronic and photonic devices are OLEDs, OFETs and OPVs. Rapid advances in materials and manufacturing technology are making OLEDs the leading technology for a new generation of thinner, lighter, higher-resolution displays for computers, televisions, and small hand-held devices. OLED technology is being commercialized as a multi-billion dollar market. OLEDs are already used in small displays in cellular phones, car stereos, digital cameras, hand-held computer games, and other consumer devices such as electric razors and watches. The research activity in OFETs has exploded in recent years. Research has proven that the charge carrier mobilities of a variety

of organic semiconductors is comparable to that of amorphous silicon. One of the key goals now is the integration of these organic transistors using a cost-effective fabrication process. Thin films can be fabricated either by solution processing, which is preferred for high-volume, low-cost production or by vapor deposition, which yields higher performance. For patterning, another plethora of alternatives are available such as printing, stamping, selective dewetting, and inkjet printing. One foreseen, early application for OFET integrated circuits is the radio-frequency identification (RFID) tag. However, even the simplest tags require a few thousand transistors. Much more promising is the introduction of OFETs in active-matrix displays. The transistors are used as switches to turn on and off corresponding pixels. OFET technology has already proven to be successful in that field, since the difficulty of today's OFETs, requiring relatively large bias voltages, is inferior to the advantage offered through large area processing on plastic substrates.

As the evidence for global warming continues to build, it is becoming clear, that we will have to exploit the renewable energy. Photovoltaic offer consumers the ability to generate electricity in a clean, quiet and reliable way. Currently, the main barrier that prevents photovoltaic cells (PV) technology from providing a large fraction of our electricity is the high cost of manufacturing crystalline silicon. If technical difficulties could be surmounted, OPV would constitute an ideal example of large-area, low-cost electronics for organic materials. In the future, is desirable to think if improved materials and device architectures can be fabricated, there is no theoretical reason that prevent OPVs from producing efficiencies that are competitive with commercially produced crystalline silicon PV cells, reaching 10-20%. Organic PV cells seem to represent a viable future technology as a clean and regenerative energy source, generating major social and environmental benefits along

with the profits.

The growth of population and industrial development gave rise to unprecedented air pollution that can cause harm to humans and the environment. Efforts to reduce this pollution include recognition of the problem, collection of information, definition of sources and causes, and the selection and implementation of the appropriate solutions. In order to control the emission levels of pollutants, portable devices using arrays of gas sensors have been developed over recent years. These so-called electronic noses (e-nose) are mainly based on selective layers made from metal oxide semiconductors. However they have been shown some drawbacks, which include their poor selectivity and sensitivity, high operation temperatures, and instability because of response to humidity. Conjugated polymers have been proposed as alternative materials to improve these properties. The easy synthesis, the diversity, and the sensitivity at room temperature are the main advantages of these polymers over inorganic materials. [23]

1.5 ORGANIC FIELD-EFFECT TRANSISTORS (OFETs)

1.5.1 Introduction

Organic field-effect transistor devices are being investigated for a number of low-cost, large-area applications, particularly those that are compatible with flexible plastic circuits. The organic materials that have been used as active semiconductor materials include both sublimed and solution processed semiconductors such as pentacene, oligothiophenes, hexadecafluorocopper, phtalocyanine, polythiophene, etc. This choice of materials opens up several possibilities to develop integrated circuit technologies based on organic transistors for various large area, low-cost applications. Organic polymer transistors have also been integrated with optical devices such as light-emitting diodes, electrophoretic cells and liquid crystals. [24]

1.5.2 Working Principle of FETs

A field-effect transistor (organic or inorganic) requires the following components (shown in Figure 14-a): a thin semiconducting layer, which is separated from a gate electrode by the insulating gate dielectric; source and drain electrodes of width W (channel width) separated by a distance L (channel length) that are in contact with the semiconducting layer.

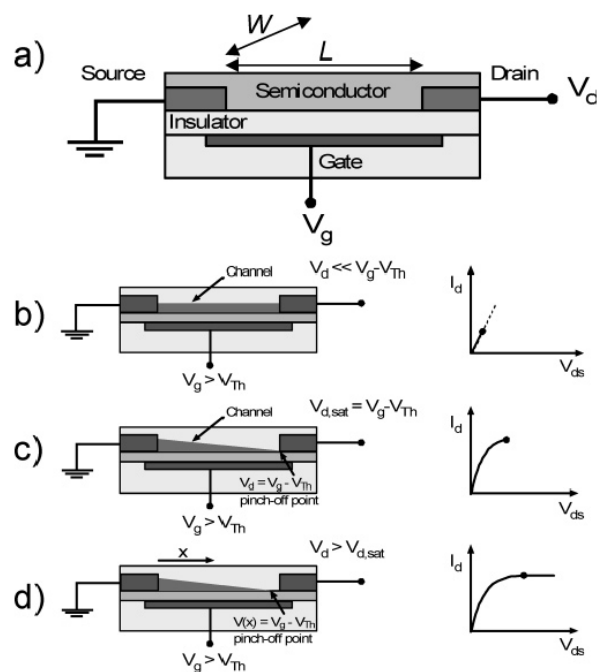


Figure 14: (a) Schematic structure of a field-effect transistor and applied voltages: L = channel length; W = channel width; V_d = drain voltage; V_g = gate voltage; V_{Th}) threshold voltage; I_d) drain current. (b-d) Illustrations of operating regimes of field-effect transistors: (b) linear regime; (c) start of saturation regime at pinchoff; (d) saturation regime and corresponding current-voltage characteristics “Ad. from [25]”.

The semiconducting layer in the case of an organic FET is usually vacuum sublimed, spin-coated, or drop-cast depending on the semiconductor. The gate electrode can be a metal or a conducting polymer, but very often, highly doped silicon serves as substrate and gate electrode at once. As gate dielectrics, inorganic insulators, such as, for example, SiO_2 (thermally grown on Si or sputtered), Al_2O_3 , and Si_3N_4 , or polymeric insulators, such as, for example, poly(methylmethacrylate) (PMMA) or poly(4-vinylphenol) (PVP) are commonly used depending on the transistor structure. The source and drain electrodes, which inject charges into the semiconductor, are usually high work function metals such as

gold (also Pd, Pt, and Ag), but conducting polymers, e.g. poly(3,4-ethylenedioxythiophene), poly(styrenesulfonate) (PEDOT:PSS); polyaniline (PANI), which can be printed, are used as well. Voltage is usually applied to the gate electrode (V_g) and the drain electrode (V_d). The source electrode is normally grounded ($V_s = 0$). The potential difference between the source and the gate is usually just called the gate voltage (V_g), while the potential difference between the source and the drain is referred to as the source-drain voltage (V_{ds}). The source is the charge-injecting electrode, as it is always more negative than the gate electrode when a positive gate voltage is applied (electrons are injected) and more positive than the gate electrode when a negative gate voltage is applied (holes are injected). Figure 14 (b-d) illustrates the basic operating regimes and associated current-voltage characteristics of a field-effect transistor. First we can assume a simple metal-insulator semiconductor (MIS) diode (that is, there is no potential difference between source and drain) with a voltage V_g applied to the gate electrode. A positive gate voltage for example will induce negative charges (electrons) at the insulator-semiconductor interface that were injected from the grounded electrodes. For negative V_g , positive charges (holes) will be accumulated. The number of accumulated charges is proportional to V_g and the capacitance C_i of the insulator. However, not all induced charges are mobile and will thus contribute to the current in a field-effect transistor. Deep traps first have to be filled before the additionally induced charges can be mobile. That is, a gate voltage has to be applied that is higher than a threshold voltage V_{Th} , and thus, the effective gate voltage is $V_g - V_{Th}$. On the other hand, donor (for n-channel) or acceptor (for p-channel) states and interface dipoles can create an internal potential at the interface and thus cause accumulation of charges in the channel when $V_g = 0$ so that in some cases an opposite

voltage has to be applied to turn the channel off. When no source-drain bias is applied, the charge carrier concentration in the transistor channel is uniform. A linear gradient of charge density from the carrier injecting source to the extracting drain forms when a small source-drain voltage is applied ($V_{ds} \ll V_g$, Figure 14-b). This is the linear regime, in which the current flowing through the channel is directly proportional to V_{ds} . The potential $V(x)$ within the channel increases linearly from the source ($x = 0$, $V(x) = 0$) to V_{ds} at the drain electrode ($x = L$, $V(x) = V_{ds}$). When the source-drain voltage is further increased, a point $V_{ds} = V_g - V_{Th}$ is reached, at which the channel is “pinched off” (Figure 14-c). That means a depletion region forms next to the drain because the difference between the local potential $V(x)$ and the gate voltage is now below the threshold voltage. A space-charge-limited saturation current $I_{ds,sat}$ can flow across this narrow depletion zone as carriers are swept from the pinch-off point to the drain by the comparatively high electric field in the depletion region. Further increasing the source-drain voltage will not substantially increase the current but leads to an expansion of the depletion region and thus a slight shortening of the channel. Since the potential at the pinch-off point remains $V_g - V_{Th}$ and thus the potential drop between that point and the source electrode stays approximately the same, the current saturates at a level $I_{ds,sat}$ (Figure 14-d). Note that transistors with short channel lengths require thin gate dielectrics, typically $L > 10d_{dielectric}$, in order to ensure that the field created by the gate voltage determines the charge distribution within the channel (gradual channel approximation) and is not dominated by the lateral field due to the source-drain voltage. Otherwise, a space-charge limited bulk current will prevent saturation and the gate voltage will not determine the “on” or “off” state of the transistor. [25]

1.5.3 Current-Voltage Characteristics

The current-voltage characteristics in the different operating regimes of field-effect transistors can be described analytically assuming the gradual channel approximation. That is, the field perpendicular to the current flow generated by the gate voltage is much larger than the electric field parallel to the current flow created by the drain voltage. This is valid for long channel transistors but starts to fail for very short channel lengths. In the linear regime with $V_{ds} \ll V_g$, the drain current I_d can be described to

$$I_d = \frac{W}{L} \mu_{lin} C_i (V_g - V_{Th}) V_{ds} \quad (9)$$

where W is the channel width, μ is the charge mobility, C_i is the capacitance per unit area of the gate dielectric. The drain current is directly proportional to V_g , and the field-effect mobility in the linear regime (μ_{lin}) can thus be extracted from the gradient of I_d versus V_g at constant V_{ds} (also applicable for gate voltage dependent mobilities).

$$\mu_{lin} = \frac{\partial I_{ds}}{\partial V_g} \cdot \frac{L}{WC_i V_{ds}} \quad (10)$$

The channel is pinched off when $V_{ds} = V_g - V_{Th}$. The current cannot increase substantially anymore and saturates ($I_{ds,sat}$). Thus, Equation 8 is no longer valid. Neglecting channel shortening due to the depletion region at the drain, the saturation current can be obtained by substituting V_{ds} with $V_g - V_{Th}$, yielding

$$I_{ds,sat} = \frac{W}{2L} \mu_{sat} C_i (V_g - V_{Th})^2 \quad (11)$$

In the saturation regime, the square root of the saturation current is directly proportional to the gate voltage. This equation assumes that the mobility is gate voltage independent. If this is not the case, a gate voltage dependent saturation mobility (I_{sat}) can be extracted using

$$\mu_{sat}(V_g) = \frac{\partial I_{ds,sat}}{\partial V_g} \cdot \frac{L}{WC_i} \cdot \frac{1}{V_g - V_{Th}} \quad (12)$$

Figure 15-a shows typical output characteristics (that is the drain current versus source-drain voltage for different constant gate voltages) of a polymer n-channel transistor with a channel length of 200 nm. From the output characteristics, the linear regime at low V_{ds} and the saturation regime at high V_{ds} are evident. Figure 15-b shows the transfer characteristics (that is the drain current versus gate voltage at constant V_{ds}) of the same transistor in the linear regime (V_{ds} , V_g) both as a semilog plot and as a linear plot. From the semilog plot one can easily extract the onset voltage (V_{on}) (the voltage at which the drain current abruptly increases above a defined low off-current level) and the subthreshold swing ($S = dV_g/d(\log I_{ds})$), which depend on the gate dielectric capacitance and the trap states at the interface. The gradient of the current increase in the linear regime is directly proportional to the mobility according to Equation 9 and is constant if the mobility is gate voltage independent. Most semiconductors, however, show gate voltage dependent mobilities, and

thus, the curve shape may deviate from being linear. Figure 15-c shows a transfer curve in the saturation regime. Here the square root of the drain current should be linearly dependent on the gate voltage, and its gradient is proportional to the mobility according to Equation 10. Extrapolating the linear fit to zero yields the threshold voltage V_{Th} . Threshold voltages can originate from several effects and depend strongly on the semiconductor and dielectric used. Built-in dipoles, impurities, interface states, and, in particular, charge traps contribute to the threshold voltage.

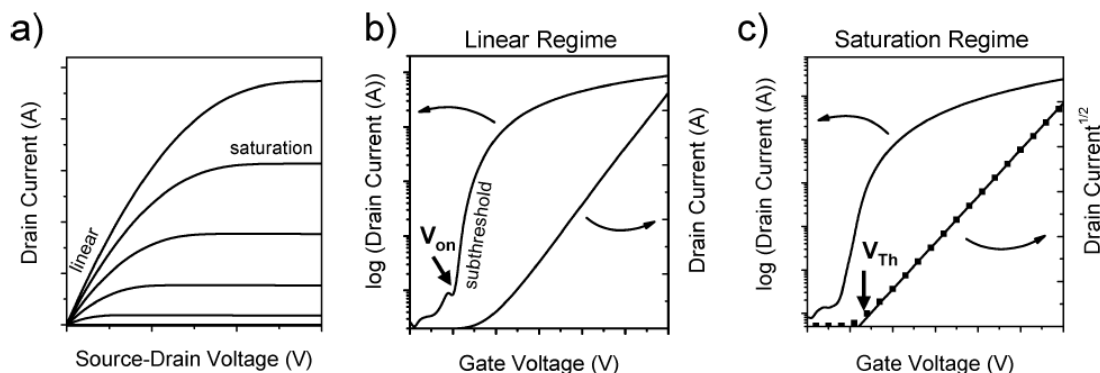


Figure 15: Representative current-voltage characteristics of an n-channel organic field-effect transistor. (a) output characteristics indicating the linear and saturation regimes; (b) transfer characteristics in the linear regime ($V_d \ll V_g$), indicating the onset voltage (V_{on}) when the drain current increases abruptly; (c) transfer characteristics in the saturation regime ($V_{ds} > V_g - V_{Th}$), indicating the threshold voltage V_{Th} , where the linear fit to the square root of the drain current intersects with the x -axis “Ad. from [25]”.

Another important parameter of FETs that can be extracted from the transfer characteristics is the on/off ratio, which is the ratio of the drain current in the on-state at a particular gate

voltage and the drain current in the off-state ($I_{\text{on}}/I_{\text{off}}$). For clean switching behavior of the transistor, this value should be as large as possible.

1.5.4 Device Structure

The most commonly found structures (in relation to the substrate) are the bottom contact contact/top gate (BC/TG, Figure 16-a), bottom contact/bottom gate (BC/BG, Figure 16-b), and top contact/bottom gate (TC/BG, Figure 16-c) structures. Transistors with the same components but different geometries can show very dissimilar behavior.

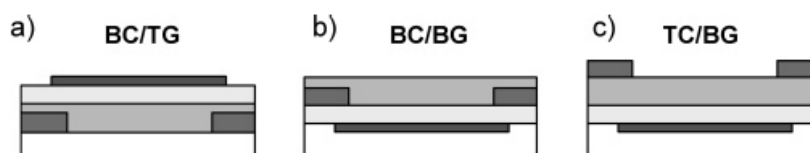


Figure 16: Common field-effect transistor configurations. (a) bottom contact, top gate (BC/TG); (b) bottom contact, bottom gate (BC/BG); (c) top contact, bottom gate (TC/BG). “Ad. from [25]”

One of the major differences between these device geometries arises from the position of the injecting electrodes in relation to the gate. In the bottom contact/bottom gate structure, charges are directly injected into the channel of accumulated charges at the semiconductor-dielectric interface. In the other two structures, the source/drain electrodes and the channel are separated by the semiconducting layer. Thus, charges first have to travel through several tens of nanometers of undoped semiconductor before they reach the channel. However, in the staggered BC/TG and TC/BG configurations, charges are injected not only

from the edge of the electrode but also from those parts of the electrode that overlap with the gate electrode, contributing to the current depending on distance from the edge (current crowding).

1.5.5 Organic Functional Materials for OFET Devices

Efficient FET charge transport and therefore high device performance can be achieved by the use of proper materials and material combination to fabricate the transistor. Source, drain and gate contacts must exhibit large conductivity and ensure ohmic contacts to enhance device speed. The gate dielectric must exhibit large dielectric strength to ensure charge carrier accumulation in FET channel upon application of the gate field. As far as the most important FET materials is concerned, the organic semiconductor, it must satisfy general criteria relating both injection and current-carrying characteristics, in particular: (i) HOMO and LUMO energies of the individual molecules must be at levels where holes/electrons can be incorporated at accessible applied electric field, (ii) solid should be extremely pure since impurities act as charge carrier traps, (iii) molecules should be preferentially orient with the long molecular axes approximately perpendicular to the FET substrate in order to have charge transport along the direction of intermolecular π - π stacking, (iv) crystalline domains of the semiconductor must cover the area between source and drain contacts uniformly. [26]

The development of new materials for p-channel transistors continues to be a major area of research. Apart from high mobilities, major objectives are stability under ambient conditions and under bias stress, as well as easy processing, e.g., from solution, which would make organic semiconductors a viable alternative to amorphous silicon. For small

molecule, thin-film transistors, pentacene (Figure 17) is still the material with the highest mobility, but it must be vacuum sublimed, while solution processing is technologically more practical. Various solution processable precursor forms of pentacene were synthesized and tested in field-effect transistors, but they usually did not show as high mobilities as vacuum-sublimed films. Recently, new soluble pentacene derivatives with triisopropylsilylethynyl groups at the 6,13-positions (Figure 17) were reported that show

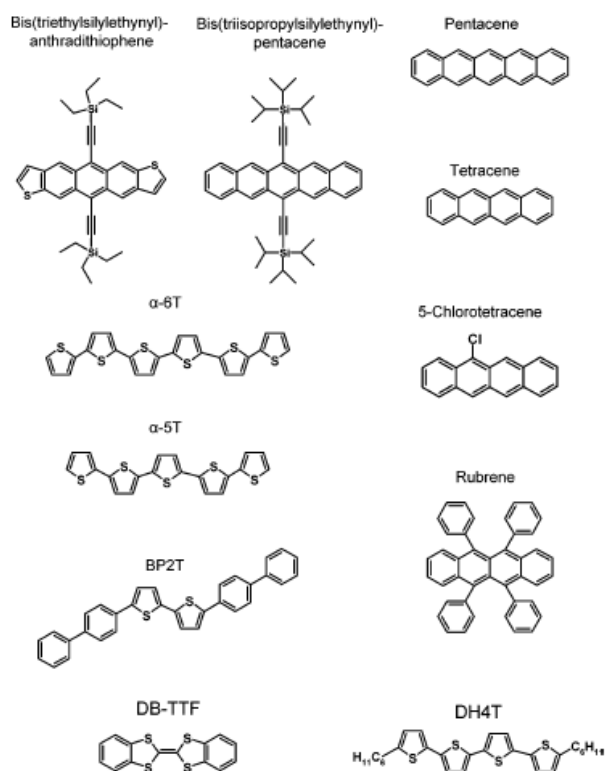


Figure 17: Small molecule semiconductors, which are commonly known for their hole channel characteristics in field-effect transistors “Ad. from [25]”.

hole mobilities of up to $0.17 \text{ cm}^2\text{V}^{-1}\text{s}^{-1}$ [25]. Similarly functionalized anthradithiophenes (triethylsilylethynyl anthradithiophene, Figure 17) showed even higher mobilities of up to $1 \text{ cm}^2\text{V}^{-1}\text{s}^{-1}$, probably due to improved π -stacking. Solution processable polymer semiconductors for p-channel transistors have also shown improved mobility and stability under ambient conditions in recent years. One of the most promising building blocks for polymer semiconductors remains thiophene. Regioregular poly(3-hexylthiophene) (P3HT, Figure 18) used to be the conjugated polymer with the highest hole mobilities of up to $0.1 \text{ cm}^2\text{V}^{-1}\text{s}^{-1}$ depending on processing conditions. P3HT, however, is very susceptible to unintentional doping due to its relatively low ionization potential (4.8 eV) and thus shows poor performance under ambient conditions [25]. In order to increase the ionization potential while maintaining good transport properties, the conjugation length and thus delocalization of charges should be reduced. This can be achieved, e.g., by attaching alkyl chains only to some thienylene moieties and thus allowing more rotational freedom, which reduces the conjugation length. In fact, has been proved this concept for poly(3,3''-dialkylquaterthiophene)s (PQT-12, Figure 18), which exhibit high field-effect mobilities and good air stability.[25] An alternative approach is to incorporate a fused aromatic heterocycle that cannot form an extended conjugated pathway with both its neighboring monomer units, as shown for thieno[2,3-*b*]thiophene with sulfur atoms in *syn* position. Recently, the same approach using thieno[2,3-*b*]thiophene with sulfur atoms in *anti* position (Figure 18) yielded a liquid crystalline, reasonably air-stable semiconducting polymer that forms large crystals after annealing and shows the highest hole mobilities demonstrated for a semiconducting polymer up to now ($0.6 \text{ cm}^2\text{V}^{-1}\text{s}^{-1}$) [25].

One of the main challenges of fabricating a n-channel transistor is the injection of electrons into the LUMO level of the semiconductor from a suitable electrode. For p-channel transistors, the injection of holes into the HOMO level is easily achieved using

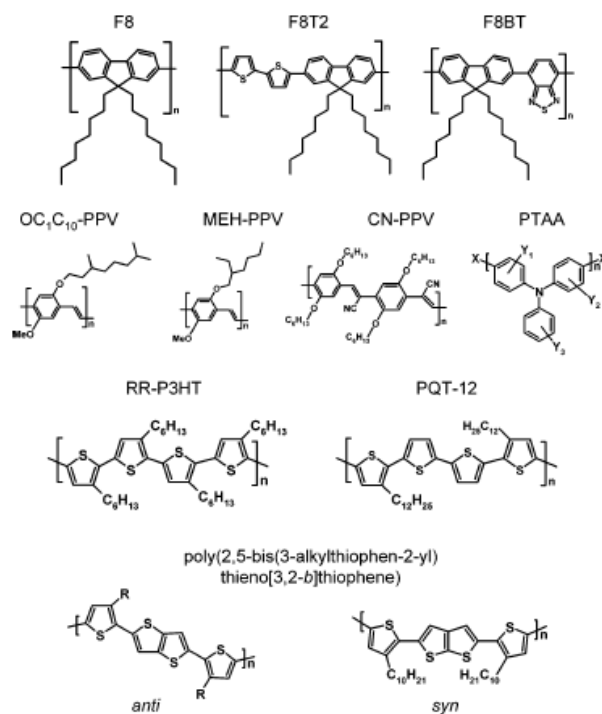


Figure 18: Conjugated semiconducting polymers that have shown hole and, in some cases, electron field-effect transport “Ad. from [25]”.

gold electrodes because the HOMO level of many organic semiconductors is in the range of 4.8 to 5.3 eV, which aligns well with the work function of gold (4.8-5.1 eV). The LUMO level, on the other hand, often lies much higher, at around 2-3 eV. When gold electrodes are used in this case, observation of n-channel behavior cannot be expected due to the extremely high injection barrier of 2-3 eV. In order to inject electrons, one needs to

use low work function metals, such as calcium, magnesium, or aluminum, that are not environmentally stable. Most newly synthesized organic semiconductors are tested using convenient gold electrodes, and thus n-channel transport may not be observed due to the misalignment of the LUMO level with the work function of gold. Another major obstacle is the susceptibility of organic semiconductors to water and oxygen under ambient conditions. Organic radical anions as they are present in the channel when a positive gate voltage is applied have a very high reducing power and can thus react with water or oxygen that have diffused into the organic film. In fact, it is necessary to stabilize the charge carriers in electron transport materials with respect to H₂O reduction. This means that the LUMO of these molecules should lie at an energy below approximately -3.7 eV with respect to vacuum. However, molecular materials in which negatively charged carriers are not thermodynamically susceptible to O₂ oxidation would require a far more daunting reduction potential of greater than 0.57 V, and thus, LUMO energies less than -4.9 eV. However, an overpotential to the charge carrier O₂ reaction could, in principle, prevent ambient trapping in materials where the LUMO energies are considerably less negative. Recent experimental and theoretical studies empirically identified this energetic threshold at approximately -4.0 to -4.3 eV, which scales to an overpotential versus O₂ reduction of approximately 0.9 to 0.6 V. [27]. In order to fabricate n-channel transistors that can be processed under the same conditions and with the same electrodes as those used for p-channel transistors, many new materials were synthesized. A number of design rules have guided the search for these so-called “n-type” semiconductors. In order to be able to inject electrons into the LUMO level from environmentally stable electrodes, such as gold, the LUMO level must be lowered (i.e., increasing the electron affinity) substantially in order to

align with the work function of the metal. At the same time, increasing the electron affinity of a semiconducting material also improves its environmental stability, that is, its sensitivity to oxygen and water. On the basis of known n-channel transistors, it was generally assumed that a high electron affinity (at least 3 eV) is necessary to observe n-channel behavior. This is achieved by taking a known semiconducting core molecule and adding strong electron withdrawing groups such as fluorine, cyano, or diimide moieties. At the same time, the molecular packing of those molecules might be altered due to these changes, which could impede or improve electron transfer.

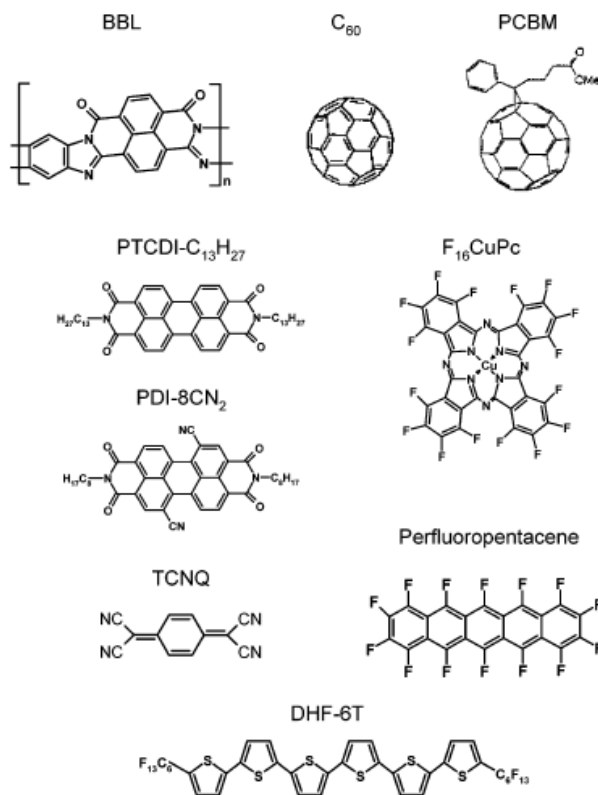


Figure 19: Organic semiconductors that show predominantly n-channel behavior in transistors with SiO₂ as a gate dielectric and gold source-drain electrodes “Ad. from [25]”.

A class of molecules with exceptionally high electron affinity are the fullerenes and their derivatives (e.g., C60 and PCBM, Figure 19). They were shown to yield n-channel transistors with very high electron mobilities. Although a high electron affinity improves the environmental stability of the organic semiconductor, the radical anion remains thermodynamically unstable, especially toward oxygen in the presence of water. A kinetic barrier against diffusion of water and air into the active channel region during operation is needed. Very close packing of molecules, as was shown for fluorinated copper phthalocyanine, seems to be beneficial in that respect. Very few of the demonstrated n-channel transistors are stable under ambient conditions; among them are transistors based on fluorinated copper phthalocyanine (FCuPC), dicyanoperylene-3,4:9,10-bis(dicarboximide) (PDI-8CN2), and α,ω -diperfluorohexylsexithiophene (DHF-6T) (chemical structures in Figure 19). In addition to stability and energetic considerations, the orientation of molecules to each other and the associated transfer integrals of electrons play a role. The best LUMO-LUMO overlap for electron transport may be different from the ideal HOMO-HOMO overlap for hole transport. The molecular packing in crystalline semiconductors can strongly affect the observation of p- or n-channel characteristics. This may be less important for amorphous polymer semiconductors. Nevertheless, one of the few conjugated polymers showing n-channel behavior until recently was poly(benzobisimidazobenzophenanthroline) (BBL, Figure 19).

1.6 ORGANIC SENSORS

1.6.1 Introduction

Desired properties of a chemical sensor include high sensitivity, a large dynamic range, high selectivity or specificity to a target analyte, related low cross-sensitivity to interferences, perfect reversibility of the physicochemical detection or sensing process (short sensor recovery and response times), and long-term stability of the sensor and sensing material. Unfortunately, a sensor exhibiting all these properties is a largely unrealizable ideal. Sensor sensitivity, selectivity, speed of response, and reversibility are determined by the thermodynamics and kinetics of sensor material/analyte interactions. In particular, high sensitivity and specificity on the one hand and perfect reversibility on the other hand impose contradictory constraints on the sensor design: high sensitivity and selectivity are typically associated with strong interactions, whereas perfect reversibility requires weak interactions. Consequently, it is necessary to compromise, and, in most cases, sensors showing partial selectivity to only some of the detected species are used to ensure reversibility. [28]

The basic strategy for the design of a chemical sensor is to connect a molecular recognition site (receptor site) with a signaling unit in such a way that these two functional components communicate. In such a system, a binding event between the receptor site and a target analyte triggers a change in the measurable properties of the materials. Hence, simply stated, factors that can be modified by molecular design are the affinity between the receptor site and the target analyte (i.e. binding constant (K) and selectivity) and the transduction efficiency of the binding event into an observable signal. The interaction of

the analytes with organic polymers can cause changes in their color, mass, work function and electrical conductivity. In particular, the transport properties of these materials can provide these types of amplification and both the mobility of excitons (excited states) and charge carriers (electrons/holes) in conjugated polymers are dramatically influenced by small perturbations.

1.6.2 Volatile Organic Compounds (VOCs) Detection: Transduction Mechanism

An advantage of polymeric materials is that sensory devices can easily be fabricated from these materials on electrodes either by spin coating and/or drop casting from solution or anodic electrochemical polymerization from an electrolyte solution. The electrode configuration of the sensor will vary according to the sensing mechanism. A potentiometric and amperometric signal can be read through a single electrode. Conductometric sensory devices, on the other hand, are most easily monitored by passing charge between two electrodes. The conductance of a material is a bulk transport property and as a result is more sensitive than potentiometric and amperometric methods that are dependent on local electronic structure.

Most conductive polymers, such as polyaniline (PANI), polypyrrole (PP) and poly(phenylene sulphide-phenyleneamine) (PPSA), are p-type semiconductors, unstable in the undoped state. In contrast, polythiophene (PT) films are stable when undoped or very lightly doped. The primary dopants (anions), introduced during the chemical or electrochemical polymerization, generally increase the electrical conductivity. Primary doping can be accomplished chemically or electrochemically, and its level depends on the type of the dopant and on its distribution in the polymer. The nature of the anion strongly

influences the morphology of the polymer. Anions can also serve as specific binding sites for interaction of the polymer with the analyte gas. The introduction of an electrically neutral gas into a conductive polymer can be seen as adding an ‘inert’ secondary dopant, which, when applied to a primary-doped polymer, induces still further changes in its electronic, optical or magnetic properties. The effects of secondary doping are based primarily on a change in molecular conformation of the polymer from compact to expanded coil. Changes in the electronic properties are related to changes of electronic coupling between redox sites in the matrix that define a physical electron transfer pathway in the conductive polymer, recognized in conductivity and work function. The electron transfer pathway relies on the premise that covalent bonds, hydrogen bonds and Van der Waals contacts between atoms modulate electronic coupling differently. The magnitude of the electronic coupling depends on the extent of these chemical interactions. A secondary dopant differs from a primary dopant in that a charge transfer between the dopant and the polymer is carried out. The affinity of the conductive polymer for the secondary dopant can be increased by introducing specific binding sites, creating template-synthesized nanostructures or using post-treatments. As an example, Figure 20 illustrates typical response cross-sensitivity for different types of sensing materials toward a variety of vapors. In Figure 21 has been reported the simplest form of chemiresistor. It consists of a pair of electrodes forming contacts to the polymer, deposited on an insulating substrate.

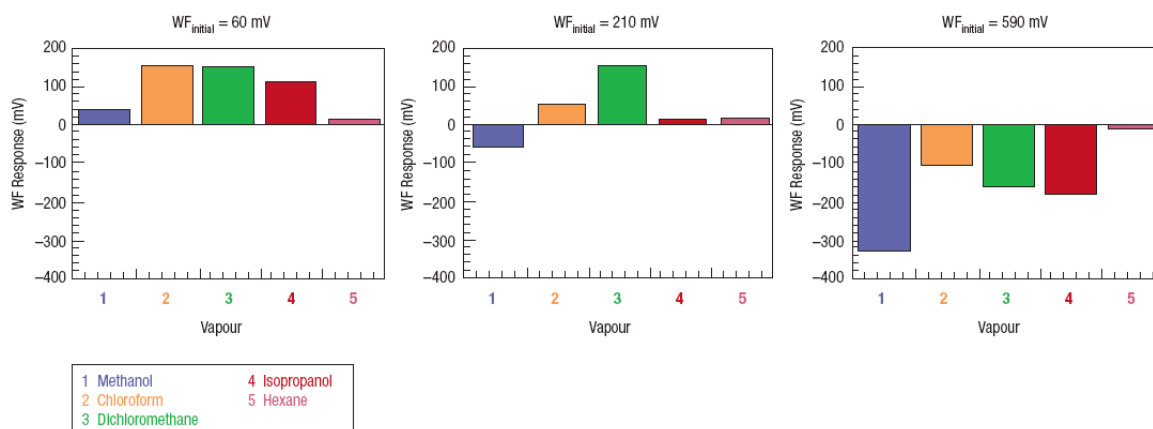


Figure 20: Comparison between the work-function responses of conducting polymer layers to different vapors. Initial work function (versus Au reference) was adjusted electrochemically to different initial values “Ad. from [28]”.

When a constant current is applied, the resulting potential difference at the electrodes becomes the response signal. But the simplicity of this sensing concept and its realization comes at a price.

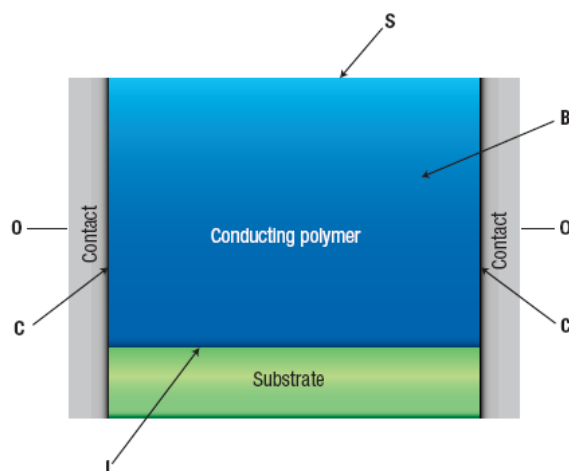


Figure 21: Chemiresistor. B:bulk of the conducting polymer. S:surface. I:interface with the insulating substrate. C:interface with the contacts “Ad. from [28]”.

As the polymer interacts with gaseous species it can act either as an electron donor or an electron acceptor. If a p-type polymer donates electrons to the gas its hole conductivity increases. Conversely, when the same polymer acts as an electron acceptor its conductivity decreases. Besides the change in the number of carriers, there can be a change in their bulk mobility. It is usually due to conformational changes of the polymer backbone. Disadvantages of the response originating in the bulk of the conductive polymers are the relatively long time constant (tens of seconds to minutes), often accompanied by hysteresis. These effects are caused by slow penetration of gases into the organic material. [29]

1.6.3 Conducting Polymers for Volatile Organic Compounds (VOCs) Detection

Examples of conjugated polymers and their derivatives demonstrated for gas sensing with wireless and low-power transducers include polyaniline, polythiophenes, polypyrrole, polypyrroles and poly(vinyl ferrocene). Conjugated polymers (e.g., poly(flourene)diphenylpropane) originally developed for OLEDs have also been demonstrated with wireless resonant sensors as sensing materials with significantly suppressed humidity effects. Formulation of conjugated polymers with different dielectric and highly conducting additives provides an way to expand the diversity of response selectivity to different gases. Recently, two “classic” conjugated polymers with diverse response mechanisms to different vapors were applied to transducers these independent changes and to demonstrate the power of passive wireless sensors. Poly(3,4-ethylenedioxythiophene) (PEDOT) was formulated with poly-(4-styrenesulfonate) (PSS) and employed for sensing of acetonitrile (ACN), ethanol (EtOH), and water (H₂O) vapors [29]. The response mechanism of PEDOT-PSS to polar organic vapors involves

conformational changes within the polymer chains due to the interaction between the dipoles of the vapors and dipoles or charges on the polymer chains. For example, the H₂O vapor-response mechanism has been shown to involve dipole molecular effects with the polar PEDOT-PSS formulation. Another “classic” polymer, polyaniline (PANI), was formulated with camphorsulfonic acid (CSA) and employed for sensing ammonia (NH₃) and H₂O vapors [29]. The response mechanism of PANI-CSA to NH₃ involved polymer deprotonation, whereas the response mechanism to H₂O involved formation of hydrogen bonds and swelling. New conjugated polymers have been synthesized and implemented for VOCs detection with detection limits down to the low part per-million-high part-per-billion range with reduced humidity effects. Poly(fluorene)diphenylpropane polymer was applied onto a sensor and exposed to different concentrations of trichloroethylene (TCE), water, and toluene vapors. Several routes to improve the selectivity and stability of conjugated polymers have been identified, including chemical modifications (e.g., side-group substitution of heterocycles, copolymerization, introduction of end-groups), doping, charge compensation for oxidized polymers by incorporation of functionalized counterions, formation of organic-inorganic hybrids, and surface functionalization. Rational manipulation of polymerization conditions can also be used to control sensor-related properties of conjugated polymers (e.g., molecular weight, monomer connectivity, conductivity, band gap, and morphology). It has been found that, under certain conditions, regioregular poly(3-hexylthiophenes) self-assemble into highly ordered and partially crystalline structures with improved charge carrier mobility [29]. A field-effect transistor readout was well suited to benefit from the improved field effect mobility in these conjugated polymers. Good contacts between the polythiophene polymer and the metal

electrodes of a chemiresistor sensor were provided by combining nanotransfer printing and solventless polymerization. Vapor-based polymerization of thiophene resulted in a highly oriented polythiophene film. Deposition methods for conjugated polymers can facilitate the formation of different morphologies. For example, inkjetted films can exhibit significantly different structures compared to films drop-cast from low vapor pressure solvents. The increased drying time of regioregular poly(3-hexylthiophene) polymer solution allowed polymer molecules to self-assemble into dense 10-30 nm wide nanofibril structures when drop-cast [29].

1.7 ORGANIC SOLAR CELLS

1.7.1 Introduction

Until very recently, the development of solar photovoltaic systems has been essentially related to inorganic semiconductors, in particular polycrystalline silicon. While the maximum yields approach 25%, the high cost of fabrication of the raw materials yields only limited commercial developments. Alternatives using micro-crystalline or amorphous silicon have been widely studied; and maximum yields are close to 15%. Nevertheless, costs remain problematic due to the use of highly polluting materials, leaving inorganic solar cells as poor competitors against other more prevalent energy sources. In parallel, the use of organic semiconductors developed during the 1970s and 1980s was envisaged as a possible route. There are many foreseeable advantages in commercializing organic and polymer-based photovoltaic (PV) systems, including ease of fabrication and manipulation, flexibility, low weight and low cost. [31] In fact, deposition of organics by screen printing, doctor blading, inkjet printing, and spray deposition is possible because these materials can be made soluble. Additionally, these deposition techniques all take place at low temperature, which allows devices to be fabricated on plastic substrates for flexible devices. In addition to the inherent economics of high-throughput manufacturing, light weight and flexibility are qualities claimed to offer a reduction in the price of PV panels by reducing installation costs. Flexible PV also opens up niche markets like portable power generation and aesthetic PV in building design. [32]

1.7.2 Principle of Operation

Organic solar cells have a planar-layered structure, where the organic light-absorbing layer is sandwiched between two different electrodes. One of the electrodes must be (semi-) transparent, often Indium–tin–oxide (ITO), but a thin metal layer can also be used. The other electrode is very often aluminum (calcium, magnesium, gold and others are also used). Basically, the underlying principle of a light-harvesting organic PV cell (sometimes referred to as photodetecting diodes) is the reverse of the principle in (LEDs) (Figure 22) [33]

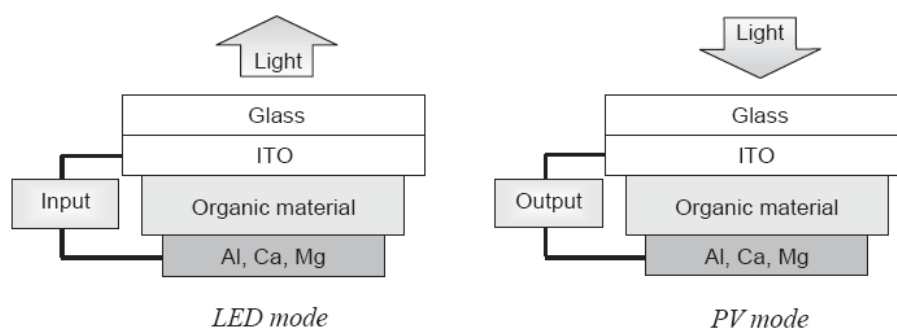


Figure 22: A PV device (right) is the reverse of a LED (left). In both cases an organic material is sandwiched between two electrodes. In PVs electrons are collected at the metal electrode and holes are collected at the ITO electrode. The reverse happens in a LED: electrons are introduced at the metal electrode (cathode), which recombine with holes introduced at the ITO electrode (anode) “Ad. from [33]”.

In LEDs an electron is introduced at the low-workfunction electrode (cathode) with the balanced introduction of a hole at the high-workfunction electrode (anode). At some point the electron and the hole meets, and upon recombination light is emitted. The reverse happens in a PV device. When light inside on device, one photon is absorbed: electron-hole

pairs (excitons) are generated at the *p*-type donor material due to electron transitions from π -HOMO to π^* -LUMO bands (Figure 23).

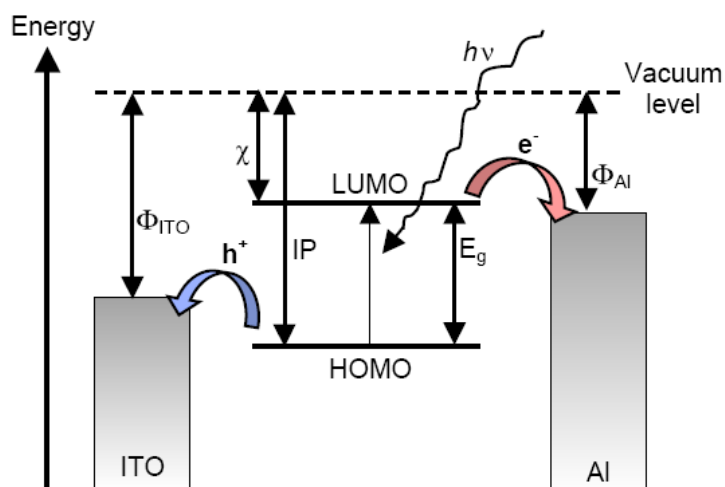


Figure 23: Energy levels and light harvesting. Upon irradiation an electron is promoted to the LUMO leaving a hole behind in the HOMO. Electrons are collected at the Al electrode and holes at the ITO electrode. Φ : workfunction, χ : electron affinity, IP: ionization potential, E_g : optical bandgap “Ad. from [33]”.

The generation of an electron-hole pair, by photoexcitation, results in an excited but neutral state with a limited, finite lifetime; this state is termed an exciton and consists of an electron and a hole paired by an energy (E_{ex}) that is smaller than the energy gap between the limits of the permitted bands (LUMO and HOMO bands, respectively). If E_g is the energy gap, then $(E_g - E_{ex})$ is the exciton binding energy (around 0.1-0.2 eV in organics). The occupation of these excited states, the LUMO by the electron, and the HOMO by the hole, is termed a nonrecombined exciton, generally observed in organic materials. This quasi-particle diffuses inside the donor material as long as recombination processes (of the

hole-electron pair which makes up the exciton) do not take place. Förster (long range) or Dexter (between adjacent molecules) transfers can take place between an excited molecule (considered as excitation donor) and a molecule that receives the excitation (excitation acceptor). If the diffusion length is sufficiently long that the exciton meets an internal field, hole and electron separation occurs. The internal field may be obtained at a donor-acceptor interface, provided the LUMO level of the acceptor is lower than the excitonic state located at the bottom of the conduction band of the donor. More precisely, the condition which must be fulfilled is $E_{\text{ex}} > I_{\text{pd}} - \chi_{\text{Ea}}$, where I_{pd} is the ionization energy of the acceptor, and χ_{Ea} is the electronic affinity of the acceptor. ($[I_{\text{pd}} - \chi_{\text{Ea}}]$ is the energy of electron and hole just after the charge transfer at the donor-acceptor interface). Moreover, excitons are considered to be localized on specific chain segments. In simple PV devices and diodes based on organic semiconductors the primary exciton dissociation site is at the electrode interface. This limits the effective light-harvesting thickness of the device, since excitons formed in the middle of the organic layer never reaches the electrode interface if the layer is too thick. Typical exciton diffusion distances are on the order of 10 nm. Afterwards, carriers migrate towards the electrodes. This transport involves the classic mechanism for hopping processes in organic materials. Traps can reduce the mobility.

1.7.3 Electronic Donor-Acceptor Interactions

Recently, two main approaches have been explored in the effort to develop PV viable devices: the donor-acceptor bilayer, commonly achieved by vacuum deposition of molecular components, and the so-called bulk heterojunction (BHJ), which is represented in the ideal case as a bicontinuous composite of donor and acceptor phases, thereby

maximizing the all-important interfacial area between the donors and acceptors. The real advantage of these BHJ devices, which can be processed in solution, over vacuum deposition is the ability to process the composite active layer from solution in a single step, by using a variety of techniques that range from inkjet printing to spin coating and roller casting. [34] However, regardless of the preparation's method, one feature that extends across all classes of organic solar cells is the almost ubiquitous use of fullerenes as the electronaccepting component. The high electron affinity and superior ability to transport charge make fullerenes the best acceptor component currently available for these devices. The state-of-the-art in the field of organic photovoltaics is currently represented by BHJ solar cells based on poly(3-hexylthiophene) (P3HT) and the fullerene derivative [6,6]-phenyl-C61-butyric acid methyl ester (PCBM), with reproducible efficiencies approaching 5%. In principle, the optimization of polymer-fullerene solar cells is based on fine-tuning of the electronic properties and interactions of the donor and acceptor components, so as to absorb the most light, generate the greatest number of free charges, with minimal concomitant loss of energy, and transport the charges to the respective electrodes at a maximum rate and with a minimum of recombination. The first constraint is that the donor must be capable of transferring charge to the fullerene upon excitation (Figure 24). A downhill energetic driving force is necessary for this process to be favorable and the driving force must exceed the exciton binding energy. This binding energy is the Coulombic attraction of the bound electron-hole pair in the donor, and typical values are estimated to be 0.4-0.5 eV.

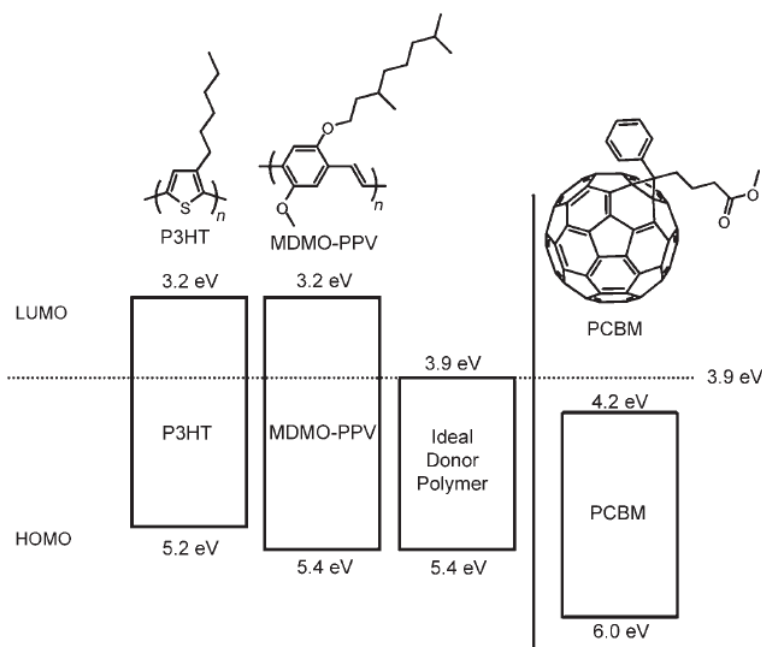


Figure 24: Band structure diagram illustrating the HOMO and LUMO energies of MDMO-PPV, P3HT, and an “ideal” donor relative to the band structure of PCBM. Energy values are reported as absolute values relative to a vacuum “Ad. from [34]”.

1.7.4 Determination of Photovoltaic Performance

The photocurrent action spectrum of solar cells is very informative for the characterization of new materials in a device. It represents the ratio of the observed photocurrent divided by the incident photon flux as a function of the excitation wavelength and is referred to as the incident photon-to-current conversion efficiency (IPCE). [35] The photocurrent which is normally measured is obtained outside the solar cell device; therefore, IPCE can also be named as external quantum efficiency (EQE), e.g. the current obtained outside the photovoltaic device per incoming photon, that is the ratio of the

number of carriers collected by the solar cell to the number of photons of a given energy incident on the solar cell:

$$IPCE(\lambda) = \frac{n_{electrons}}{n_{photons}} = \frac{I/e}{P/h\nu} = \frac{I}{P} \times \frac{hc}{e\lambda} = \frac{I}{P} \times \frac{1240}{\lambda(\text{nm})} \quad (13)$$

where I is the photocurrent in Am^{-2} and P is the incident light power in Wm^{-2} . By recording the photocurrent response while continuously varying the wavelength of the incident light, the conversion efficiency of photons to electrons, namely IPCE, can be determined. The IPCE value is expressed as a product of three factors:

$$IPCE(\lambda) = LHE(\lambda) \times \Phi_{inj} \times \Phi_{col} \quad (14)$$

where $LHE(\lambda)$ is the light-harvesting efficiency of active materials, Φ_{inj} is the charge injection efficiency between the active materials, and Φ_{col} is the charge collection efficiency at the external electrodes. The maximum IPCE value ($IPCE_{max}$) is a key parameter for describing the device and correlating the performance to the dye absorption and thereby its molecular structure. The higher the $IPCE_{max}$ and the broader the spectrum, the higher the photocurrent will be (I_{sc} corresponds to the integral IPCE curve). A quantum efficiency curve for an ideal solar cell is shown in Figure 25. While quantum efficiency ideally has the square shape shown above, the quantum efficiency for most solar cells is reduced due to recombination effects. The same mechanisms which affect the collection probability also affect the quantum efficiency. For example, front surface passivation

affects carriers generated near the surface, and since blue light is absorbed very close to the surface, high front surface recombination will affect the "blue" portion of the quantum efficiency. Similarly, green light is absorbed in the bulk of a solar cell and a low diffusion length will affect the collection probability from the solar cell bulk and reduce the quantum efficiency in the green portion of the spectrum. The quantum efficiency can be viewed as the collection probability due the generation profile of a single wavelength, integrated over the device thickness and normalized to the incident number of photons. [36]

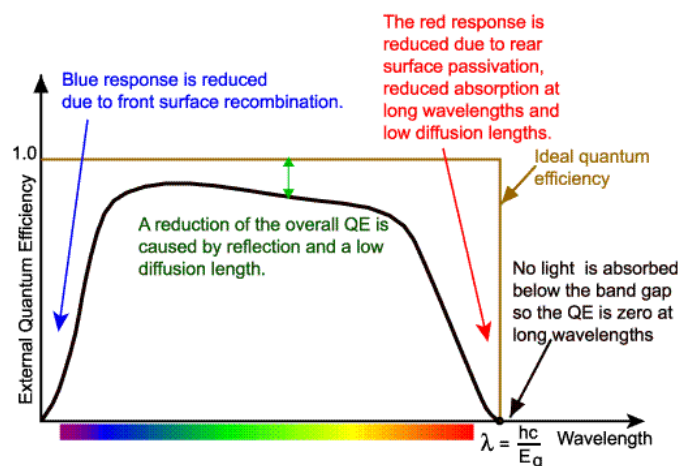


Figure 25: The quantum efficiency of a silicon solar cell “Ad. from [36]”.

Therefore, the photocurrent action spectrum inspects the ability of the solar cells to convert photons to electrons under the irradiation of light with various wavelengths or intensities, which gives the reference of the photon to electron transfer capability of solar cells. However, to decide whether a solar cell has the potential to be commercialized or not, the most efficient method is to measure the photocurrent and photovoltage under the simulated

AM 1.5 solar light. The overall power conversion efficiency (PCE), η , is calculated according to the following equation:

$$\eta = \frac{P_{out}}{P_{in}} = FF \frac{V_{oc} I_{sc}}{P_{in}} \quad (15)$$

where P_{out} is the maximum output electrical power (in Wm^{-2}) of the device under illumination, P_{in} (in Wm^{-2}) is the light intensity incident on the device, V_{oc} is the open circuit voltage, and I_{sc} is the short circuit current in A m^{-2} . The parameter FF is known as the fill factor, which is defined as

$$FF = \frac{V_{mpp} I_{mpp}}{V_{oc} I_{sc}} \quad (16)$$

where V_{mpp} and I_{mpp} are the voltage and current at the maximum power point in the I - V curve, respectively. A typical solar cell I - V curve is shown in Figure 26. When a cell is illuminated, the I - V curve is shifted down by the short-circuit current, (Figure 26 right). The open-circuit voltage, is the maximum voltage difference attainable between the two electrodes, typically around 0.5-1.5V, which is higher than inorganic cells. An ideal device would have a rectangular shaped I - V curve and therefore a fill factor $FF \approx 1$. At some point the charge build-up will reach a maximum equal to the V_{oc} that is limited by the difference in workfunctions of the two electrodes. The maximum current that can run through the cell is determined by the short-circuit current. This quantity is determined by connecting the

two electrodes, whereby the potential across the cell is set to zero, and then illuminating the cell while the current flow is measured. I_{sc} yields information about the charge separation and transport efficiency in the cell.

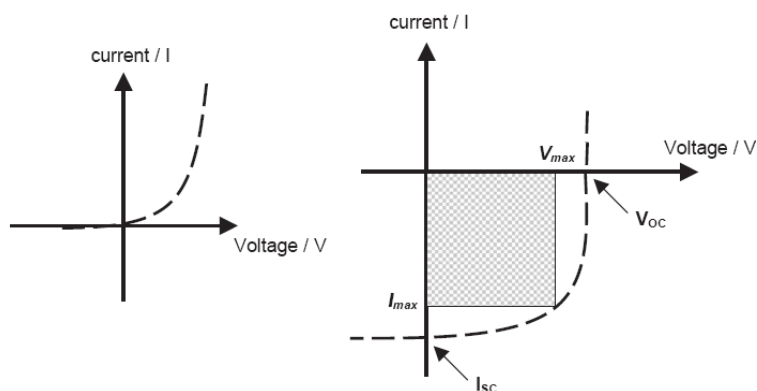


Figure 26: I-V curves of an organic PV cell under dark (left) and illuminated (right) conditions. The open-circuit voltage (V_{oc}) and the short-circuit current (I_{sc}) are shown “Ad. from [33]”.

1.7.5 Organic Functional Materials for Photovoltaic Cells

The prototypical BHJ solar cells based on MDMO-PPV/PCBM and P3HT/PCBM composites discussed above (Figure 24), show the extent of optimization that is required to generate efficient polymer-fullerene solar cells. The photon flux reaching the surface of the earth from the sun occurs at a maximum of approximately 1.8 eV (700 nm); however, neither MDMO-PPV ($E_g = 2.2$ eV) nor P3HT ($E_g = 1.9$ eV) can effectively harvest photons from the solar spectrum. It is calculated that P3HT is only capable of absorbing about 46% of the available solar photons and only in the wavelength range between 350 nm and 650

nm. The limitation in the absorption is primarily due to limited spectral breadth rather than the absorption coefficient, as conjugated polymers typically have extremely high absorption coefficients on the order of 10^5 cm^{-1} . Developing a polymer that could capture all of the solar photons down to 1.1 eV would allow absorption of 77% of all the solar photons. Expanding the spectral breadth of absorption in polymer-fullerene composites has most commonly been pursued by extending (or shifting) the polymer absorption spectrum into the near-infrared region. This is primarily achieved through the use of low-bandgap polymers, which has led to efficiencies as high as 3.5% in polymer-fullerene composite solar cells. While low-bandgap polymers have often been touted as the solution of this problem, merely having a lower energy onset for absorption is not sufficient to harvest more solar photons. What is needed is to extend the overlap with the solar spectrum to gain broader chromophores that are conjugated to the backbone leads to a broadening of the wavelengths at which high photoconversion efficiencies can be achieved. In a direct comparison with P3HT/PCBM devices, cells with polymer 1 (Figure 27) afforded 3.2% efficiency versus 2.4% with P3HT under the same conditions. The enhanced performance of polymer 1 can be attributed to the increased photocurrent in the 400–500 nm range. It is interesting to note that despite its irregular structure, copolymer 1 is able to afford highly efficient solar cells when blended with PCBM in a 1:1 ratio. Other examples of poly(3-vinylthiophenes) have also been reported to achieve efficiencies greater than 1%. The second and most common approach to increasing the spectral breadth of absorbed photons is the use of so-called low-bandgap polymers, which are loosely defined as polymers with a bandgap less than 1.5 eV. However, in terms of polymer-based photovoltaic systems, any polymer with a bandgap less than that of P3HT (that is, $<1.9 \text{ eV}$) is often referred to as a

low-bandgap polymer. In several cases efficiencies in the range of 1 to 3.5% have been achieved. Compounds 2-7 (Figure 27) represent a few of the more successful polymers employed to-date. The most common synthetic technique used to achieve low-bandgap polymers is the donor-acceptor approach, in which alternating electron-rich and electron-poor units define the polymer backbone. The best examples of this class reported thus far are based almost exclusively on benzothiadiazole (or analogues) as the acceptor in combination with several different donor groups.

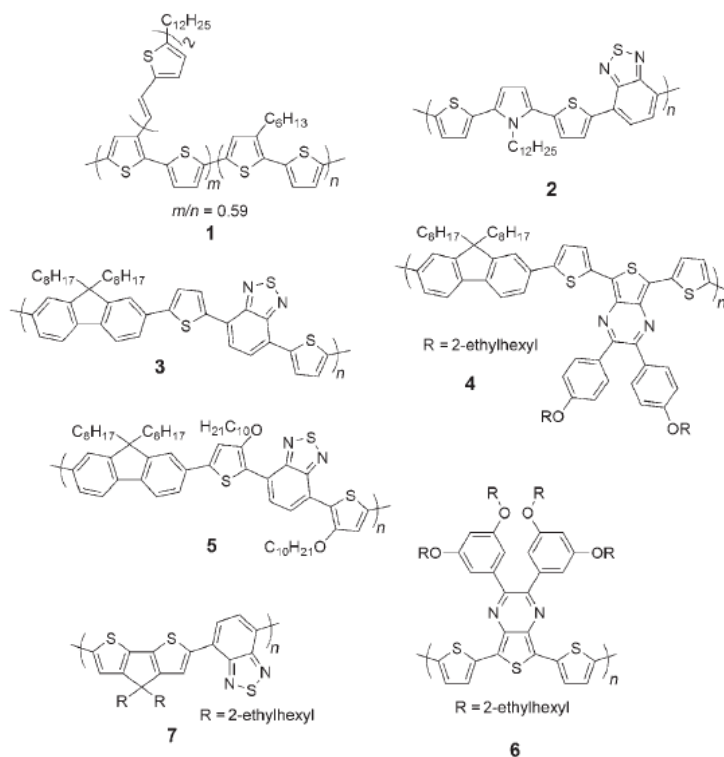


Figure 27: Several polymers employed in prototypical solar cells “Ad. from [34]”.

2 EXPERIMENTAL

2.1 Materials and Methods

All the solvents and reagents were analar-grade and were used without further purification, as provided by Sigma–Aldrich, Lancaster, Acros, or Carlo Erba. All the compounds synthesized were analyzed by chemico-physically characterizations using the techniques following:

2.1.1 Proton Resonance Magnetic Nuclear (^1H NMR)

^1H NMR characterizations were performed with ^1H NMR spectroscopy with a Varian VXR 200 MHz, Bruker Drx 400 MHz and Varian Inova 500 MHz spectrometers. ^1H NMR chemical shifts are reported as δ (ppm) compared to the solvent (CHCl_3 , $\delta = 7.26$; 1,1,2,2-tetrachloroethane, $\delta = 6.0$). The following abbreviations are used in describing the NMR multiplicities: s, singlet; d, doublet; t, triplet; and m, multiplet.

2.1.2 Optical Microscopy

Optical observations were carried out with a Zeiss Axioscope polarizing microscope equipped with a Mettler FP90 hot stage.

2.1.3 Differential Scanning Calorimetry

Phase-transition temperatures and enthalpies were measured with a PerkinElmer Pyris differential scanning calorimeter at $10\text{ }^\circ\text{C}/\text{min}$ scanning rate under a nitrogen flow. Instrument calibration was performed with a Indium sample with 99.99% of purity.

2.1.4 UV-Vis Spectroscopy

UV-Vis absorption spectra were recorded at room temperature with a Jasco V-560 spectrophotometer.

2.1.5 Photoluminescence Spectroscopy (PL)

PL emission spectra were recorded at room temperature with a Jasco FP-750 spectrofluorometer.

2.1.6 Thermogravimetric Analysis (TGA)

Thermogravimetric analyses were performed with a TA Instruments SDT2960 simultaneous DSC-TGA apparatus under both nitrogen and air flow.

2.1.7 Spin Coating

Polymeric films were obtained from organic solvents (chloroform or 1,2-dichlorobenzene solutions (10 mg/ml or 5 mg/ml), via spin coating, with a P6700 SCS spin coater.

2.1.8 Mass Spectrometry

Mass spectra were recorded on a MALDI TOF DE-PRO apparatus on 2,5-dihydroxybenzoic acid (DHB) matrix.

2.1.9 Single Crystal X-Ray Crystallography

Data collection was performed in flowing N_2 at -100°C on a Bruker-Nonius Kappa CCD diffractometer (MoK α radiation, CCD rotation images, thick slices, φ scans + ω scans to fill the asymmetric unit). Cell parameters were determined from 122 reflections in the range $3.63^\circ \leq \theta \leq 20.34^\circ$.

Semiempirical absorption corrections (multi-scan SADABS) [37] were applied. The structure was solved by direct methods (SIR 97 package) [38] and refined by the full matrix least-squares method (SHELXL program of SHELX97 package) [39] on F^2 against all independent measured reflections, using anisotropic thermal parameters for all non-hydrogen atoms. H atoms were placed in calculated positions with U_{eq} equal to those of the carrier atom and refined by the riding method.

2.2 Monomers Synthesis

Molecular structure monomers are reported in Figure 28:

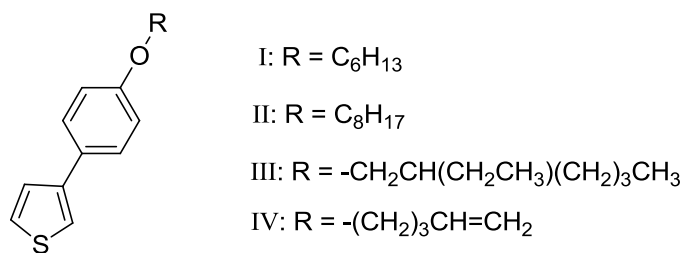


Figure 28: Molecular structure of the monomers.

2.2.1 Synthesis Monomer I

✓ *Synthesis 1-bromo-4-(hexyloxy)benzene*

4-bromophenol (115.6 mmol) and 1-bromoesane (135.6 mmol) in the presence of K_2CO_3 (180.0 mmol) were stirred and refluxed in 67 ml of *N,N*-dimethylformamide (DMF) for 6 h. The reaction mixture was cooled and filtered to eliminate K_2CO_3 not reacted, and the solution was diluted with water and extracted with hexane. The total collected hexane layers were dried over Na_2SO_4 , and evaporated. The crude product was purified by distillation under vacuum.

Yield: 88%

1H NMR (200 MHz, $CDCl_3$, δ ppm): 0.89 (t, 3H, 6Hz), 1.36 (m, 6H), 1.74 (m, 2H), 3.87 (t, 2H, $J=6$ Hz), 6.74 (d, 2H, $J=9$ Hz), 7.32 (d, 2H, $J=9$ Hz).

✓ *Synthesis 3-(4-hexyloxyphenyl)thiophene*

Under nitrogen flux, magnesium (120.0 mmol) and iodine (0.48 mmol) were dissolved in 100 ml of anhydrous tetrahydrofuran (THF) and stirred at $100^\circ C$ for 20 min (up to color reaction mixture change from red to yellow). After the reaction mixture was left to cool at room temperature and 1-bromo-(4-hexyloxy)benzene (99.0 mmol) was added drop wise. During addition operation, reaction system must be cooled by ice bath to keep temperature controlled. Reaction system was stirred at room temperature for 20 min.

Aside under nitrogen flux, 3-bromothiophene (99.0 mmol) and (1,3-bis[diphenylphosphino]propane)dichloronickel(II) $[Ni(dppp)Cl_2]$ (2.0 mmol) were dissolved in 80 ml of anhydrous THF. Reaction mixture containing Grignard react was

added drop wise (without adding residual magnesium). Reaction system was stirred at room temperature in nitrogen atmosphere for 12 h. Reaction mixture was dispersed in 600 ml of water, the precipitate was collected by filtration and recrystallized from methanol. After the residue was dissolved in 100 ml of chloroform, treated with active carbon and filtrated. Residue was recrystallized from hexane.

Yield: 62%, mp: 101°C.

^1H NMR (200 MHz, CDCl_3 , δ ppm): 0.85 (t, 3H), 1.35 (m, 6H), 1.69 (t, 2H), 3.87 (t, 2H), 6.84 (d, 2H, $J=8$ Hz), 7.28 (m, 3H), 7.39 (d, 2H).

Similar synthesis method was used to prepare both Monomer **II** and Monomer **III**.

2.2.2 Synthesis Monomer IV

✓ *Synthesis 3-(4-methoxyphenyl)thiophene*

Under nitrogen flux, magnesium (221.0 mmol) and iodine (0.922 mmol) were dissolved in 190 ml of anhydrous tetrahydrofuran (THF) and stirred at 100°C for 20 min (up to color reaction mixture change from red to yellow). After the reaction mixture was left to cool at room temperature and 4-bromoanisole (184.0 mmol) was added drop wise. During addition operation, reaction system must be cooled by ice bath to keep temperature controlled. Reaction system was stirred at room temperature for 20 min.

Aside under nitrogen flux, 3-bromothiophene (184.0 mmol) and (1,3-bis[diphenylphosphino]propane)dichloronickel(II) $[\text{Ni}(\text{dppp})\text{Cl}_2]$ (2.02 mmol) were

dissolved in 100 ml of anhydrous THF. Reaction mixture containing Grignard react was added drop wise (without adding residual magnesium). Reaction system was stirred at room temperature in nitrogen atmosphere for 12 h. Reaction mixture was dispersed in 1 l of water, the precipitate was collected by filtration and recrystallized from methanol and after heptane.

Yield: 66%, mp: 127°C.

^1H NMR (200 MHz, CDCl_3 , δ ppm): 3.80 (s, 3H), 6.85 (d, 2H, $J=8\text{Hz}$), 7.30 (m, 3H), 7.44 (d, 2H, $J=6\text{ Hz}$).

✓ *Synthesis 3-(4-hydroxyphenyl)thiophene*

Under nitrogen flux, 3-(4-methoxyphenyl)thiophene (63.07 mmol) was treated with pyridine chloride (415.4 mmol) at high temperature up to completely system fusion, in stirring for 30 min. After the reaction mixture was left to cool at room temperature and dispersed in 300 ml of water. The reaction mixture was boiled and left to cool at room temperature. The precipitate was filtered and treated with boiling heptane collected by filtration and recrystallized from ethanol-water.

Yield: 78%, mp: 187°C.

^1H NMR (200 MHz, CDCl_3 , δ ppm): 6.77 (d, 2H, $J=8\text{ Hz}$), 7.93 (m, 5H).

✓ *Synthesis 3-(4-penteneoxyphenyl)thiophene*

3-(4-hydroxyphenyl)thiophene (45.2 mmol) and 5-bromo-1-pentene (54.2 mmol) in the presence of K_2CO_3 (80.0 mmol) were stirred and refluxed in 16 ml of DMF for 6 h. .

Reaction mixture was dispersed in 300 ml of water, the precipitate was collected by filtration and recrystallized from methanol. After the residue was dissolved in 100 ml of chloroform, treated with active carbon and filtrated. Residue was recrystallized from hexane.

Yield: 45%, mp: 203°C.

^1H NMR (200 MHz, CDCl_3 , δ ppm): 1.9 (m, 1H), 2.22 (q, 2H), 4.00 (t, 2H, $J=6$ Hz), 5.06 (m, 2H), 5.87 (m, 1H), 6.96 (d, 2H, $J=9$ Hz), 7.34 (s, 2H), 7.52 (d, 2H, $J=9$ Hz).

2.3 Synthesis Cu(II) Complexes

Molecular structure Cu(II) Complexes are reported in Figure 29

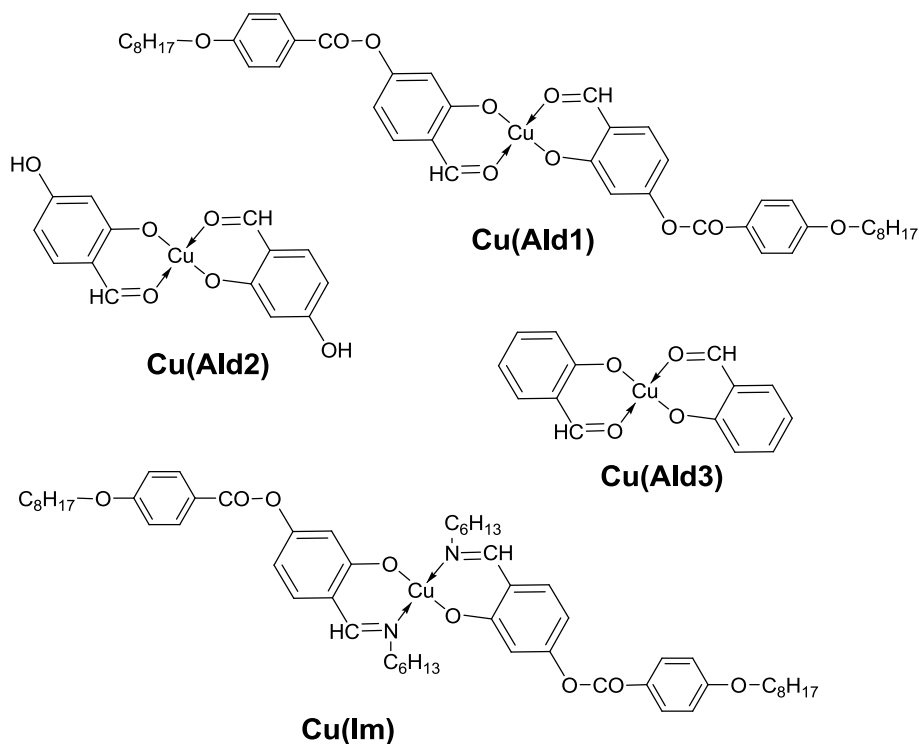


Figure 29: Molecular structure Cu(II) complexes.

2.3.1 Synthesis Cu(Ald1)

Under nitrogen flux, 2,4-dihydroxybenzaldehyde (72.0 mmol), 4-(octyloxy)benzoic acid, pyrrolidine pyridine (4.5 mmol) were dissolved in 130 ml of anhydrous THF. Aside under nitrogen flux, *N,N'*-dicyclohexylcarbodiimide (DCC) (60.0 mmol) was dissolved in 30 ml of anhydrous THF and this solution was added to reaction system previously prepared. Reaction mixture was stirred at room temperature in nitrogen atmosphere for 3 h. Reaction system was filtered to eliminate urea byproduct. Aside, copper acetate (65.0 mmol) was dissolved in 400 ml of boiling ethanol; sodium acetate (120 mmol) was dissolved in 50 ml of water; these two solution was added to THF solution previously prepared and a green precipitate was observed. To increase solid precipitation, 100 ml of water were added to the reaction system. The precipitate was collected by filtration and washed with ethanol.

Yield: 40%

TGA: calcd for (C₄₄H₅₀CuO₁₀): 9.7%. Found: 11.4%.

Similar synthesis method was used to prepare both **Cu(Ald2)** and **Cu(Ald3)**.

2.3.2 Synthesis Cu(Im)

Under nitrogen flux, 2,4-dihydroxybenzaldehyde (72.0 mmol), 4-octiloxibenzoic acid, pyrrolidine pyridine (4.5 mmol) were dissolved in 130 ml of anhydrous THF. Aside under nitrogen flux, *N,N'*-dicyclohexylcarbodiimide (DCC) (60.0 mmol) was dissolved in 30 ml of anhydrous THF and this solution was added to reaction system previously

prepared. Reaction mixture was stirred at room temperature in nitrogen atmosphere for 3 h. Reaction system was filtered to eliminate urea derivative. Aside, copper acetate (65.0 mmol) was dissolved in 400 ml of boiling ethanol; sodium acetate (120 mmol) was dissolved in 50 ml of water; these two solution was added to THF solution previously prepared and a green precipitate was observed. To increase solid precipitation, 100 ml of water were added to the reaction system. The precipitate was collected by filtration and washed with ethanol. Such precipitate and hexylamine (70.2 mmol) were refluxed in 30 ml of chloroform for 10 min. To increase solid precipitation, 40 ml of ethanol were added and the mixture system was cooled by ice bath. The resultant precipitate was collected by filtration.

Yield: 40%

TGA: calcd for (C₅₆H₇₆CuN₂O₈): 8.1%. Found: 9.1%.

2.4 Synthesis Polythiophenes

Molecular structures of polythiophenes are reported in Figure 30

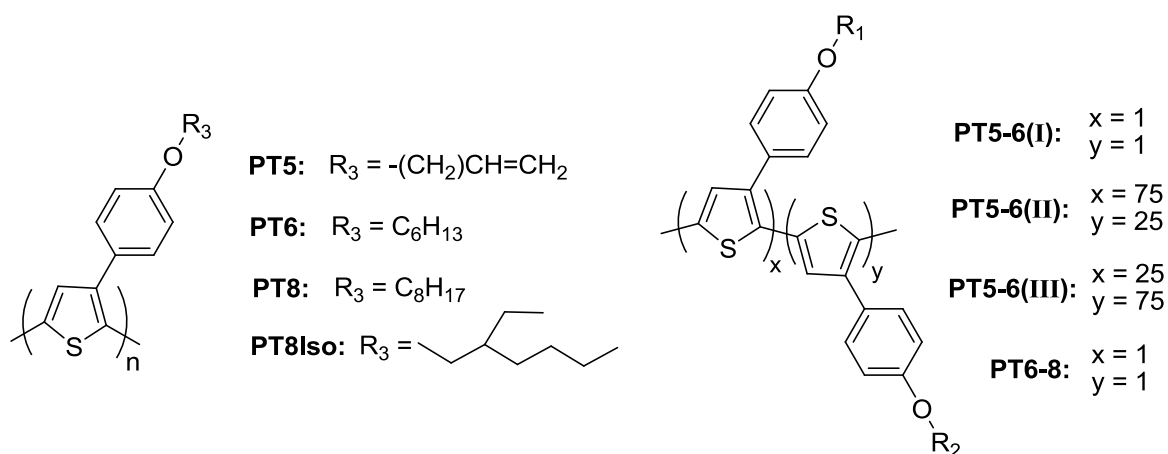


Figure 30: Molecular structures of polythiophenes.

2.4.1 Synthesis PT8-VO(acac)₂

In a two-necked, round-bottom flask (1 l), a vacuum–oxygen cycle was performed three times. Under a slight oxygen flow, VO(acac)₂ (309.2 mmol), anhydrous 1,2-dichloroethane (1.2 ml), trifluoroacetic anhydride (1.2 ml), and trifluoromethanesulfonic acid (TFMSA; 5 μl) were introduced into the flask, and the resulting mixture was stirred at room temperature for 30 min. The monomer II (4.13 mmol), trifluoroacetic anhydride (0.5 ml), and 1,2-dichloroethane (6.5 ml) were then added. The obtained mixture was stirred under an oxygen atmosphere (pressure = 1.0 atm) for 17 h at room temperature. The resulting polymer was recovered by precipitation from methanol (250 ml) containing HCl (25 ml, 37% w/w). The crude product was extracted with acetone by a Soxhlet-extraction apparatus.

Yield: 40%

¹H NMR (500 MHz, 1,1,2,2-tetrachloroethane-d₂, δ ppm): 0.89 (m, 3H), 1.31 (m, 10H), 1.78 (m, 2H), 3.96 (m, 2H), 6.89 (m, 3H), 7.28 (d, 2H, J = 8 Hz).

Similar synthesis method was used to prepare **PT5**, **PT6**, **PT5-6(I)**, **PT5-6(II)**, **PT5-6(III)** using VO(acac)₂ as catalyst.

2.4.2 Synthesis PT8-Cu(Ald1)

In a two-necked, round-bottom flask (1 l), a vacuum–oxygen cycle was performed three times. Under a slight oxygen flow, Cu(Ald1) (260.0 mmol), 1,2-dichlorobenzene (3.5 ml), trifluoroacetic anhydride (2 ml), and trifluoromethanesulfonic acid (TFMSA; 13 μl)

were introduced into the flask, and the resulting mixture was stirred at room temperature for 10 min. The monomer II (3.47 mmol), trifluoroacetic anhydride (0.8 ml), and 1,2-dichlorobenzene (3 ml) were then added. The obtained mixture was stirred under an oxygen atmosphere (pressure = 1.0 atm) for 48 h at 80°C. The resulting polymer was recovered by precipitation from methanol (150 ml) containing HCl (15 ml, 37% w/w). The crude product was extracted with acetone by a Soxhlet-extraction apparatus.

Yield: 30%

¹H NMR (500 MHz, 1,1,2,2-tetrachloroethane-d₂, δ ppm): 0.90 (m, 3H), 1.32 (m, 10H), 1.80 (m, 2H), 3.97 (m, 2H), 6.90 (m, 3H), 7.29 (d, 2H, J = 10 Hz).

Similar synthesis method was used to prepare **PT8-Cu(Ald2)** and **PT8-Cu(Ald3)**. Moreover, the same method was employed to synthesize **PT6-8** and **PT8-Iso** using Cu(Ald1) as catalyst.

2.4.3 PT8-Cu(Im)

In a two-necked, round-bottom flask (1 l), a vacuum–oxygen cycle was performed three times. Under a slight oxygen flow, Cu(Im) (260.0 mmol), 1,2-dichlorobenzene (1 ml), trifluoroacetic anhydride (2 ml), and trifluoromethanesulfonic acid (TFMSA; 4.2 μl) were introduced into the flask, and the resulting mixture was stirred at room temperature for 10 min. The monomer II (3.47 mmol), trifluoroacetic anhydride (0.8 ml), and 1,2-dichlorobenzene (5.5 ml) were then added. The obtained mixture was stirred under an oxygen atmosphere (pressure = 1.0 atm) for 96 h at 80°C. The resulting polymer was recovered by precipitation from methanol (150 ml) containing HCl (15 ml, 37% w/w). The crude product was extracted with acetone by a Soxhlet-extraction apparatus.

Yield: 23%

^1H NMR (500 MHz, 1,1,2,2-tetrachloroethane- d_2 , δ ppm): 0.90 (t, 3H, $J = 0.90$), 1.31 (m, 10H), 1.77 (m, 2H), 3.99 (m, 2H), 6.90 (m, 3H), 7.29 (d, 2H, $J = 10$ Hz).

2.5 Perylene-3,4,9,10-tetracarboxylic acid diimide (PDI) derivatives synthesis

Molecular structure of PDI derivatives are reported in Figure 31

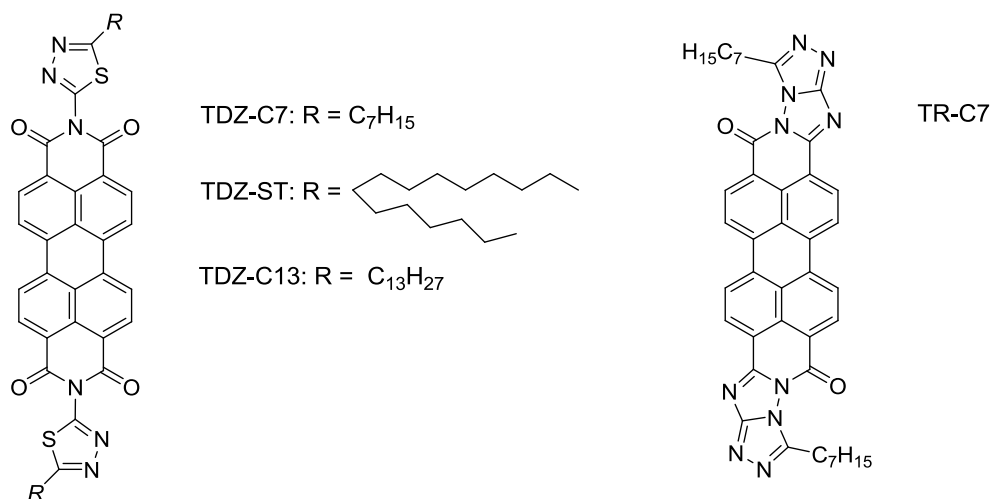


Figure 31: Molecular structures of PDI derivatives.

2.5.1 Synthesis TDZ-C7

✓ Synthesis 5-heptyl-1,3,4-thiadiazol-2-amine

Caprylic acid (62.4 mmol) and thiosemicarbazide (77.9 mmol) were dissolved with POCl_3 (21 ml) and stirred at 100°C for 1 h. The reaction mixture was cooled, diluted with 94 ml of water and refluxed for 4 h. The reaction system was basified using an aqueous solution of

sodium hydroxide (1 M) to pH 8 at room temperature. The precipitate was collected by filtration and recrystallized from ethanol-water to afford product.

Yield 50%, mp 190-192°C.

^1H NMR (200 MHz, CDCl_3 , δ ppm): 0.86 (m, 3H), 1.27 (m, 8H), 1.70, (m, 2H), 2.88 (m, 2H), 5.42 (s, 2H).

✓ *Synthesis TDZ-C7*

Perylene-3,4,9,10-tetracarboxylic dianhydride (PTCDA) (2.56 mmol), 5-heptyl-1,3,4-thiadiazol-2-amine (6.0 mmol), zinc chloride (1.18 mmol) with imidazole (3 g) were heated under N_2 at 180°C for 4 h. The reaction mixture was cooled, an aqueous solution of HCl 12 M (20 ml) was added and the reaction system reacted under N_2 for 2 h at 150°C. The reaction mixture was dispersed in 200 ml of water and basified using an aqueous solution of sodium hydroxide (1 M) to pH 7 at room temperature. The precipitate was collected by filtration and washed by a mixture composed both by aqueous solution with HCl 10% weight (200 ml) and methanol (50 ml). The solid was recovered by filtration and washed by boiling ethanol. The precipitate was collected by filtration and extracted with chloroform by a Soxhlet-extraction apparatus. The chloroform solution was reduced, the product recovered by precipitation in methanol and successive filtration.

Yield 45 %.

Elemental Analysis: calcd for ($\text{C}_{42}\text{H}_{38}\text{N}_6\text{O}_4\text{S}_2$): C 66.82%, H 5.07%, N 11.13%, S 8.49%.

Found: C 66.61%, H 4.93%, N 10.76%, S 8.34%.

M (mass spectrum), 756.13 ($M + H^+$), required for ($C_{42}H_{38}N_6O_4S_2$) 754.92.

1H NMR (400 MHz, $CDCl_3$, δ ppm): 8.81 (d, $J = 8$ Hz, 4H), 8.76 (d, $J = 8$ Hz, 4H), 3.25 (t, $J = 3.25$ Hz, 4H), 1.95 (m, 4H), 1.43 (m, 16H), 0.93 (t, $J = 0.93$, 6H).

Similar synthesis method was used to prepare **TDZ-C13**.

Regarding the synthesis method of **TDZ-ST**, the purification step differs from TDZ-C7 (see 2.5.1 Paragraph): the reaction mixture was diluted with water and extracted with chloroform. The total collected chloroform layers were extracted with water at pH 8. The total collected chloroform layers were dried over Na_2SO_4 and evaporated.

2.5.2 Synthesis TR-C7

✓ *Synthesis 5-heptyl-1,2,4-triazole-3,4-diamine*

Caprylic acid (21.7 mmol) and diaminoguanidine hydrochloride (27.8 mmol) were dissolved with polyphosphoric acid (PPA) (100 g) and stirred at $150^\circ C$ for 12 h. The reaction mixture was cooled, diluted with 250 ml of water and basified using an aqueous solution of sodium hydroxide (1 M) to pH 8 at room temperature. The precipitate was collected by filtration and recrystallized from ethanol-water to afford product.

Yield:30%, mp: $200^\circ C$.

1H NMR (300 MHz, $DMSO-d_6$, δ ppm): 0.84 (t, 3H), 1.25 (m, 8H), 1.58 (m, 2H), 2.47 (t, 2H), 5.39 (s, 2H), 5.43 (s, 2H),

✓ Synthesis TR-C7

PTCDA (2.56 mmol) and 5-heptyl-1,2,4-triazole-3,4-diamine (35.5 mmol) were refluxed with pyridine and imidazole in nitrogen atmosphere for 12h. The reaction mixture was dispersed in 200 ml of water and basified using an aqueous solution of sodium hydroxide (1 M) to pH 7 at room temperature. The precipitate was collected by filtration and washed by a mixture composed both by aqueous solution with HCl 10% weight (200 ml) and methanol (50 ml). The solid was recovered by filtration and washed by boiling ethanol. The precipitate was collected by filtration. After the compound was dissolved in 100g of PPA and stirred at 150°C for 12 h. The reaction mixture was cooled, diluted with 100 ml of basified using an aqueous solution of sodium bicarbonate (1 M) to pH 8 at room temperature. The precipitate was collected by filtration and recrystallized from DMF.

Yield: 40%.

M (mass spectrum), 715.02 (M + H⁺), 738.01 (M + Na⁺), 753.04 (M + K⁺) required for (C₄₂H₃₈N₁₀O₂) 714.82.

¹H NMR (400 MHz, CDCl₃, δ ppm): 8.81 (d, *J* = 8 Hz, 4H), 8.76 (d, *J* = 8 Hz, 4H), 3.25 (t, *J* = 3.25 Hz, 4H), 1.95 (m, 4H), 1.43 (m, 16H), 0.93 (t, *J* = 0.93, 6H).

3 POLYTHIOPHENES 3-SUBSTITUTED FOR APPLICATIONS IN ELECTRONICS

3.1 Introduction

Over the past decade, polythiophenes (PTs) variously substituted in position 3, have been widely studied for their electrical and optical applications [37]. In particular, synthesis of regioregular polythiophenes have been reported aimed at improving their photonic and electronic properties. The regioregularity is given by a regular head-to-tail (HT) connection of the repetitive units along the chain; possible configurational triads HT-HT are shown in Figure 32. The regioregularity is a fundamental feature for these materials: in fact in regioregular polythiophenes, the planarity of the backbone allows a wide delocalization of the π -electron density and the organization of the macromolecular chains in a stacked structure. Both properties improve the electrical conductivity and strongly affect the spectroscopic properties. On the contrary, regioirregular sequences produce strong interactions between substituent groups in the 3-position and force the polythiophenic backbone into a nonplanar conformation, which is detrimental to the electric properties of the material. This type of structural organization supports the charge carrier transport, dominated by hopping phenomena, and determines the macroscopic conductivity. However, different preparation methodologies are described in the literature, based on metal-catalyzed cross-coupling of the thiophenic monomers: the 3-substituted thiophenic monomer is oxidized by Br_2 in the 2- and 5-positions and the dihalogenated product is then allowed to react with finely powdered electropositive metals (Rieke metals [41]) or Grignard reagents [42] and polymerized. These synthetic procedures lead to highly

regioregular polymers (>95%) obtained in good yields, but tedious multistep and expensive procedures are required.

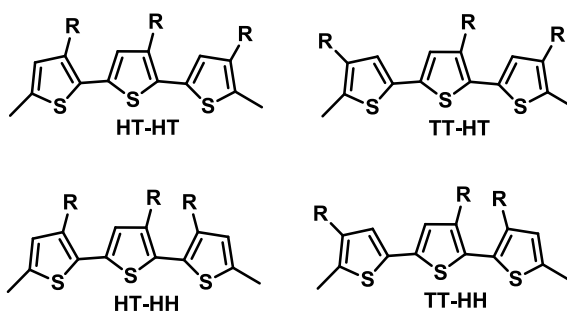


Figure 32: Different configurational triads in polythiophenes 3-substituted.

As discussed earlier, PTs represent the most important conjugated polymers utilized in a broad spectrum of applications such as OLEDs, OFETs, plastic solar cells and organic sensors. In particular, The PTs ability to change their color and electrical conductivity in response to various analytes, solvents, and environment make these polymers the ideal candidates for an all-polymer sensor. The linear-alkyl-substituted polythiophenes have been most widely studied due to their ease of synthesis. However, increasingly heteroatom-substituted PTs are being designed, synthesized and explored in order to engineer intelligent properties into the conducting polymer. The possibility of merging host-guest chemistry, biological macromolecular assembly, organic self-assembly and inorganic structural chemistry to create new conjugated polymer devices and smart materials is a rapidly expanding area. Moreover, PTs represent the most widespread organic materials utilized in the field of organic solar cells. In fact a combination of P3HT as the electron

donor and PCBM as the electron acceptor in the active layer represents the most efficient bulk heterojunction solar cell with power conversion efficiency approaching 5%. The success of the P3HT/PCBM system is largely associated with careful control and optimization of the active layer morphology.

3.2 Polythiophenes 3-Substituted for Applications in Organic Sensors

Synthesis and characterizations of polythiophenes 3-substituted by alkoxyphenilic and alkeneoxyphenilic groups are reported. Polymerizations were conducted by oxidative catalysis using vanadyl acetylacetonate ($\text{VO}(\text{acac})_2$) complex through a very simple and inexpensive procedure. The choice of this kind of polymer depends on the following factors: (i) The monomers can be synthesized on a large scale and with a high degree of purity from inexpensive reagents and with a very simple procedure. (ii) Bulky substituents on thiophene rings are useful for the selective obtainment, especially in oxidative-coupling-based methods of synthesis, of long regioregular sequences in the polymers. (iii) These polymers are very similar to alkylphenyl thiophenic polymers [43] compared to both the solubility features and electric properties. Moreover, in agreement with what has already been observed for poly(3-alkoxythiophene) systems, the greater electron donor capability of the alkoxylic chain, if compared with one of the alkylic chain, should improve the electron-donor character of the polymers. (iv) The presence of double bond in alkyl chain can lead to crosslinking reaction on film in different conditions, improving structuring and stability of polymers. The polymers were synthesized by oxidation of thiophene monomers with molecular oxygen in the presence of $\text{VO}(\text{acac})_2$ as a catalyst, trifluoroacetic anhydride (TFA) and trifluoromethanesulfonic acid (TFMSA) in 1,2-dichloroethane dry, typically for

17 h at room temperature (general reaction scheme is reported in Figure 33). This method does not require any leaving groups or removal of the byproduct in the preparation of aromatic polymers, using a procedure reported in the literature [44]. Such synthetic procedure leads to regioregular polythiophenes with over 90% HT content. Generally, thiophenes are polymerized by oxidative coupling reactions in the presence of oxidants. The accepted mechanism of this reaction is outlined in Figure 34. Firstly, a thiophene nucleus undergoes one-electron oxidation to give a radical cation. The efficiency of this step can be inferred from the ionization potential of the compound.

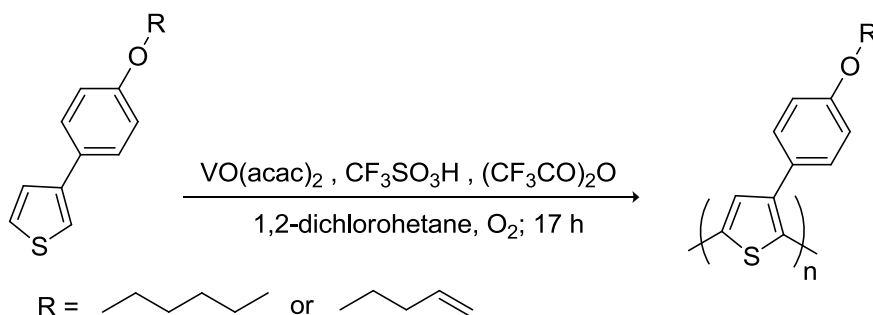


Figure 33: Synthesis scheme of polythiophenes.

Secondly, two radical cations couple yield dihydro cation dimers. This coupling reaction is more likely to occur in the position with high spin density. Thirdly, the dihydro cation dimers release two protons to form a dimerization product that undergoes further oxidation followed by proton loss to give the dimerization product. These reactions are repeated and lead to polymers.

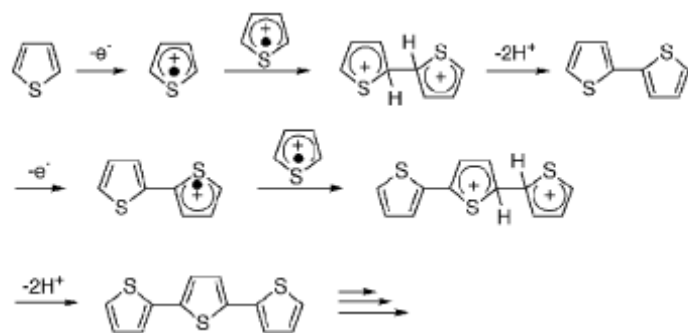


Figure 34: Mechanism of polymerization of thiophenes.

In this system, an active oxidant is a vanadium(V) species which is produced by the disproportionation of vanadium(IV) species in V(V) and V(III), as shown in Figure 35. After the V(V) species worked as an oxidant, oxidizing the thiophene nucleus, it converts to V(IV) species. Parallely, V(III) is oxidized to V(IV) by the O_2 present in the reaction environment, closing the catalytic cycle.

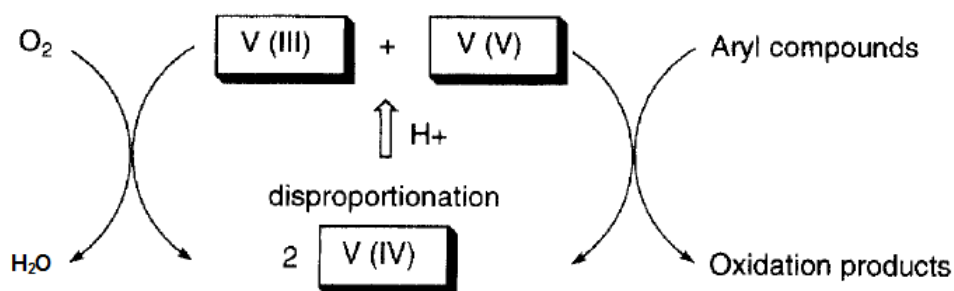


Figure 35: A catalytic cycle of the oxivanadium catalytic system.

The thiophene nucleus is oxidized by V(V) species to give a radical cation, as V(III) species react with molecular oxygen to give again V(IV) species, closing the catalytic cycle.

As mentioned earlier, we have employed the polymerization method based on oxidative catalysis using $\text{VO}(\text{acac})_2$ also to synthesize polythiophenes 3-substituted by alkeneoxyphenilic groups. The choice of this kind of substituent was motivated by the possibility of realizing cross-linking reactions on polymer films to improve the structuring, electrical conductivity and stability to the photo-oxidation reactions of the polymers.

Finally, the effects of different VOCs on the electrical properties of such materials were carefully investigated and their potential application as electrical sensors will be discussed in 3.2.3. Paragraph.

3.2.1 Synthesis Methods

Synthesis methods that we have developed to obtain the different monomers employed in polymerization reactions and the synthesis of different polythiophenes 3-substituted are discussed in this section.

✓ *Synthesis of monomer (I)*

Preliminary reaction (Figure 36) concerned the synthesis of the intermediate 1-bromo-(4-esyloxy)benzene by Williamson etherification of 4-bromophenol with 1-bromoesane, in the presence of K_2CO_3 as base in *N,N*- dimethylformamide (DMF):

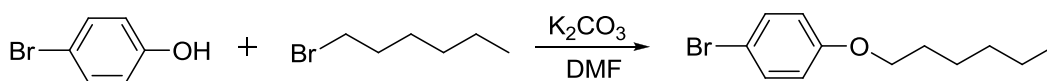


Figure 36: Synthesis of 1-bromo-(4-esiloxy)benzene by Williamson etherification.

Afterwards, magnesium with iodine in anhydrous tetrahydrofuran was activated and into this system was added 1-bromo-4-(hexyloxy)benzene. Then the monomer (I) was prepared by Grignard reaction of 4-esyloxyphenyl magnesium bromide with 3-bromothiophene in anhydrous THF, in the presence of a catalyst amount of (1,3-bis[diphenylphosphino]propane)dichloronickel(II) [Ni(dppp)Cl₂] (see Figure 37):

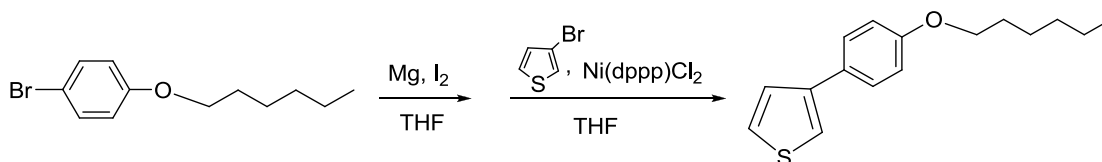


Figure 37: Synthesis of monomer (I) by Grignard reaction.

In this procedure, the Grignard reagent in situ was prepared. Similar method of synthesis was used to prepare both monomer (II) and monomer (III).

✓ *Synthesis of monomer (IV)*

The monomer (IV) was synthesized by a different strategy due to the incompatibility of the unsaturation of the alkyl chain under the conditions of Grignard reaction. In this case, the

preliminary reaction (Figure 38) concerned about the synthesis of the intermediate 3-(4-methoxyphenyl)thiophene by Grignard reaction of 4-bromoanisole with 3-bromothiophene.

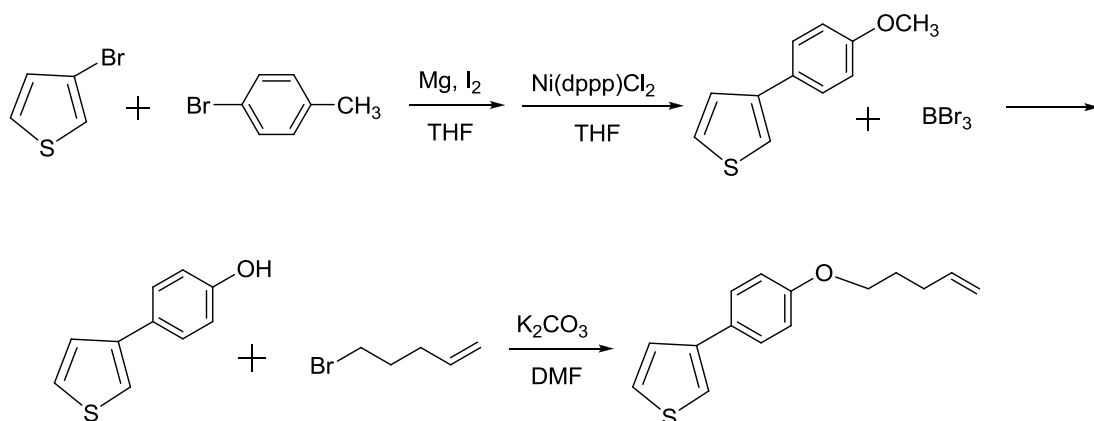


Figure 38: Scheme of synthesis of monomer (IV).

Afterwards, the intermediate 3-(4-methoxyphenyl)thiophene was undergone to hydrolysis reaction through BBr₃ to obtain 3-(4-hydroxyphenyl)thiophene. In such method, Williamson etherification was made between 3-(4-hydroxyphenyl)thiophene and 5-bromo-1-pentene.

✓ *Synthesis of the polymers*

The synthesis procedure was optimized by the variation of the experimental conditions in a wide range of experiments. The polymers were synthesized by oxidation of thiophene monomers with molecular oxygen in the presence of VO(acac)₂ as a catalyst, TFA and TFMSA in anhydrous 1,2-dichloroethane, typically for 17 h at room temperature. Different homopolymers and copolymers were synthesized, as shown in Figure 39.

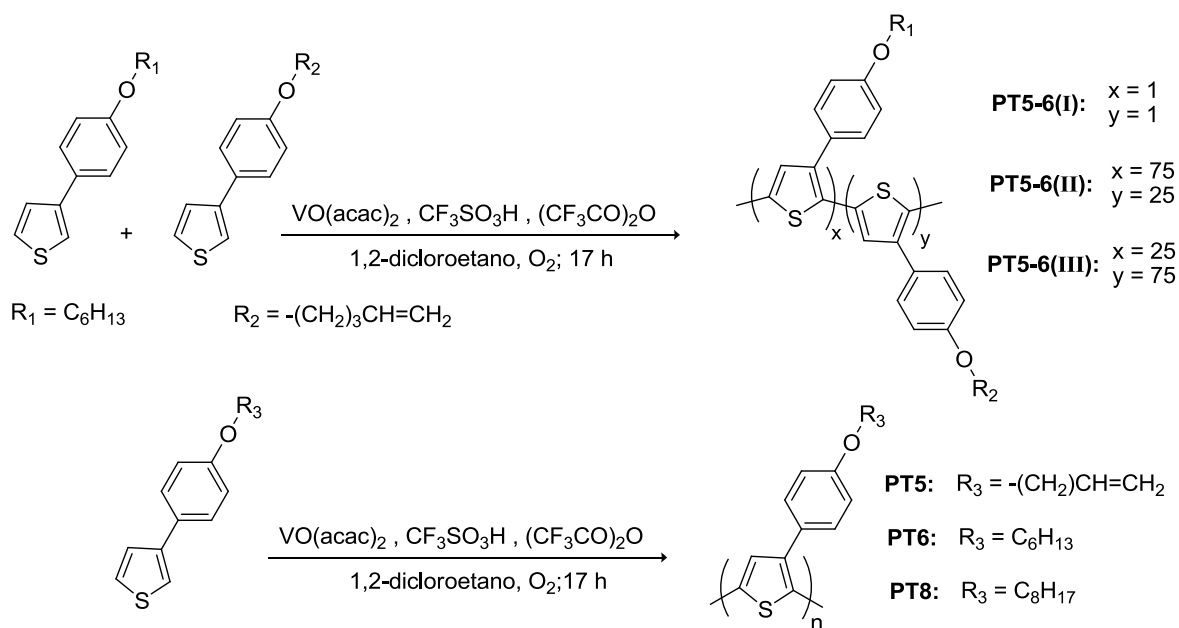


Figure 39: Scheme of synthesis of the polythiophenes.

Different typologies of copolymers were obtained through different weight ratios of the corresponded monomers, as reported in Figure 39. Several parameters influence the polymerization rate like the oxygen pressure, catalyst $[VO(acac)_2]$, and TFMSA concentration and they also strongly affect the regioregularity of the resulting polymers too. An increase in the polymerization rate always leads to a reduction of the regioregularity. The reaction time is also an important parameter. Other conditions being equal, increasing the reaction time leads to the formation of polymers containing significantly long regioirregular sequences together with equally long regioregular sequences, determining a sort of block copolymer. A possible explanation of this behavior could be suggested according to the observation of Ueda et al. [44] that, during the polymerization reaction, a regioregular polymer was mainly produced together with

significant fractions of oligomers with a regioirregular end, which is hardly reactive. Therefore, until there is monomer in the reaction system, regioregular chains should preferably grow, but once the monomers are totally reacted, terminations of regioregular chains can react only with regioirregular oligomers. If there is enough time for this process to occur, a long sequence with a poor degree of regioregularity could bind to the initial regioregular sequence, leading to a polymer showing the optical properties of both regioregular and regioirregular poly(3-substituted)thiophenes. In effect, using a time reaction of 17 h and 1 atm as oxygen pressure it is possible to obtain the polymers with good yield and high regioregularity. Afterwards, the crude product of polymerization is extracted with acetone by a Soxhlet-extraction apparatus. Such procedure allows the elimination of byproducts and regioirregular oligomers. A polymeric residual obtained is soluble in chlorinated organic solvents.

3.2.2 Characterization Methods

^1H NMR and UV-Vis analysis were employed to investigate about the structural characteristics and to obtain a qualitative evaluation of regioregularity degree of the polymers synthesized.

✓ ^1H -NMR Analysis

^1H -NMR analysis confirm the polymers structures obtained. Moreover, this method lets calculate the real amount of monomer I and IV contained in the copolymers, compared to stoichiometric amounts of monomers are allowed to react. In fact, such quantitative

evaluation was made through the comparison of methylene proton signals, bonded to oxygen atom, and proton vinylic signals. For example, in $^1\text{H-NMR}$ spectrum of PT5-6(II) (Figure 40) by areas ratio of the multiplet at $\delta=5.00$ ($\text{CH}=\text{CH}_2$) and $\delta= 3.96$ (O-CH_2), it is possible to estimate that the real percent of monomer IV is 27%, compared to stoichiometric amounts of monomer to react (25% weight).

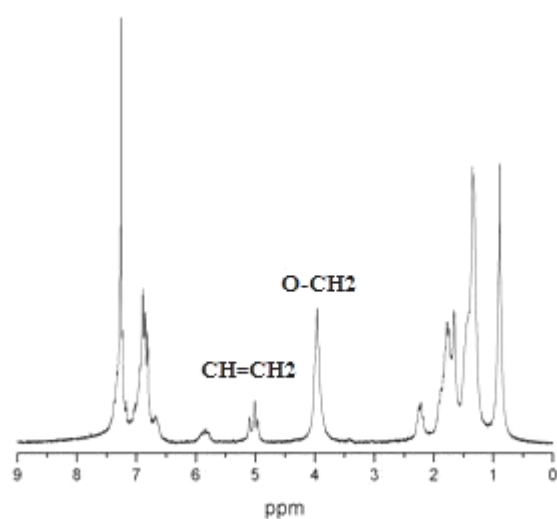


Figure 40: $^1\text{H-NMR}$ spectrum of PT5-6(II)

The related data to all the polymers are reported in Table 1.

Table 1: Quantitative evaluation of monomer I and IV contained in the copolymers compared to stoichiometric amounts of monomers are allowed to react: ^a experimental values found; ^b theoretical values.

Monomer	PT5-6(I)		PT5-6(II)		PT5-6(III)	
	(I)	44% ^a	50% ^b	28% ^a	25% ^b	73% ^a
(IV)	56% ^a	50% ^b	72% ^a	75% ^b	27% ^a	25% ^b

✓ UV-Vis Analysis

UV-Vis studies were made by polymer films obtained from chloroform solution (10 mg/ml) via spin-coating. Afterwards, the films were annealed for 15 minutes, at 150°C in nitrogen atmosphere. UV-Vis spectra can be assumed as qualitatively diagnostic of the regioregularity of poly(3-substituted)thiophenes. McCullough et al. [45] reported that a redshift of λ_{\max} could be found in regioregular poly(3-alkylthiophene)s (HT sequences) in comparison with regioirregular poly(3-alkylthiophene)s, both in solution and in films. The redshift is particularly evident for films: UV-vis spectra of HT sequences show λ_{\max} values of 550-560 nm, whereas for regioirregular poly(3-alkylthiophene)s, λ_{\max} is ~450 nm. Moreover, a vibronic structure appears in spectra of films of HT sequences with less intense secondary peaks at 590-600 and 665-700 nm.

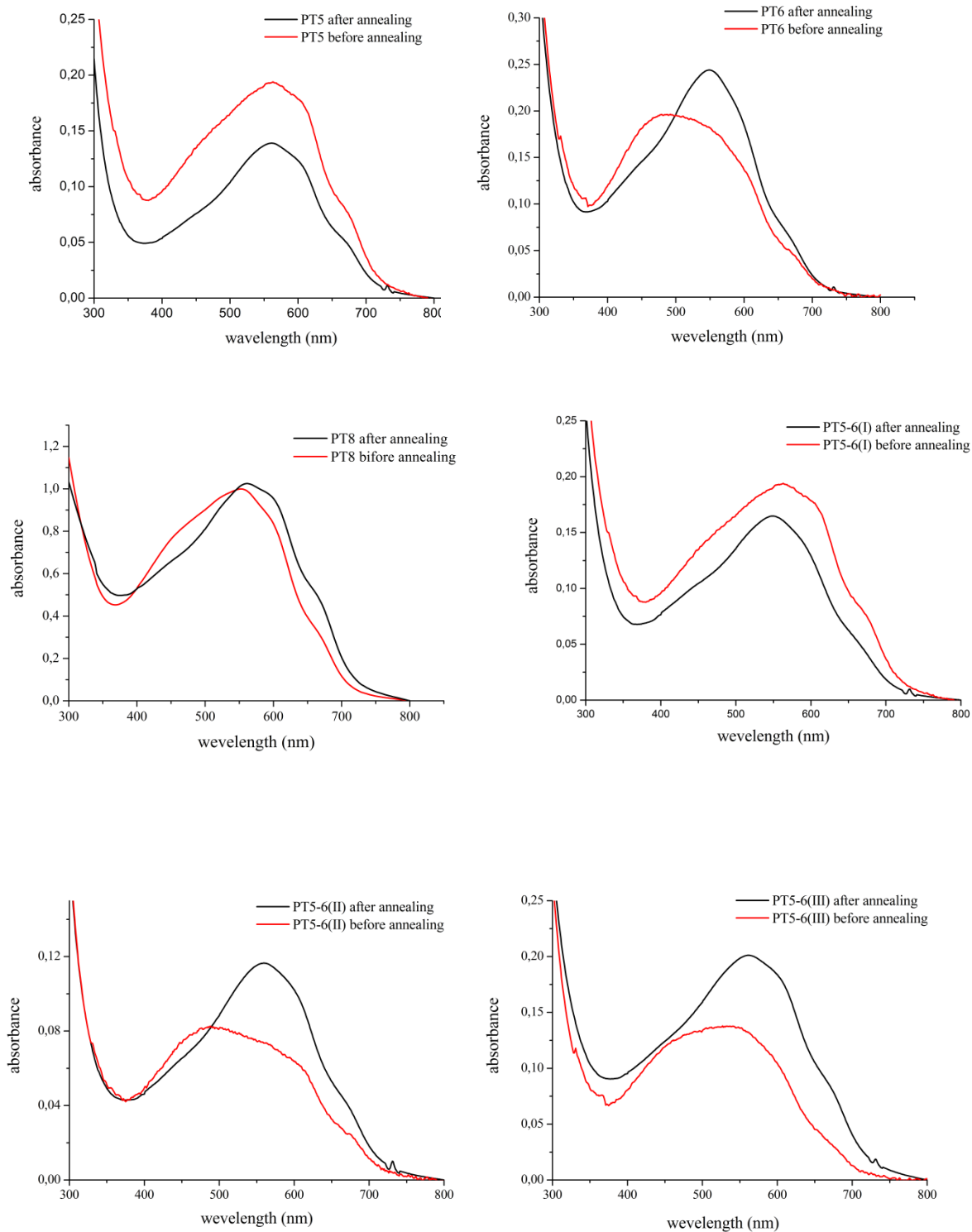


Figure 41: UV-Vis spectra by polymer films before and after annealing.

The redshift observed for regioregular polymers indicates a longer conjugation length depending on a higher degree of planarity of the backbone. UV-Vis spectra of polymer films before and after annealing are reported In Figure 41.

The spectroscopic behavior of the different polymers is very similar, thus confirming the good reproducibility of the employed polymerization method. Films prepared by spin coating show UV-vis spectra with λ_{\max} and secondary peaks typical of regioregular 3-substituted polythiophenes. In fact, after annealing (the phenomenon is fewer relevant for PT5 and PT8) polymers show a strong redshift of λ_{\max} from 488 to 562 nm and the secondary peaks both 590-600 nm and 665-700 nm (see Table 2) due to the strong electron-donor efficiency of the 4-alkoxyphenyl groups.

Table 2: Data related to redshift of λ_{\max} for polymer films before and after annealing.

λ_{\max} (nm)	PT5	PT6	PT8	PT5-6(I)	PT5-6(II)	PT5-6(III)
<i>before annealing</i>	563	492	553	549	488	541
<i>after annealing</i>	561	549	562	549	560	562

Moreover, the films of PT5 and copolymers (containing crosslinkable units) show high insolubility after annealing. This phenomenon is compatible with the occurrence of a thermally activated cross-linking reaction, in accordance to data of literature [46]. In fact, the thermal treatment on polymer film can induce a cycloaddition reaction between vinilic

groups, leading to the formation of a covalent bond between two different chains. Probably, this occurs through the formation of a cyclobutane unit, as shown in Figure 42. Therefore, the film insolubility may result by a more orderly arrangement of the chains, induced by crosslinking.

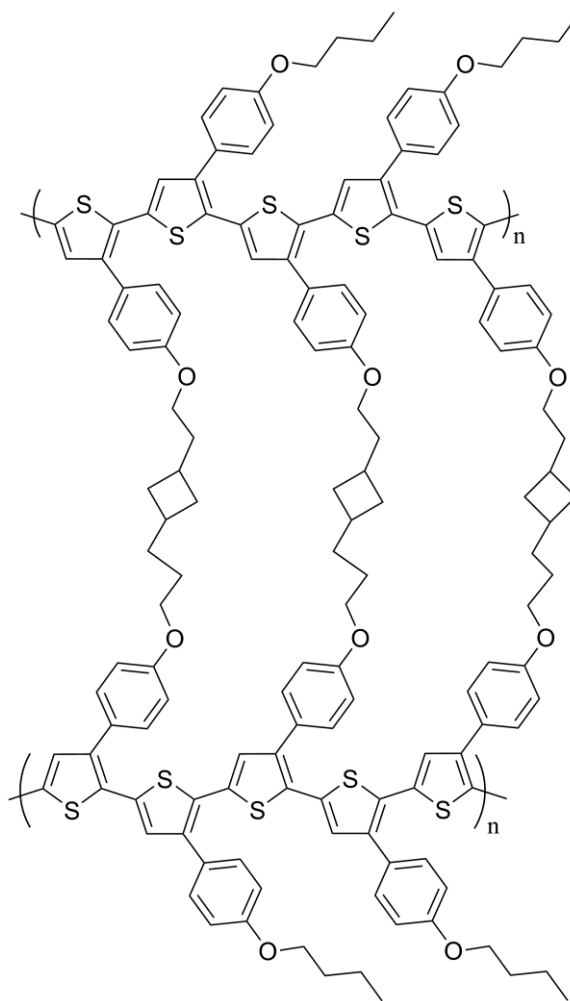


Figure 42: Supposed chemical structure consequent to crosslinking reaction.

3.2.3 Detection of VOCs Compounds Using Polythiophenes 3-Substituted

As earlier discussed, the effects of different VOCs on the electrical properties of polythiophenes synthesized were widely studied and their potential application as electrical sensors were carefully investigated.

In order to realize the sensor devices, the polymers were deposited via drop-casting onto a alumina substrate with interdigitated gold electrodes (Figure 43).

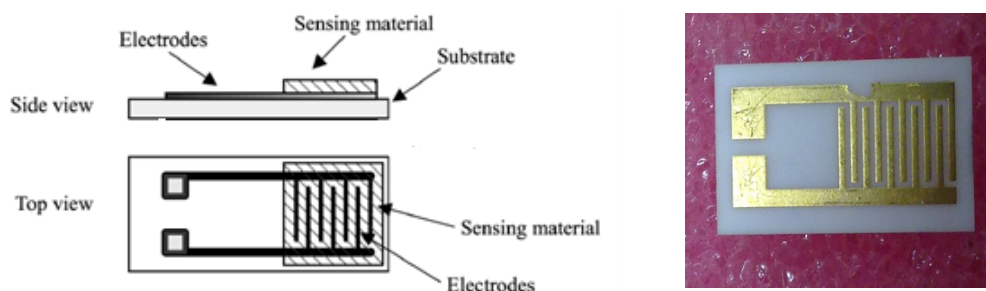


Figure 43: Structure of a chemiresistor device.

The response characteristics of the micro gas sensor films were then investigated against various test gases. The response behavior of polymer sensors was characterized by measuring the current versus time with a fixed applied voltage (0.5 V) at 20°C, in dark. The sensors were tested in a test chamber (GSCS System) in the presence of organic volatile gases in dynamic flow, carried by nitrogen. Moreover for each concentration gas it were performed three fases: baseline, where the response device is recorded in absence of analyte; step, where the response device is recorded in the presence of analyte; recovery,

where the response device is again recorded in absence of analyte, going back to initial state. Such cycle sensor device is shown in Figure 44.

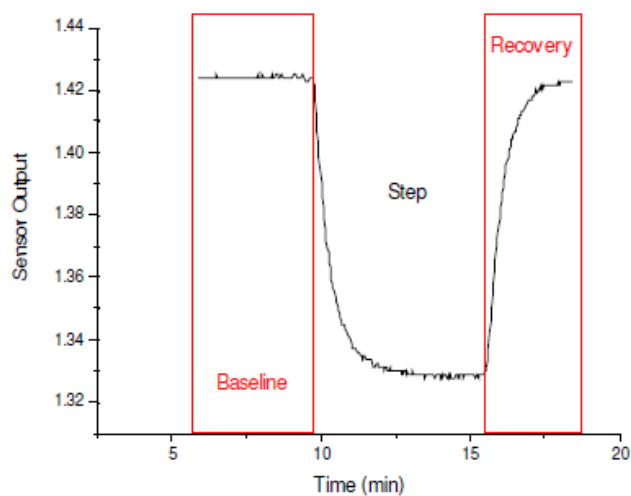


Figure 44: Cycle sensor device is subdivided in three faces: baseline, step and recovery.

The measurements were carried out in the laboratories of the research center ENEA of Portici, Italy.

In particular, the experimental results of PT8 and PT5-6(I) based device are fully discussed below.

✓ *PT8 Based Device*

PT8 solution (10 mg of polymer in 1 ml of dopant solution constituted by 2 % w/v FeCl_3 in chloroform), filtered through a 0.2 μm PTFE filter, was deposited via drop-casting onto the alumina substrate. Afterwards, the device was annealed at 150°C for 15 minutes and its

electrical behavior investigated in the presence of various VOCs. Figure 44 summarizes sensor responses of PT8 to different VOC vapors. It is evident that each VOC vapor tested resulted in a unique sensor response pattern. For all vapors it is observed a positive response, indicating that the conductivity of the materials increases in the presence of the VOCs, since the conductivity is directly proportional to current value. The sensors demonstrated a fast response to all vapors. Moreover, sensor current values returned to the initial ones after flushing the chamber for 10 min with nitrogen, showing that these changes are completely reversible with absence of hysteresis. The positive response observed to all VOCs could be related to oxygen atom into side chain. In fact, side chain containing oxygen atom has a high dipole moment. Therefore, stronger electrostatic interactions occurred when PT8 is exposed to all tested analytes. The dipole-dipole electrostatic force between polar analytes with certain dipole moments and polymer polar alkyl side chains could push the polymer molecules closer together, thus reducing hopping distances and resulting in a conductance increase.

As far as acetone is investigated as analyte, the performed tests indicated that the moisture does not influence the conductivity of PT8: the experiments run using both moist and dry acetone showed in fact the same trend. The tests carried out with ethanol and toluene featured visible tails at the base of the peaks (see Figure 45). This behavior could be related to a slower analyte desorption as compared to its absorption, allowing the penetration of the analyte into the deep layers of the film.

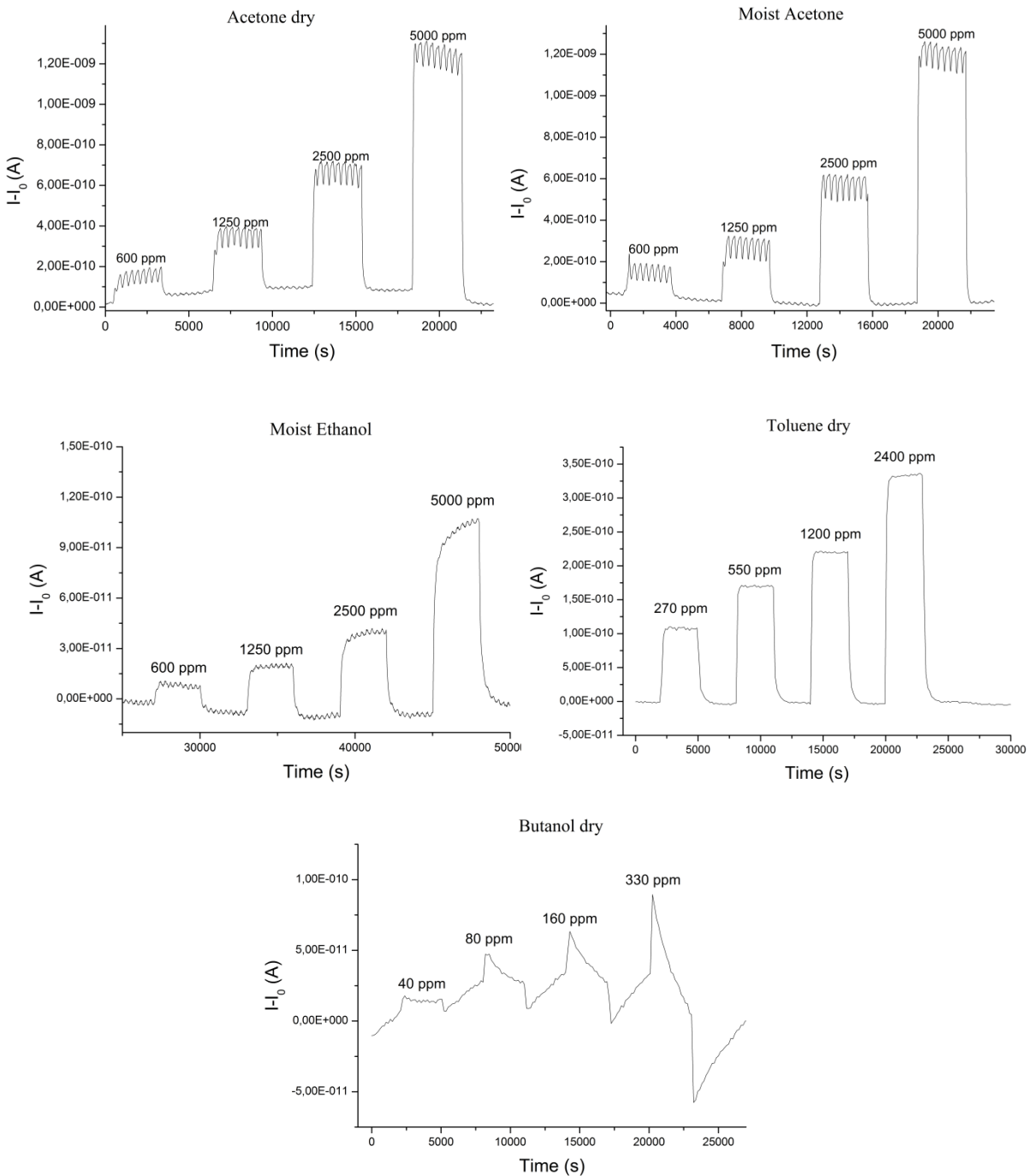


Figure 45: Sensor responses of PT8 to various VOC vapors.

Finally, the tests made with butanol dry show instead an irregular trend: in this case we can assume a fast adsorption of the analyte, that immediately cause an increase in the current intensity, followed by a desorption of the dopant agent occurs, with a consequential decrease of the current intensity. This process becomes very evident at higher concentrations (see Figure 45).

The main characteristics of the devices are reported in Table 3. It is clear that the sensibility values decrease with polarity analyte: the highest value is obtained with toluene, followed by butanol and acetone. The ethanol test contrasts this trend, probably due to moisture present during the test. The detection limit values follow the same trends; finally, the response times are very satisfactory being in all the times lower than 2 minutes.

Table 3: Characteristics of the PT8 based devices.

Analyte	Sensibility (S/ppm)	Detection Limit (ppm)	Response Time (s)
Moist Acetone	$2.3 \cdot 10^{-13}$	50	<120
Acetone dry	$2.3 \cdot 10^{-13}$	40	<120
Moist Ethanol	$2.3 \cdot 10^{-14}$	250	<120
Toluene dry	$2.5 \cdot 10^{-13}$	20	<120
Butanol dry	$7.5 \cdot 10^{-13}$	10	<120

Current intensity versus the analyte concentration is reported in Figure 46. For acetone and ethanol a linear response is observed while in the case of toluene, this behavior does not occur.

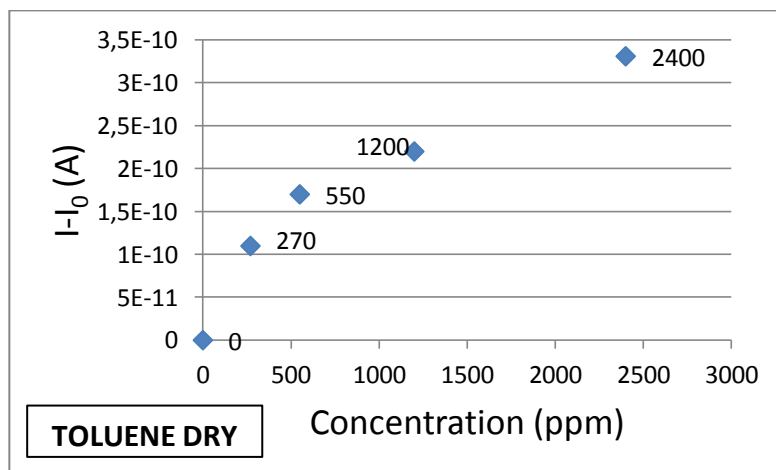
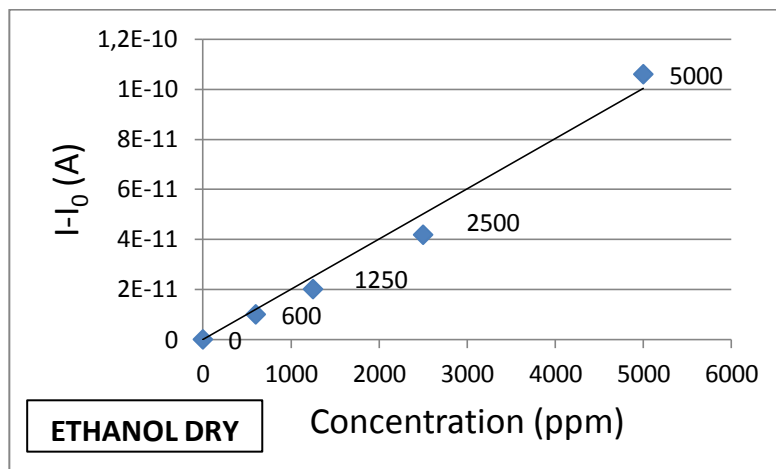
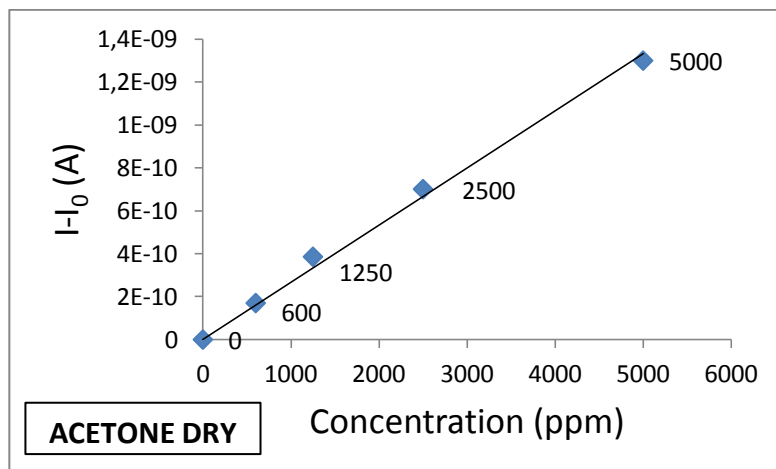


Figure 46: Concentration analytes versus variation of the current.

✓ *PT5-6(I) Based Device*

The same analysis method is used to PT5-6(I). In fact, polymer solution (10 mg of polymer in 1 ml of chloroform solution with FeCl_3 2%), filtrated through a $0.2 \mu\text{m}$ PTFE filter, was deposited via drop-casting onto the alumina substrate. Afterwards, the device was annealed at 150°C for 15 minutes and investigated against various VOCs.

Figure 47 summarizes the sensor responses of PT5-6(I) to different VOC vapors.

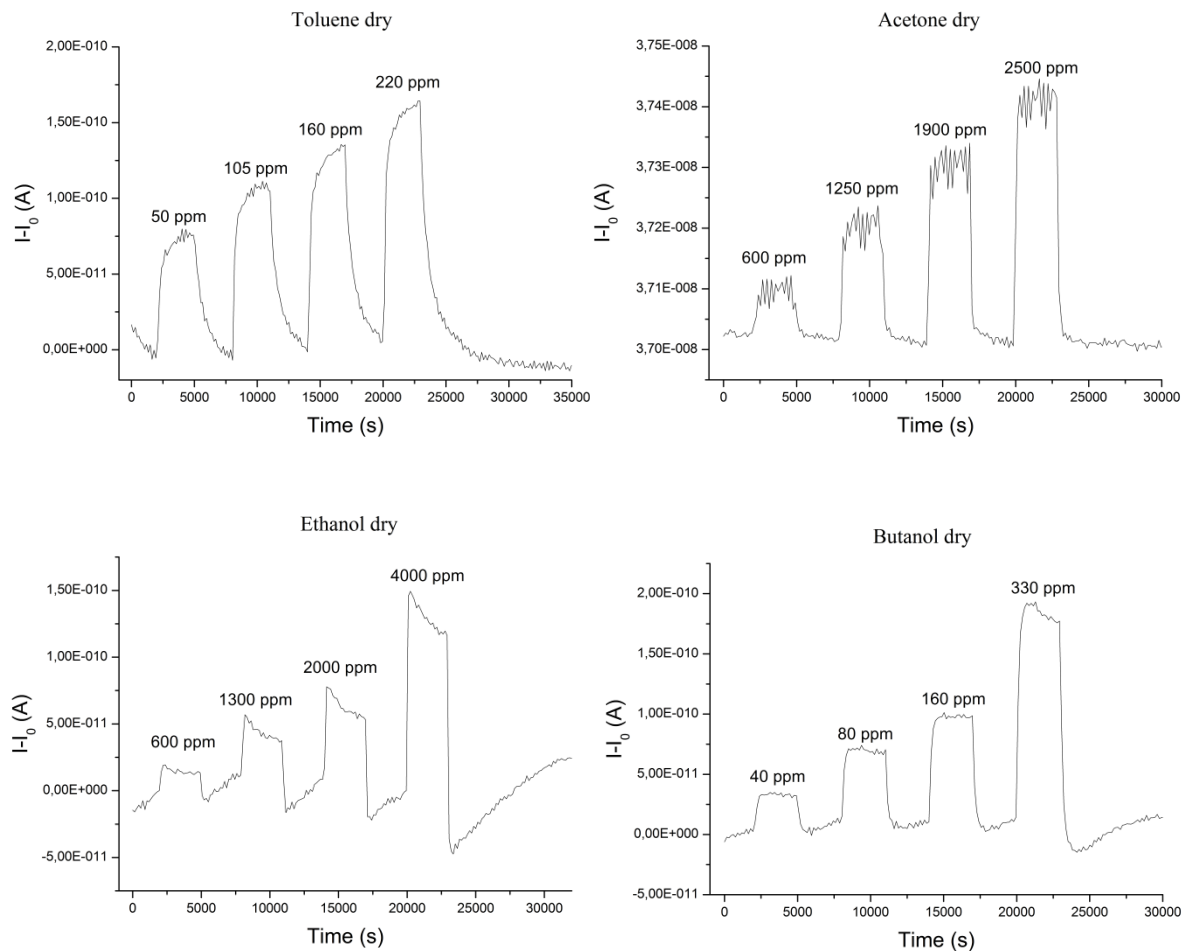


Figure 47: Sensor responses of P5-6(I) to various VOC vapors.

As already observed for PT8, also in this case we have verified that the moisture does not influence the conductivity. As far as toluene is investigated as analyte, the tests featured drift-up and visible tails at the base of the peaks. In this case we can assume that the analyte is able to enter into the deep layers of the film. This irregular trend is reflected also in graph reported in Figure 48, in which the current response is plotted versus the concentration of the analyte.

The main parameters that allow us to evaluate the device performances are quite good (see Table 4). In fact values of sensibility and noise are satisfactory, thus allowing low detection limits, as also shown in Figure 48. Response times are instead high, and this can be caused by chemical structure of polymer. Regarding acetone, the tests show that the sensibility values are very good, the noise is moderate and device reports low detection limit (see Table 4). Moreover, unlike the case of toluene, there is a linear current response of versus analyte concentration (Figure 48).

As far as ethanol is investigated as analyte, we have observed an irregular trend, that can be described by two principal events: firstly, a fast adsorption of the analyte occurs, that involves an increase of the current intensity. Secondly, the loss of the dopant agent occurs, with decreases of the current intensity. This process becomes very evident at higher concentrations (Figure 48).

Moreover the current variation versus analyte concentration is quite regular (see Table 4).

Finally, as far as butanol is employed as analyte, the tests reports a linear trend, with good sensibility values and low detection limits (see Table 4).

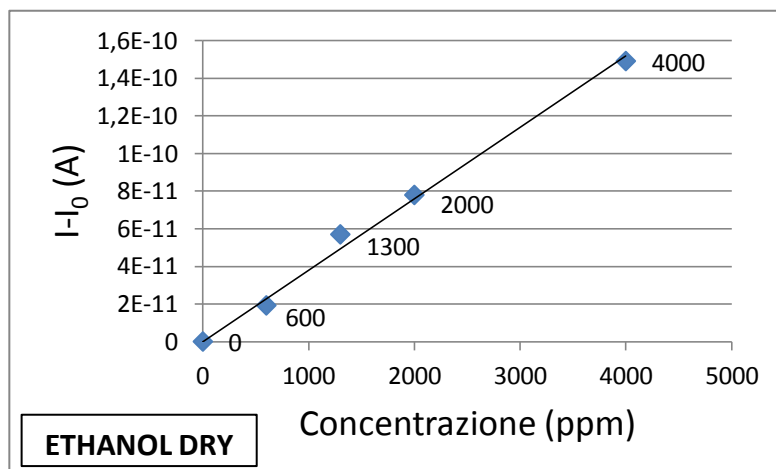
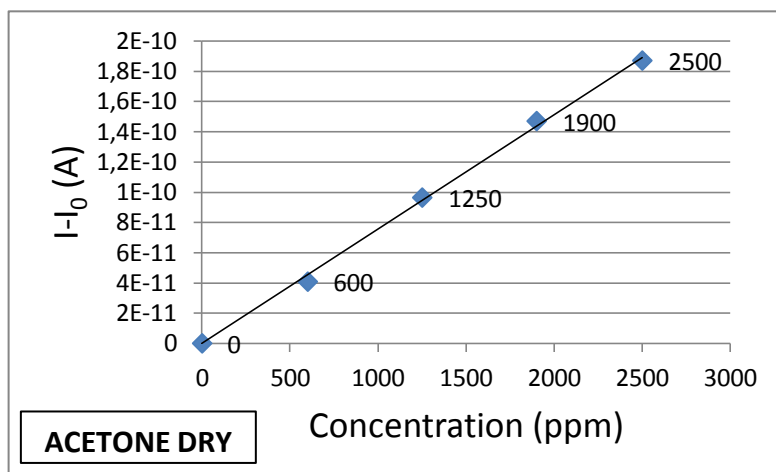
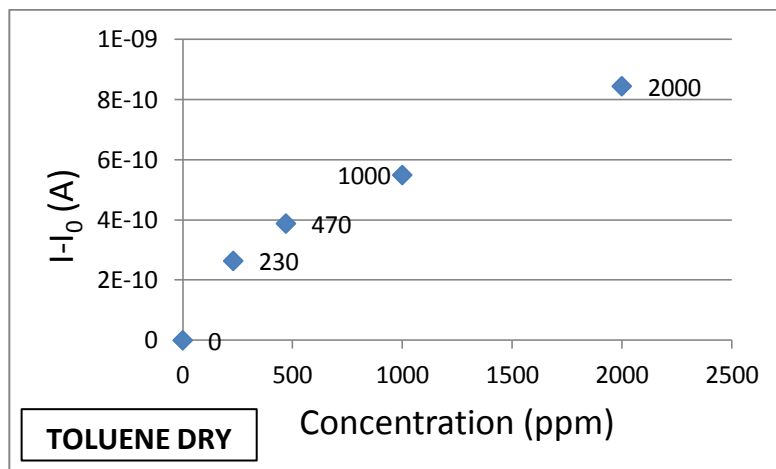


Figure 48: Concentration analytes versus variation of the current.

The main characteristics of PT5-6(I) based devices are summarized in Table 4.

Table 4: Characteristics of the PT5-6(I) based devices.

Analyte	Sensibility (S/ppm)	Detection Limit (ppm)	Response Time (s)
Acetone dry	$2.4 \cdot 10^{-13}$	100	240
Ethanol dry	$1.6 \cdot 10^{-11}$	200	298
Toluene dry	$2.33 \cdot 10^{-12}$	<1	596
Butanol dry	$1.32 \cdot 10^{-11}$	<1	297

3.3 Synthesis of Highly Regioregular Poly[3-(4-alkoxyphenyl)-thiophene]s by Oxidative Catalysis Using Copper Complexes for Application in Photovoltaics.

While the polyalkoxyphenylthiophene derivatives synthesized by means of vanadyl catalyzed oxidative coupling proved extremely useful materials in sensor applications, they did not afford good results when tested as active layers in organic solar cells or transistors. We identified the main problem in the regioregularity degree that, by using the vanadyl catalyzed oxidative coupling synthetic strategy, did not exceed 90 %. It was therefore necessary to develop a new synthetic procedure in order to obtain poly[3-(4-alkoxyphenyl)thiophene]s with regioregularity similar to that obtained by McCullough and Rieke methods in the synthesis of poly-3-alkylthiophenes.

To achieve this goal, a deep investigation of the activity of different oxidation catalysts in alkoxyphenylthiophene polymerization was carried out. At the beginning, our research was addressed towards vanadyl complexes with different ligands but the results were not satisfactory. As an example, in Figure 49 the molecular structure of one these new complexes is reported: this catalyst was tested both at room temperature and at 80°C: in the first case, polymers with regioregularity comparable to that achieved using VO(acac)₂ as catalyst were obtained, but longer reaction times were required; in the second test regioirregular polythiophenes were produced. Similar results were obtained with different ligands and therefore it was decided to investigate different metal center, possibly able to catalyze regiospecific oxidative reaction between thiophene rings. In this context, we have employed different complexes of metals as Mn(II), Fe(II), Co(II), Ni(II), Nb(II) in a wide range of conditions, but also in this case no one gave satisfactory results.

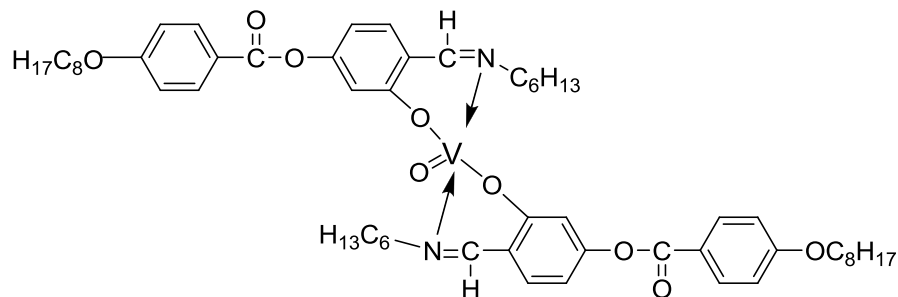


Figure 49: Vanadyl complex experimented.

We approached copper complexes, encouraged also by previous work reported in the literature about regiospecific polymerization of naphthalene systems copper catalyzed [44]. After a preliminary investigation of copper acetylacetonate catalyst, which did not afford interesting results (regardless the temperature used, regioirregular polythiophene were obtained), we finally developed a set of catalysts that, as we will described below, gave excellent results. The molecular structure of these catalyst, named Cu(Im), Cu(Ald1), Cu(Ald2), are sketched in Figure 50.

The scheme in Figure 51 summarized instead the synthetic pathway for the preparation of Cu(II) complexes. The first step shows the preparation of ligand **3** through the reaction of 2,4-dihydroxybenzaldehyde with 4-(octyloxy)benzoic acid in the presence of *N,N'*-dicyclohexylcarbodiimide (DCC) in THF. This reaction lead to a mixture of two isomers with the esterification occurring at position 2 of 2,4-dihydroxybenzaldehyde at position 2 (minority product) or at position 4 (the prevalent and desired product, ligand **3**).

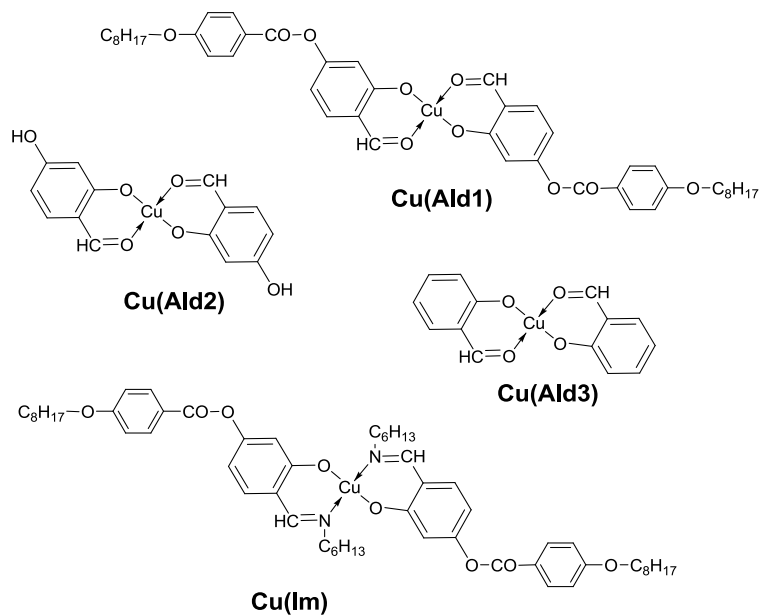


Figure 50: Molecular structure of Cu(II) catalyst.

Anyway, only the latter can react with $\text{Cu}(\text{CH}_3\text{COO})_2$ to give the correspondent complex in the successive reaction.

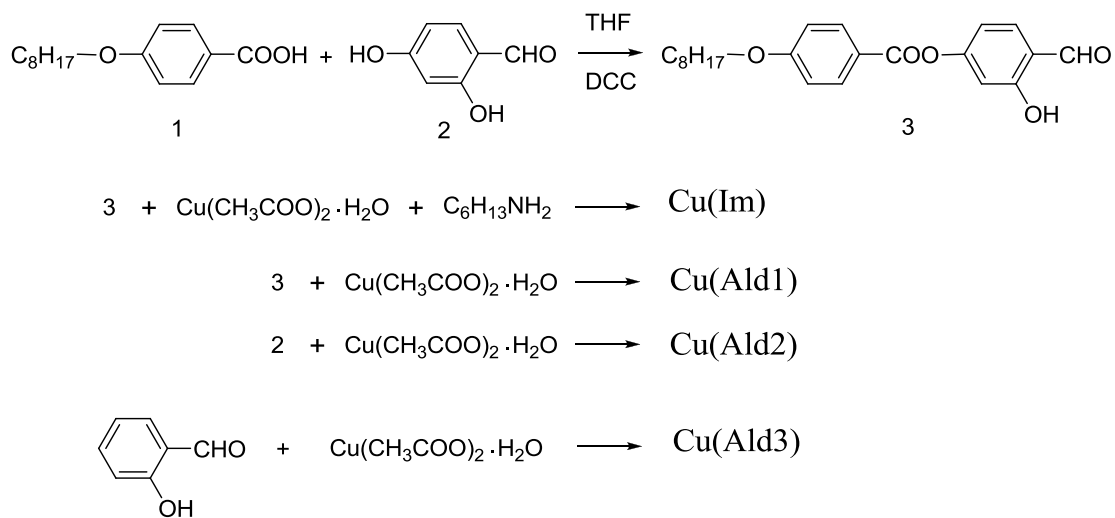


Figure 51: Synthesis Scheme of Cu(II) complexes.

The complexes Cu(Im) and Cu(Ald1) were prepared by reacting **3** with Cu(CH₃COO)₂ respectively in the presence or not of hexylamine. Cu(Ald2) and Cu(Ald3) were instead obtained by reaction of Cu(CH₃COO)₂ with 2,4-dihydroxybenzaldehyde or 2-hydroxybenzaldehyde respectively. All these reactions were carried out in boiling absolute ethanol. The chemical synthesis of copper containing complexes were performed following a procedure described in literature [48].

Thermogravimetric analysis were carried out to confirm the structures of the complexes obtained: the experiment was performed in air atmosphere in order to obtain CuO as residual product after the decomposition.

As example, the thermogravimetric analysis of Cu(Ald2) is reported in Figure 52.

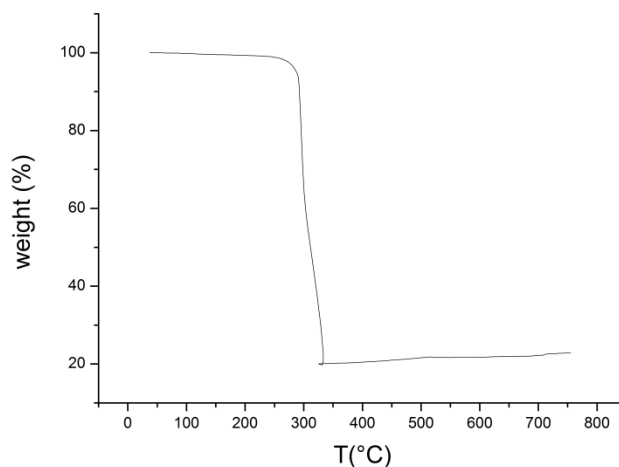


Figure 52: Thermogravimetric analysis of Cu(Ald2) complex.

From the thermogram is therefore possible to calculate the weight percentage of CuO residue and comparing with the theoretical values; the theoretical and experimental values of the weight of the residues are reported in Table 5.

Table 5: Thermogravimetric analysis of Cu(II) complexes.

Residue	Cu(Im) (weight %)	Cu(Ald1) (weight %)	Cu(Ald2) (weight %)	Cu(Ald3) (weight %)
Theoretical	8.1	9.7	23.5	26.0
Experimental	9.1	11.4	21.9	24.7

As is possible to verify in Table 5 the theoretical values are in agreement with those experimental.

Regarding Cu(Im) complex, we have obtained single crystals suitable for X-Ray analysis by slow evaporation of 1,2-dichlorobenzene solution and its molecular structure has been solved and presented in Figure 53. Crystallographic data are reported in Table 6.

Inside monoclinic cell (space group $P21/c$) there is one full molecule and other half molecule sitting on inversion center. For simplicity one only molecule is presented in Figure 53. Copper atom has a square planar coordination with two nitrogen and two oxygen atoms with trans configuration.

Table 6: Crystal data and structure refinement details for Cu(Im).

Chemical formula	C ₈₄ H ₁₁₄ Cu _{1.5} N ₃ O ₁₂
Crystal size, mm	0.4 × 0.5 × 0.5
Crystal habitus, colour	Prism, orange
Formula weight	1453.09
Temperature (K)	173
λ (Å)	0.71069
Crystal system	Monoclinic
Space group	<i>P21/c</i>
<i>a</i> (Å)	32.380 (3)
<i>b</i> (Å)	10.450 (1)
<i>c</i> (Å)	23.042(3)
α (°)	90
β (°)	97.96(2)
γ (°)	90
Volume (Å ³)	7721.5(7)
<i>Z</i>	4
D_{calcd} (g·cm ⁻³)	0.938
μ (mm ⁻¹)	0.328
<i>F</i> (000)	2308
Theta range (°)	3.04, 27.52
Reflections collected	50230
Unique observed reflections	15728 [R(int) = 0.0466]
Data/parameters	15728/913
R1 ^[a] , wR2 ^[b] [I>2 σ (I)]	0.0586, 0.1528
R1 ^[a] , wR2 ^[b] (all data)	0.1198, 0.2007
Largest diff. peak and hole (e·Å ⁻³)	0.794, -0.706

$$[a] R_1 = \frac{\sum ||F_o| - |F_c||}{\sum |F_o|}$$

$$[b] wR_2 = \left[\frac{\sum w(F_o^2 - F_c^2)^2}{\sum w(F_o^2)^2} \right]^{1/2}$$

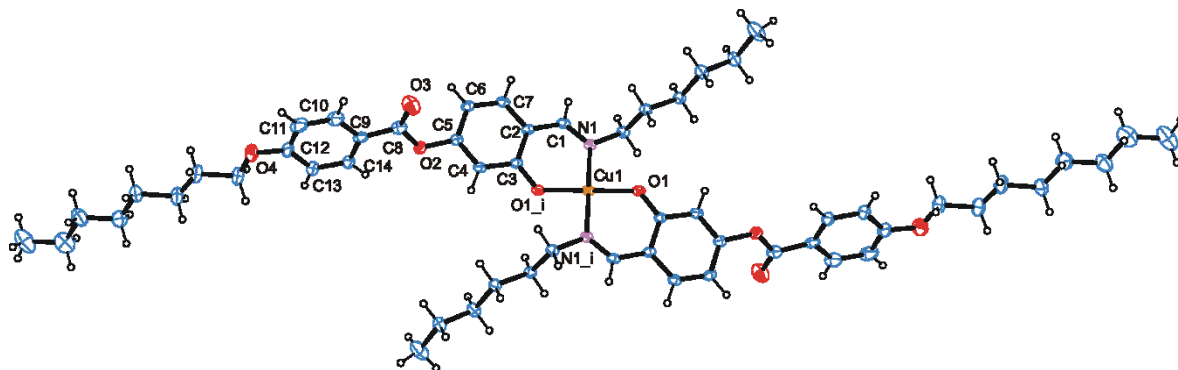


Figure 53: Ortep-3 view of Cu(Im) with ellipsoids drawn at 30% probability level. Hydrogen atoms are omitted for clarity. Symmetry transformation used to generate equivalent atoms: $_i$: $-x, -y, -z$ (the molecule lies on a crystallographic inversion centre). Selected bond distances and angles (\AA , $^\circ$): Cu1-O1 = 1.887(3), Cu1-N1 = 1.983(3), O1-Cu1-N1 = 91.5(1), O1-Cu1-N1 $_i$ = 88.5(1), N1-Cu1-N1 $_i$ = 180.0, O1-Cu1-O1 $_i$ = 180.0, N1-C1-C2-C3 = -8.2(6), N1-C1-C2-C7 = 174.8(3), O3-C8-C9-C10 = 0.1(7).

The molecules sitting on inversion centre show a perfectly planar coordination whereas for the other molecule the square planar coordination is partly distorted (O-Cu-O = 158.4 (1), N-Cu-N = 159.1 (1)). Phenyl C2 is almost coplanar to coordination plan of the metal (angle between average planes is 14.0 (5) $^\circ$). Instead, in the case of phenyl C9 average plane, the dihedral angle drawn with the metal coordination plane is 77.2(3) $^\circ$.

The different Cu(II) complexes were therefore tested as catalyst in the polymerization reaction, based on the 2,5-oxidation of the 3-(4-alkoxyphenyl)-thiophene monomers, as sketched in Figure 54.

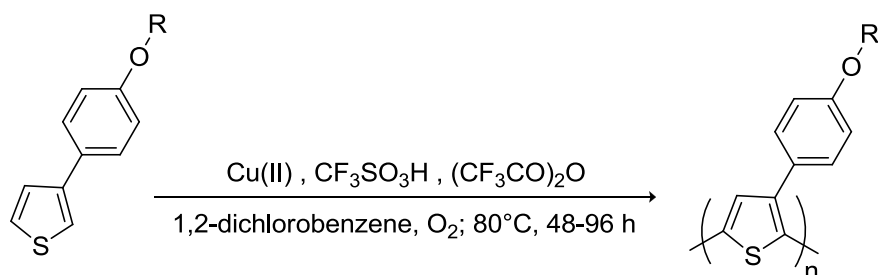


Figure 54: Synthesis scheme of polythiophenes using Cu(II) complexes.

As starting point, we used 4-octyloxyphenylthiophene and the reaction conditions employed in the previously discussed vanadyl catalyzed oxidative coupling reaction (section 3.2, Figure 33). We then carefully optimized the polymerization after a wide screening of the effects of several reaction parameters (temperature, time, catalyst and co-catalyst concentration).

In particular, in the case of Cu(Ald1), Cu(Ald2) and Cu(Ald3) catalyzed polymerization, the same optimized reaction parameters were found. The reactions were conducted at higher temperature (80°C) and for longer times (48 h) as compared to the case in which VO(acac)₂ was used as catalyst. Moreover, a solvent with higher boiling point (1,2-dichlorobenzene) and greater amounts of TFMSA and TFA were employed.

For what concerns Cu(Im) catalyzed reaction, a comparable amount of TFMSA and TFA were employed, but even longer times (96 h) were utilized.

Using the described copper based catalysts, PT8 polymers were obtained in a yield ranging between 23 and 36 %.

Considering the just discussed data, we can assume that the Cu(II) complexes have lower activity as compared to VO(acac)₂, because higher temperature, longer times, greater

amount of TFMSA and TFA were needed to achieve comparable yields. The lower reaction rate can in turn have a good effect on the regioregularity of the obtained polymer as described previously. To qualitatively assess the regioregularity degree of poly-(3-(4-octyloxy)phenyl)thiophenes prepared by using copper complexes as catalysts, we performed a careful UV-Vis analysis on thin films of these polymers.

In Particular polymer films were obtained from 1,2-dichlorobenzene solution (10 mg/ml) heated at 100°C, via spin-coating. Afterwards, the films were annealed for 15 minutes, at 150°C in air. UV-Vis spectra show no changes before and after annealing, as the films are already well structured before of annealing process. UV-Vis spectra of polymer films are reported in Figure 55.

From a qualitatively point of view the spectra of PT8 prepared using Cu(Im) and Cu(Ald1) appeared more defined while the spectra of PT8 obtained by Cu(Ald2) and Cu(Ald3) featured some absorption at ~ 450 nm (see Figure 55).), typical of regioirregular sequences. All the spectra polymers prepared through Cu(II) complexes show a stronger redshift of λ_{\max} than spectra of PT8 prepared through VO(acac)₂. Also the vibronic structure is more definite and a higher regioregularity degree can be assumed as compared to the polymers prepared by vanadyl catalyzed polymerization (90 %).

Particularly impressive is the optical behavior of PT8 prepared using Cu(Ald1) that is characterized by maximum absorption peak at 618 nm with a shoulder at 678 nm (see Table 7 in which the optical features of the different polymer films are reported).

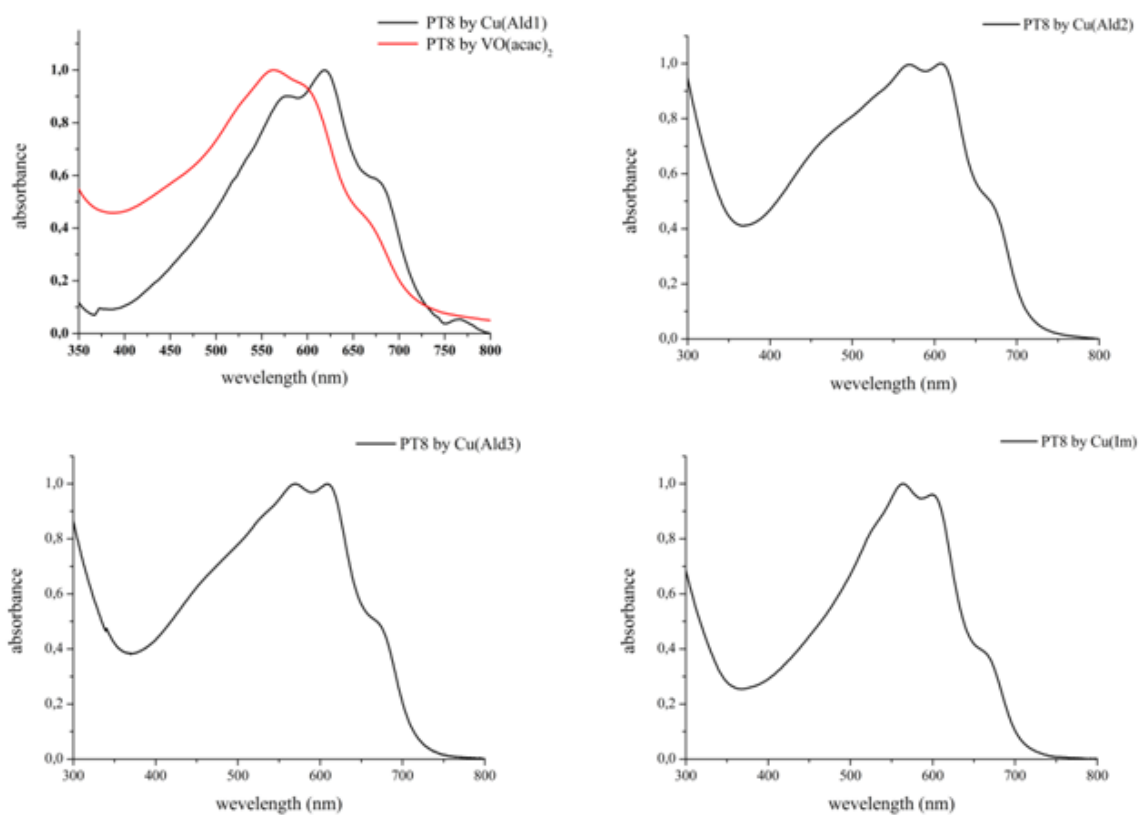


Figure 55: UV-Vis spectra of polymer films.

Table 7: Dates related to λ_{\max} values and vibronic structure of polymer films

PT8	Cu(Ald1)	Cu(Ald2)	Cu(Ald3)	Cu(Im)	VO(acac) ₂
λ_{\max} (nm)	618	608	608	563	562
<i>Vibronic Structure</i>	578	570	570	598	603
(nm)	618	608	608	668	664
	678	669	669		

While UV-Vis spectra can provide only a qualitative evaluation of the regioregularity of the polymers, ^1H NMR analysis was used in order to investigate deeply the HT content in polymers synthesized using Cu(II) and VO(acac)_2 complexes as catalysts.

Particularly, we have investigated the proton on position 4 of the thiophene ring because it can be used for the quantitative determination of the regioregularity of reported polymers, being in fact protons of the different configurational triads (shown in Figure 32) characterized by slightly different resonance values.

The ^1H NMR spectrum of PT8 prepared using Cu(Ald1) complex is reported, as example in Figure 56, with the insight representing the aromatic part.

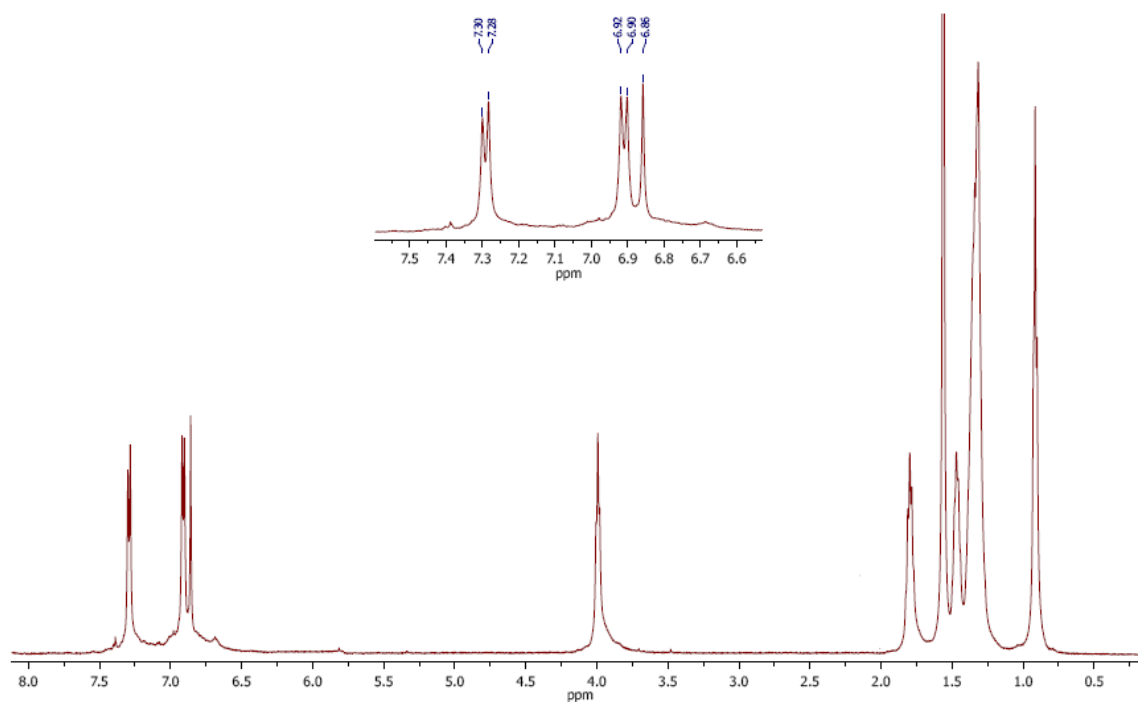


Figure 56: ^1H -NMR spectrum of PT8 prepared by Cu(Ald1) complex.

By performing a decoupling procedure during spectrum acquisition it was possible to avoid the partial overlapping of one of benzenic signals (a doublet, without decoupling) with the thiophenic singlet under investigation (see aromatic part of the ^1H NMR spectrum of PT8 in Figure 56). As earlier discussed (see 3.1 Paragraph), the thiophenic signal is composed of a main peak and three other lower signals, corresponding to the four possible configurational triads. In Figure 56 the isolated thiophenic peaks relative to PT8 prepared by using the 4 different copper catalysts are presented. By operating a deconvolution procedure it was moreover possible to separate the different contributions given to this signal by the 4 different configurational triads singlet.

Taking advantage of a previous work reported in the literature on poly(3-dodecylthiophene) [49] we have assigned each singlet signal to the corresponding configurational triads (the higher peak at higher field corresponding to HT-HT triad and then moving towards lower fields, in sequence the peaks corresponding to HT-HH, TT-HT and TT-HH triads). Then we have measured the area of each peak obtained by deconvolution process (see Figure 57), which concurs with the fraction of a corresponding triad.

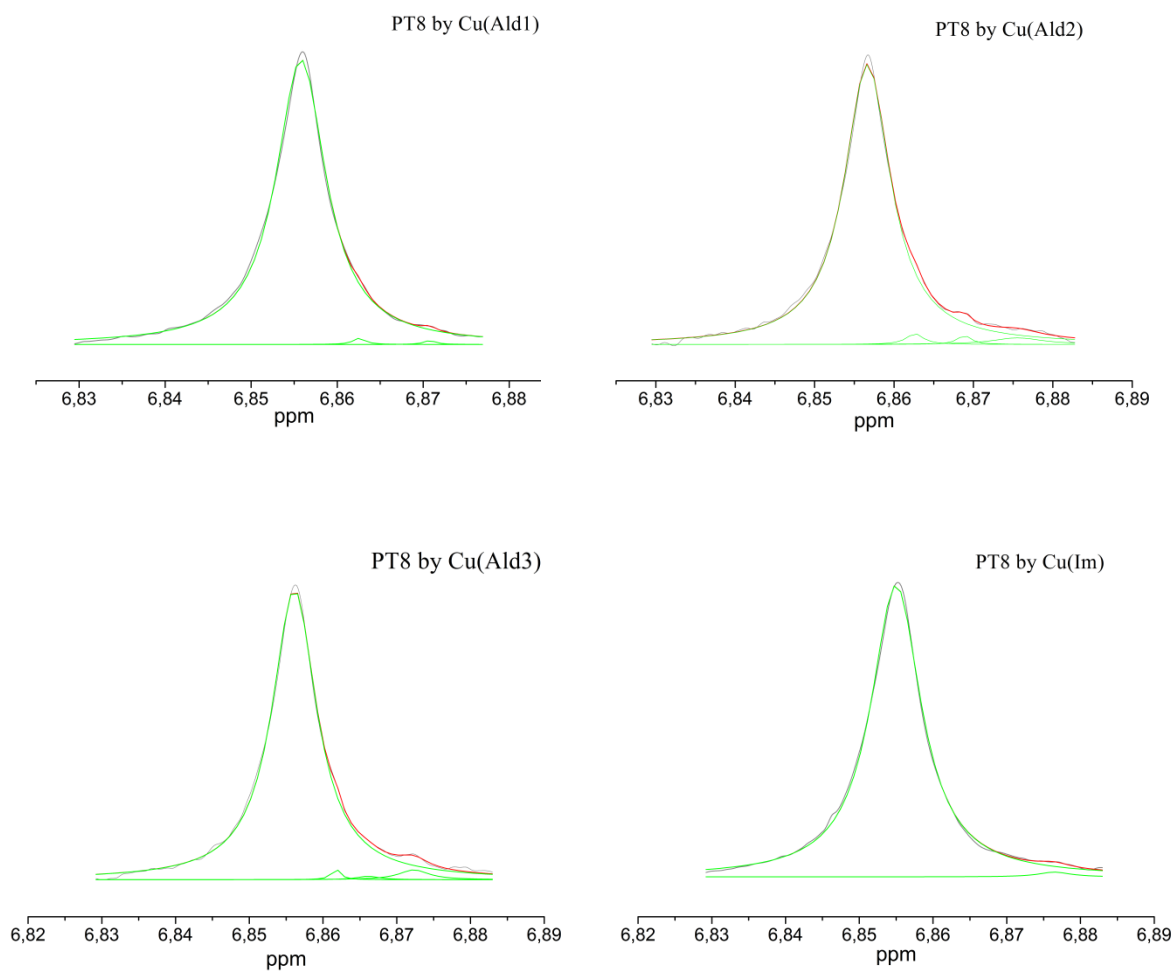


Figure 57: Deconvolution process applied to thiophenic singlets.

Moreover the observed fractions of diad and triad may be interpreted in terms of the statistics of the polymerization involving the propagation steps as it is shown in Figure 58.

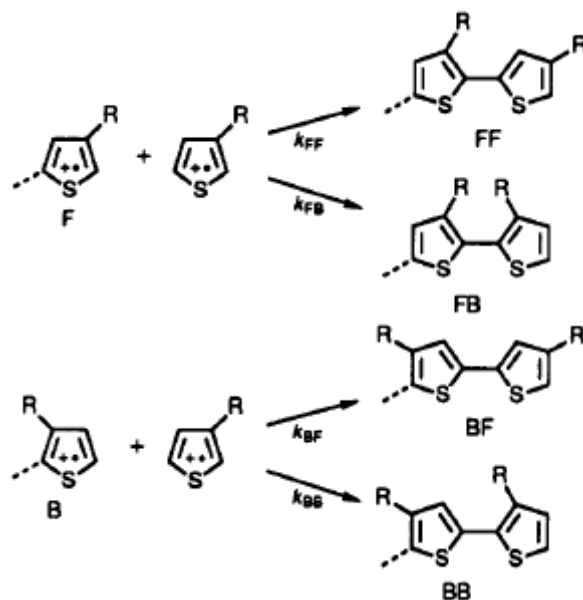


Figure 58: Diads that can be formed in polymerization process. F and B denote the forward and the opposite orientations of monomer units defined for propagating terminal radicals, respectively.

It has been suggested that the electrochemical polymerizations of polypyrroles and polythiophenes take place by the condensation of the radical cation of the monomer with the radical cation of the propagating terminal [49]. Moreover the observed fractions of diad and triad may be interpreted in terms of the statistics of the polymerization involving the propagation steps as it is shown in Figure 58, k_{xy} is the rate constant of step XY. We define and use here the fraction FX of X as the radical cation of propagating terminal with the

relation that $FF + FB = 1$ and the additional probability P_{xy} of step XY with the relations that $PPF + PFB = 1$ and $PBF + PBB = 1$.

Then we introduce the independent parameters X , α , and β as follows:

$$F_F = C \quad (17)$$

$$P_{FF} = K_{FF} / (K_{FF} + K_{FB}) = \alpha \quad (18)$$

$$P_{BF} = K_{BF} / (K_{BF} + K_{BB}) = \beta \quad (19)$$

Thus it is worked out the equation system follows, through least squares analysis method:

$$\left\{ \begin{array}{l} HT - HT = (1 - \beta)^2 + C(\alpha + \beta - 1)(\alpha - \beta + 1) \\ HT - HH = C(\alpha - \beta + 1)(1 - \alpha) \\ TT - HT = (\alpha - \beta + 1)\beta + C(-\alpha + \beta - 1)\beta \\ TT - HH = (1 - \alpha)\beta \end{array} \right. \quad (20)$$

Finally, the resolution of this equation allows obtaining HT values:

$$HT = (\alpha\beta - \beta + 1)C(\alpha - 1)(\alpha - \beta + 1) \quad (21)$$

The obtained regioregularity degree (defined as the amount of HT dyads) are reported in Table 8. We can see that a extremely high regioregularity can be obtained using Cu(II)

complexes, with a minimum of 96 % (when Cu(Ald2) is used up to a maximum of 99 % (for Cu(Im) and Cu(Ald1)). These values are significantly higher than the regioregularity obtained for the same polymers prepared by using VO(acac)₂ (see the same NMR analysis of the thiophenic peak carried out on this polymer in Figure 59) as catalyst and are comparable to the values reached by using the classical McCullough and Rieke methods for PAT's synthesis. As compared to those methods, it has to be stressed that the novel synthetic methodology that we developed is much cheaper and straightforward: the step of monomer dibromination is in fact avoided and the employed catalyst is cheaper and not air sensitive so that a protected environment is not required.

An Italian patent request has been submitted for this novel synthesis of poly-(3-(4-alcoxyphenyl)thiophenes) endowed with high regioregularity [50].

Table 8: The HT values of PT8 synthesized through Cu(II) complexes.

PT8	Cu(Ald1)	Cu(Ald2)	Cu(Ald3)	Cu(Im)	VO(acac) ₂
HT(%)	99.15	96.25	97.17	98.96	90.0

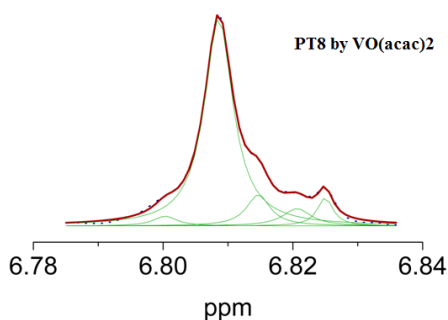


Figure 59: Deconvolution process applied to thiophenic singlets of PT8 prepared using VO(acac)₂.

For what concerns the polymerization mechanism, further studies are needed and we can just make some speculation on the basis of some experimental results. We can suppose that a redox catalytic cycle occurs, whose Cu(II) oxidize to radical cation the thiophene ring, with its reduction to Cu(I). The catalysis may be promoted by the Cu-S interaction between the copper atom of the complex and sulfur atom of thiophene. The oxygen can oxidize again Cu(I) to Cu(II), with water production in acidic environment and thus closing the catalytic cycle.

After having optimized the just discussed polymerization reaction on the synthesis of PT8, we extended this procedure in the synthesis of other systems with the aim of improving the processability properties. We have in fact found that PT8 synthesized using Cu(II) complexes result insoluble at room temperature, and are soluble only at high temperature (higher than 120 ° C) in chlorinated solvent as chloro or o-dichlorobenzene. Accordingly, we have decided to synthesized PT6-8 copolymer and PT8Iso omopolymer employing Cu(Ald1) and the same optimized conditions of reaction discussed earlier, to obtain both soluble and thus processable polymers and high regioregularity (synthesis scheme is reported in Figure 60).

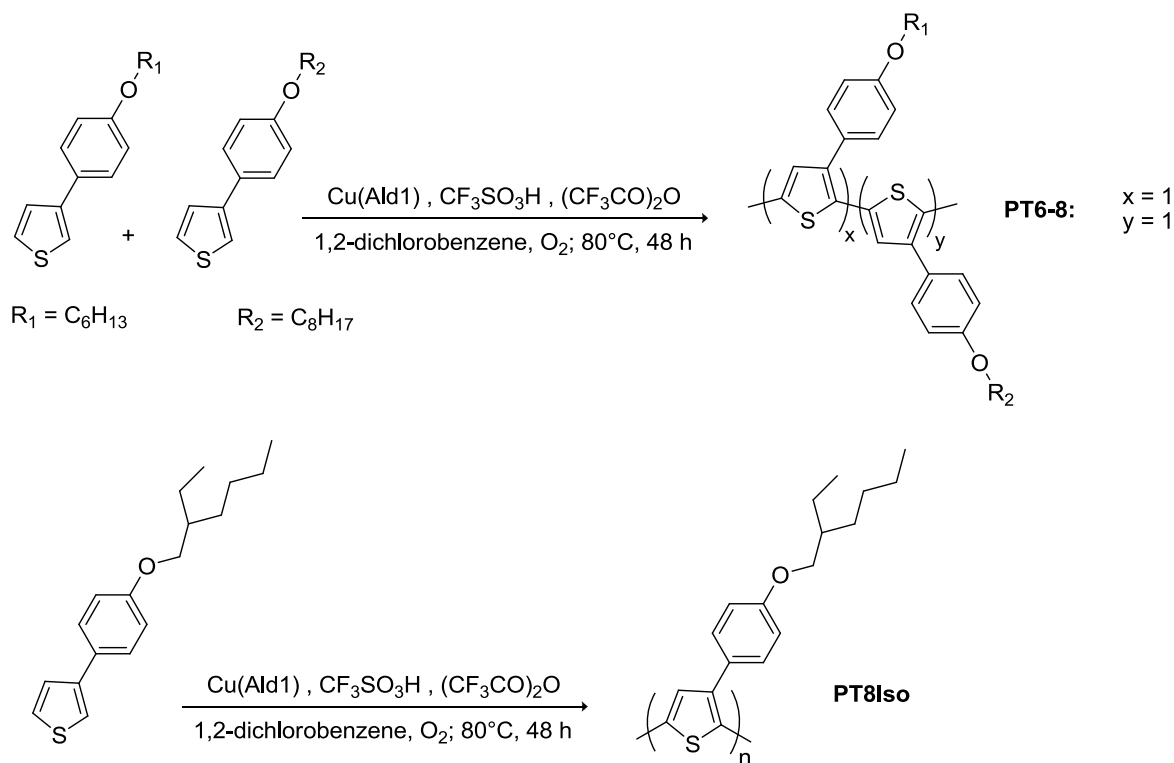


Figure 60: Synthesis scheme of PT6-8 and PT8Iso.

The UV-Vis spectra of the films of PT6-8 and PT8Iso are shown in Figure 61 from which a well defined vibronic structure and low absorbance in the regioirregualr zone (around 450 nm) can be inferred.

Also in this case, the quantitative regioregularity degree was calculated by means of 1H NMR analysis.

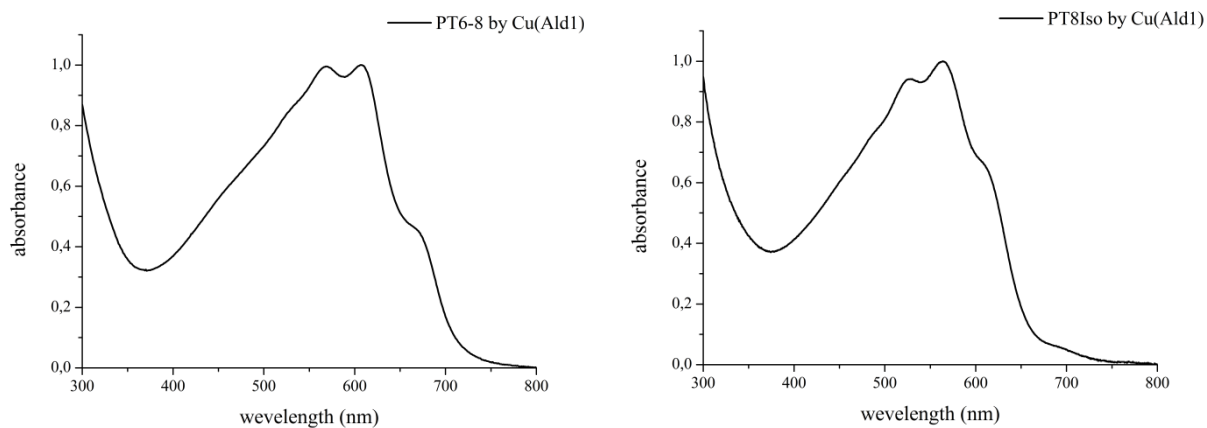


Figure 61: UV-Vis spectra of PT6-8 and PT8Iso.

In fact HT content of 95.72 and 96.90 %, respectively for PT6-8 and PTIso8, were computed, values comparable with those characterizing PT8 synthesized using Cu(Ald1) as catalyst (see Table 9).

Table 9: The HT values of PT6-8 and PT8Iso.

	PT6-8	PT8Iso
HT(%)	95.72	96.90

In Figure 62 the ^1H NMR spectra, limited to the thiophenic proton area, are reported along with the deconvolution procedure.

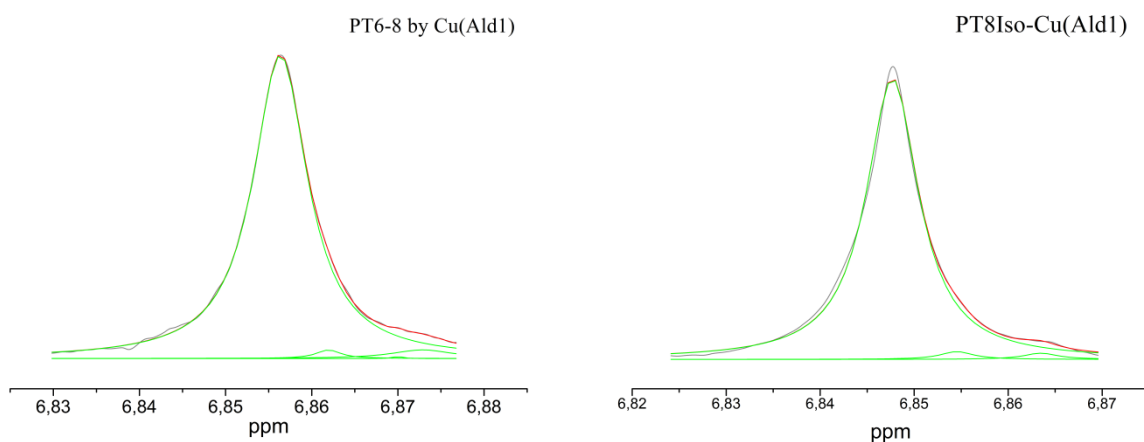


Figure 62: Deconvolution process applied to thiophenic singlets.

For what concerns their solubility, PT6-8 is slightly more soluble of PT8, while PT8Iso is soluble in chlorinated solvent even at room temperature and can be considered as an interesting candidate for application in organic photovoltaics.

3.4 Measurement of FET Mobility of PT8-Cu(Ald1)

As earlier mentioned, we have investigated about the conductivity properties of PT8 synthesized using Cu(Ald1), through preliminary measurements of FET mobility.

In order to realize the FET device, PT8-Cu(Ald1) was deposited on bottom-contact substrate by solution (5 mg of polymer in 1 ml of 1,2-dichlorobenzene) which after heating at 120°C was filtered with PTFE 0.2 μm filter and deposited via spin-coating at 700 rpm. Afterwards, the device was annealed at 150°C for 30 minutes.

The obtained device's image is reported in Figure 63.

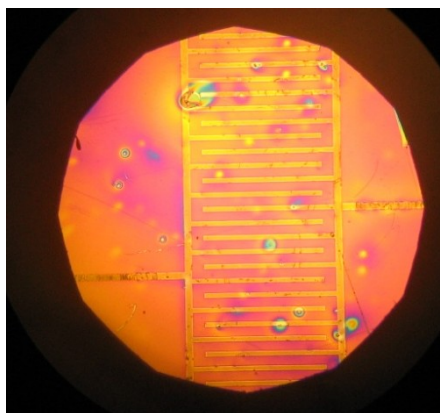


Figure 63: Film of PT8-Cu(Ald1) deposited via spin-coating onto FET device.

PT8-Cu(Ald1) exhibits FET hole mobility up to $\mu = 1.0 \cdot 10^{-4} \text{cm}^2 \text{V}^{-1} \text{s}^{-1}$. As a matter of comparison, an analogous transistor based on P3HT as active material was prepared and tested under the same experimental conditions. The measured mobility was only one magnitude order higher than value shown by the PT8 based transistor and this can be considered a very encouraging result considering that further optimization can be

performed. The device current-voltage characteristics in saturation regime are shown in Figure 64

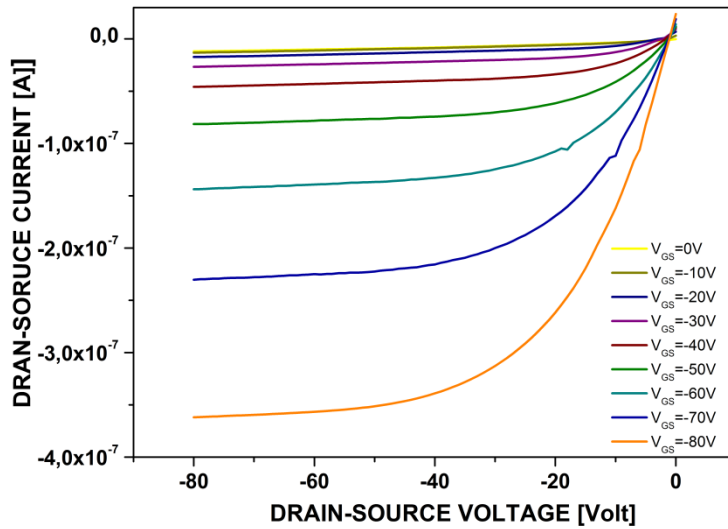


Figure 64: Current-voltage characteristics of PT8-Cu(Ald1) based device.

The measurements were carried out in the laboratories of the Physic Department, University of Naples “Federico II” (Italy), Research Group of Prof. Antonio Cassinese.

4 SYNTHESIS OF ALKYLTHIADIAZOLE AND ALKYLTRIAZOLE-SUBSTITUTED PERYLENEBIS (DICARBOXIMIDES) FOR APPLICATION IN FET DEVICES

4.1 Introduction

Perylene-3,4,9,10-tetracarboxylic acid diimides (PDI) derivatives represent a class of organic compounds that have been extensively investigated and have found, since the beginning of the last century, a wide application in the field of high performance industrial pigments because of their high color strength, weather fastness and heat stability [51],[52]. Today, perylene pigments are mainly used in the coloration of automotive paints, synthetic fibers and engineering resins. PDI derivatives present as well a series of other appealing features, such as very high fluorescence quantum efficiency, a strong electron acceptor character, excellent photochemical stability and two photon absorption properties, that make them interesting candidates for use in different subfields of organic electronics and photonics: they are among the most promising and versatile n-type semiconductors due to their high electron affinity, their remarkable chemical stability, their outstanding optical and electronic properties and the considerable variety of possible chemical functionalization. The excellent charge transporting character of PDI is favorable for organic thin film transistors (OTFT) [53] due to the rapid and effective electron transfer process. Furthermore, it is possible to obtain devices that show high-performance, excellent mobilities, light weight, mechanical flexibility and low-cost production. PDI derivatives have so far been used as active materials in newly developed devices as, fluorescent light collectors, organic solar cells and optical power limiters.

PDI derivatives are characterized by low energies of LUMO frontier orbitals and this feature make them one of the most important class of materials for n-channel OTFT: electron transport in organic transistors occurs, in fact, through an hopping mechanism between localized LUMO states and the more stable are these ones, the more resistant are the anionic radical charge carriers against electronics traps or oxidation toward moisture and oxygen. A LUMO energy between -4.0 and -4.3 eV has been identified as the energetic threshold featured by an organic material so that it can be used as active layer in OTFT efficiently working under ambient conditions.

Derivatives of PDI are generally prepared in two different ways, by functionalizing the imide nitrogen or the perylene core itself (bay substitution). In both cases, the use of strong electron-withdrawing groups has been used to stabilized the LUMO energy of the molecule, even if at a different extent. The effect of imide substitution on frontier orbitals energy is merely inductive, being the imide nitrogen located on nodal planes of both HOMO and LUMO [54] (this, in turn, determines also a little change in the optical properties, being HOMO and LUMO stabilized of the same energy amount). Substitution in the bay position leads instead in a more dramatic change in both the electronic and optical features of the molecule. At the same time anyway, particularly when bulky substituent are used, a disruption of molecule planarity can occur, negatively affecting the property of charge transporting [55]. Both the kind of derivatives have been used for the fabrication of ambient stable OTFT: functionalization of the imide nitrogen with fluoroalkyl or fluorophenyl moieties, as well as substitution in the bay position with cyano and halogen groups, have allowed the preparation of devices with excellent performance and air stability.

4.2 Alkylthiadiazole and alkyltriazole-substituted perylenebis(dicarboximides)

Starting from these considerations, we have synthesized a new class of PDI derivatives functionalized at the imide nitrogen with a thiadiazole and triazole group. Thiadiazole and triazole have electron withdrawing properties that can help in stabilizing, for inductive effect, the LUMO energy of the molecule. Indeed, in a recent work [55], a series of soluble PDI, among which a thiadiazole substituted PDI, were electrochemically investigated: it was found that the thiadiazole substituted PDI had a first reduction potential about 0.3 V more positive than alkyl derivative of PDI. This remarkable difference, correlated to a much stable LUMO orbital in thiadiazole containing PDI, suggests the possibility to investigate whether this kind of material can be a good active layer for ambient working OTFT. Moreover, being the thiadiazole and triazole pentaatomic heterocycles (in addition with no *ortho*-hydrogens), we have assumed that in the molecular conformation they remains coplanar with the perylene core (unlike what happens instead when the nitrogen is substituted with a phenyl ring) and this could lead to a tighter packing that could in turn hinder the oxygen penetration and kinetically stabilized the molecule toward oxidation. Moreover we have functionalized the heterocycle rings with different alkyl tails, some linears and the other swallow-tail like in order to increase the solubility.

Regarding the synthetic pathway for the preparation of PDI derivatives functionalized with thiadiazole group, we have developed a particular synthesis strategy that is summarized in Figure 65. The first step is the synthesis of the thiadiazole functionalized by a linear heptyl or tridecyl tail or by a branched 2-hexylnonyl group. We have prepared the heterocycle

through condensation between the proper carboxylic acid and thiosemicarbazide in the presence of POCl_3 as dehydrating agent. Afterwards, PDI derivatives were obtained by the condensation reaction of perylene-3,4,9,10-tetracarboxylic dianhydride (PTCDA) with the proper alkyl-thiadiazole at high temperatures (180°C) in solvents as imidazole with zinc chloride as a catalyst in nitrogen atmosphere. After 4h, concentrated solution of hydrochloric acid was added and the reaction system was allowed to react for 2h at 150°C .

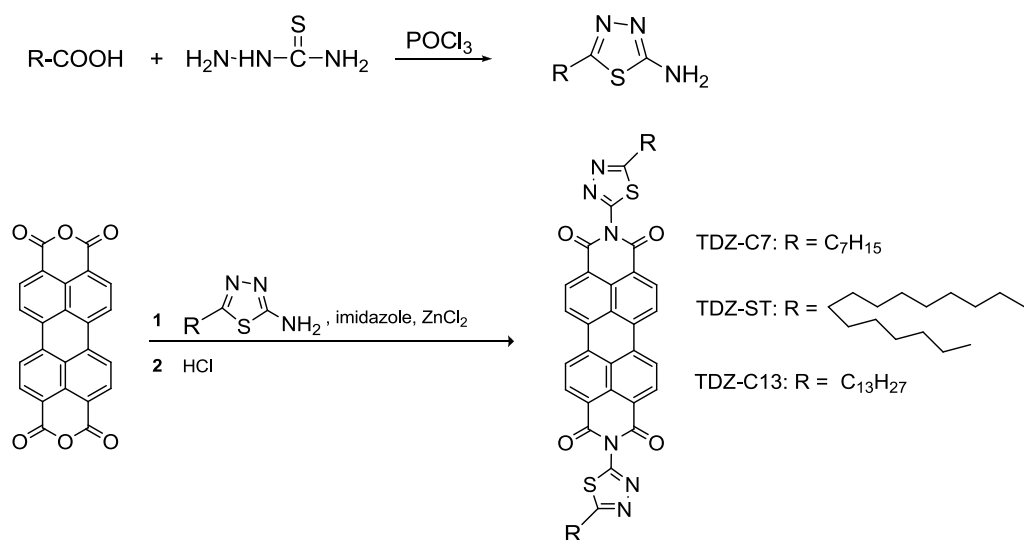


Figure 65: Synthesis scheme of PDI functionalized with thiadiazole group.

The scheme for the synthesis of the triazole functionalized PDI is shown in Figure 66. Also in this case the first step has been the preparation of the alkyl-triazole, obtained by the condensation of caprylic acid and 1,3-diaminoguanidine hydrochloride in the presence of polyphosphoric acid (PPA) as dehydrating agent, for 12h at 200°C . Successively, we have

obtained PDI derivative intermediate by the condensation reaction of PTCDA with triazole refluxed with pyridine and imidazole in nitrogen atmosphere for 12h.

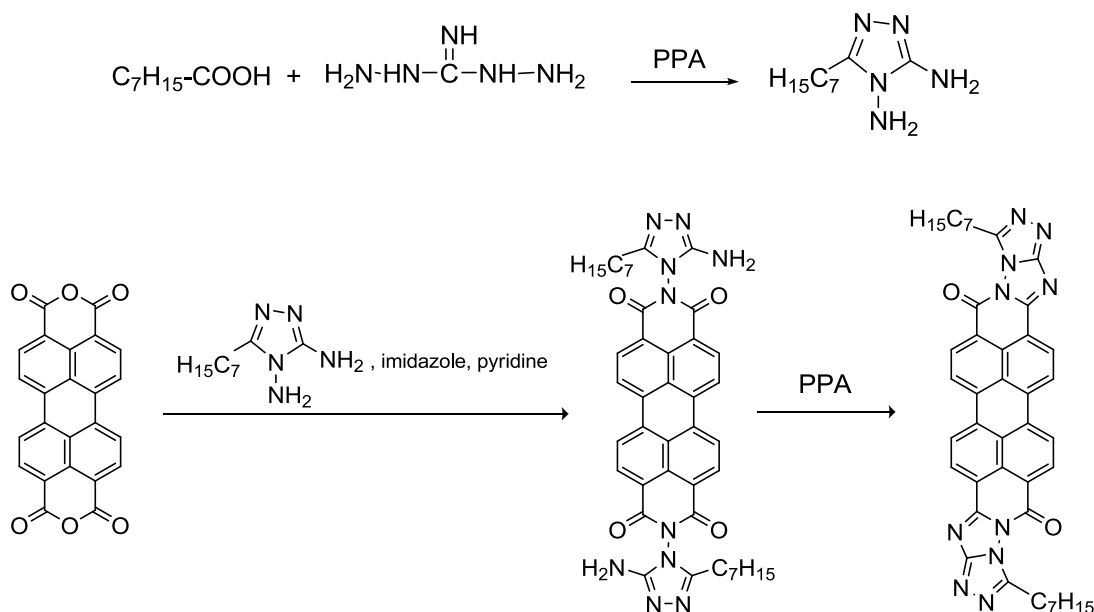


Figure 66: Synthesis scheme of TR-C7.

Finally, TR-C7 was synthesized by the cyclization reaction of PDI-derivative intermediate in PPA for 12h at 150°C.

The purity of the compounds have been checked by elemental analysis, 1H -NMR and MALDI mass spectrometry and all the data are consistent with the proposed structure.

Optical observations with a polarizing microscope and differential scanning calorimetry analysis performed on all the chromophores did not indicate the presence of phase transition and also the melting point was not detectable because the decomposition process

started before. Thus we have decided of investigate deeply about the thermal stability of the samples.

The decomposition temperature of all the PDI derivatives was obtained by means of a thermogravimetric analysis. The knowledge of this parameter is of fundamental importance during the fabrication of FET devices by thermal evaporation of the molecules: to avoid in fact thermal degradation of the chromophores during the process a safe evaporation temperature, well below the decomposition temperature, has to be chosen. The analysis was performed under nitrogen flow at a rate of 10°C/min and, as example, the thermogram of TDZ-C13 (in which the loss of specimen weight is plotted against temperature) was reported in Figure 67; the decomposition temperatures, calculated as the temperature corresponding to the loss of 5% weight, are reported in Table 10.

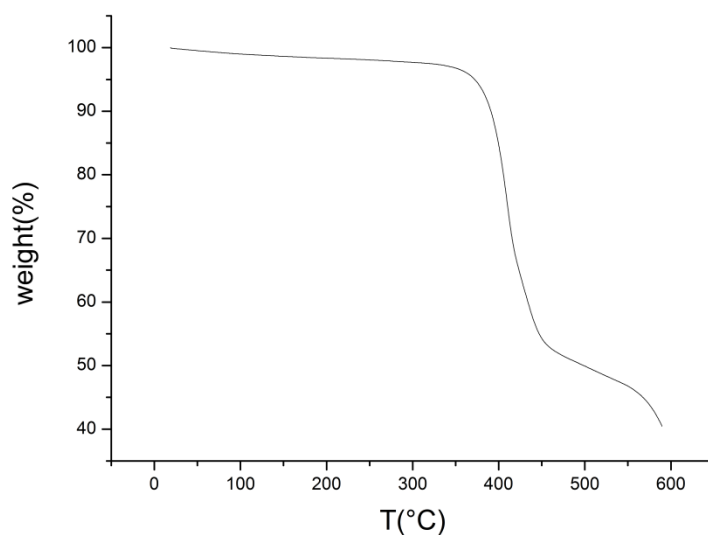


Figure 67: Thermogravimetric analysis of TDZ-C13.

Table 10: Temperatures of decomposition of PDI derivatives.

	TDZ-C7	TDZ-C13	TDZ-ST	TR-C7
T _d (°C)	354	372	369	345

All the PDI derivatives obtained present a fair good thermal stability with temperatures of decomposition well above 300°C, that allow their safe use in operating conditions.

Successively PDI derivatives were characterized by measurements of relative fluorescence quantum yields in solution. The fluorescence quantum yield of a specific molecule is defined as the ratio of the number of photons emitted compared to the number of photons absorbed:

$$\Phi_f = \frac{\text{photons emitted}}{\text{photons absorbed}} \quad (19)$$

We have calculated fluorescence quantum yields through a dilute solution relative method [56] that is based on the comparison of the Φ_f of the samples with Φ_{fS} of a suitable standard. The standard used was quinine sulfate dihydrate which has $\Phi_{fS} = 0.546$ in H₂SO₄ 1 N when is excited at $\lambda = 365$ nm according to Melhuish [57].

For each sample were carried out the absorbance and emission spectra of diluted chloroform solutions and the spectra are reported in Figure 68 (the thiadiazolic derivatives) and Figure 69 (the triazole derivative).

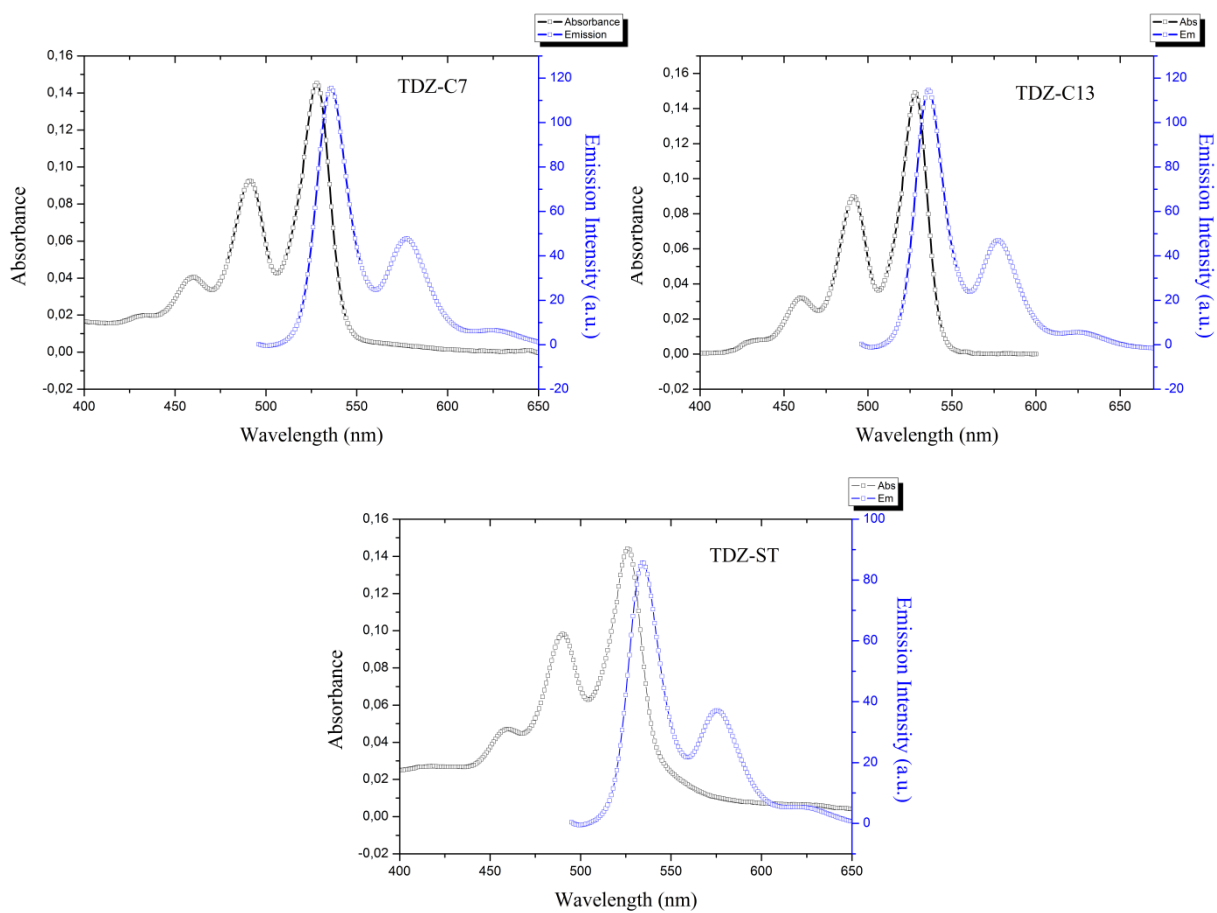


Figure 68: Absorbance and emission spectra of the PDI derivatives functionalized with thiadiazole group.

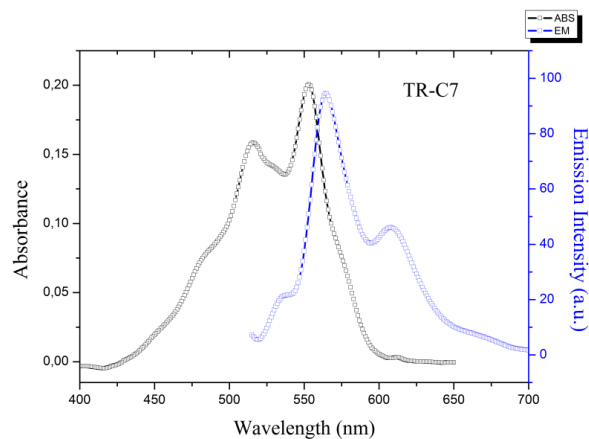


Figure 69: Absorbance and emission spectra of TR-C7.

The emission spectra were obtained using excitation wavelength corresponding to second peak of the structured absorbance spectrum. Thus plotting the values of emission area against the absorbance values corresponding to the absorption maximum, it is possible to obtain a set of points that can be fitted by a straight line according to the method of least squares. The value of the line's slope can be used to calculate Φ_f through the following expression:

$$\Phi_f = \Phi_{fS} \frac{B}{B_S} \cdot \frac{\eta^2}{\eta_S^2} \quad (20)$$

where Φ_f and Φ_{fS} are quantum yield of the sample and standard respectively; B and B_S are the slopes of the straight line of the sample and standard respectively; η and η_S are

refractive index of the solutions of the sample and standard respectively. The fluorescence quantum yields values calculated are reported in Table 11.

Table 11: Values of the fluorescence quantum yields of the PDI derivatives.

Excitation wavelength used: ^a 491 nm; ^b 490 nm; ^c 492 nm; ^d 516 nm.

	TDZ-C7 ^a	TDZ-C13 ^b	TDZ-ST ^c	TR-C7 ^d
Φ_f (%)	72	78	58	37

As far PDI derivatives functionalized with thiadiazole groups are concerned, quantum yields values are quite high.

Discussing more in details the UV-Vis spectra, the thiadiazolic PDI derivatives (Figure 68) feature a strong vibronically structured absorptions with maxima \sim 525 nm, an optical behavior similar to the PDI derivatives substituted at the imide nitrogen with an alkyl or aryl group. Generally, we can identify three peaks in the wide range of 400-550 nm, which corresponds to the transitions of 0 \rightarrow 2, 1 \rightarrow 2 and 0 \rightarrow 1. Notably, the emission and absorption spectra are well mirrored, giving strong evidence of Frank-Condon principle. It has been proven that the imide substituent has a negligible influence on the absorption and emission properties bisimide because of the nodes in the orbitals HOMO and LUMO at the nitrogen atoms [26]. This causes a decoupling of the chromophore from these single bonds. Because of solubility issues, a quantitative determination of molar extinction coefficient ϵ of the PDI derivatives under investigation, was possible only for TDZ-St. In particular, ϵ

value for TDZ-ST was found to be $3.1 \cdot 10^4$ in chloroform solution. Slightly higher values are to be expected for the other two thiadiazolic PDI derivatives considering the fact that they bear smaller, optically inactive, alkyl chain.

The optical behavior of TR-C7 is slightly different: first of all quantum yields value is lower than PDI derivatives functionalized with thiadiazole group (see Table 11). Also absorbance and emission spectra (see Figure 69) present some difference. In fact in the case of TR-C7 it is observed a partial loss of vibronic structure in the absorbance spectrum and a slight red-shift of the emission spectrum. We have assumed that this behavior can be related to the increase of conjugation extension in TR-C7 as compared to PDI derivatives that strongly influence the absorption and fluorescence peaks.

4.3 Measurement of FET Mobility of PDI Derivatives

Successively we have used the PDI derivatives to fabricate FET bottom contact devices in order to measure their mobility both in vacuum and under ambient conditions. Such electrical tests were carried out using FET device with SiO₂ gate dielectric or SiO₂ functionalized by organosilane self-assembled monolayers (SAMs). It is known that the gate dielectric of organic transistors has a greater influence on carrier transport and mobility compared to inorganic materials. Organic transistors usually operate in accumulation mode and charge transport typically takes place in the first few monolayers (2–6 monolayers, depending on the material) of the organic semiconductor adjacent to the gate dielectric. As a result, the transistor performance is greatly influenced by properties of this interface. Using functionalized gate dielectric, we can obtain: (i) a decrease charge carrier traps by shielding the conduction path from surface hydroxyl groups and smoothening dielectric surface with a polymer thin layer or molecular monolayer; (ii) tailoring the surface energy of the dielectric or the order of interfacial monolayer in order to control the molecular orientation, assembly, packing and film morphology of semiconductor layer [58]. Moreover, Fontaine et.al [59] demonstrated that this monolayer acts as an excellent electrical insulator, with leakage current densities as low 10^{-8} A cm⁻² for an average field of 5.8 M V cm⁻¹, reduced by about five magnitude orders compared to the bare substrates.

In order to functionalize the SiO₂ thermally grown on the silicon substrate used for the fabrication of our transistors, the following procedure was employed: first, we have treated the Si/SiO₂ substrate with a “piranha” solution (50:50 concentrated H₂SO₄:30% H₂O₂

(v/v)) at 120°C for 15 min in order to obtain the release of the –OH groups from surface. Successively, the substrates were exposed to 1,1,1,3,3,3-hexamethyldisilazane (HMDS) vapors under rigorously inert atmosphere, into a sealed glass vessel at room temperature for 4 days. This procedure leads to monolayers of organosilane compounds covalently linked to superficial –OH groups. Then, substrates were carefully washed with several organic solvents to remove physisorbed coupling agent. Substrate functionalization is reassume in scheme of Figure 70.

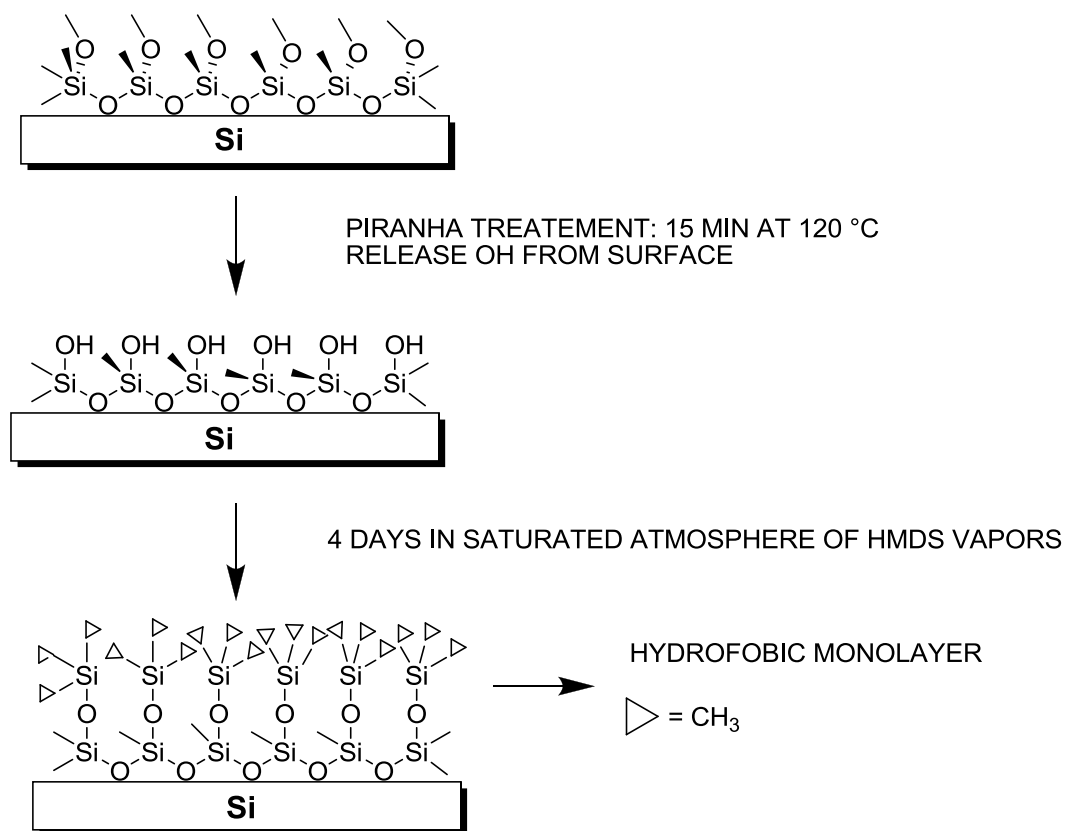


Figure 70: Substrate functionalization with HMDS.

Successively we have characterized the self-assembled coupling layer through advancing aqueous contact angle (θ_a) measurements. Contact angle values of some substrates are reported in Table 12. The contact angles change from $\sim 15^\circ$ for SiO_2 to $\sim 110^\circ$ for the silylated surface. Thus this hydrophobic change in θ_a is consistent with the presence of organosilane homogeneous monolayer on the surface.

Table 12: Contact angle values of some substrates functionalized with HMDS.

Sample	Contact Angle H ₂ O (°)
1	107,0 \pm 1,4
2	108,0 \pm 0,4
3	109,9 \pm 1,0
4	106,2 \pm 0,2

After the substrate functionalization, all the PDI derivatives were thermally evaporated both on bare (Si/SiO₂) and HMDS functionalized substrates (Si/SiO₂/HMDS). For all the samples the chamber was heated up to 100°C (maximum value experimental accessible), the cell temperature was kept at value not above at 290°C and the deposition rate was set at 0.06 nm/min, leading deposition time at 4 h. We have developed this deposition procedure to prevent sample degradation. In fact, in previous tests, the cell temperature was increased up to 320°C and it was utilized 0.5 nm/min as deposition rates. This deposition method led to lower values of mobilities due to the organic sample degradation. Therefore through the new deposition strategy, values of $\mu = 7.5 \cdot 10^{-4} \text{ cm}^2 \text{ volt}^{-1} \text{ sec}^{-1}$ for TDZ-ST were reported.

In this case, the highest mobility was measured in vacuum and through functionalized substrate (see Table 13). Moreover, For TDZ-ST measurement of mobilities was also made with sample deposited by solution (via spin-coating) on functionalized device. In this case lower mobility was reported ($\mu = 5 \cdot 10^{-6} \text{ cm}^2 \text{ volt}^{-1} \text{ sec}^{-1}$). As for TDZ-C13 measurements, the values of $\mu = 1.6 \cdot 10^{-2} \text{ cm}^2 \text{ volt}^{-1} \text{ sec}^{-1}$ were indicated (see Table 13). In this case, the highest mobilities were measured in vacuum and through a bare substrate. Current-voltage characteristics in saturation regime and mobility trends of the devices are shown in Figure 71.

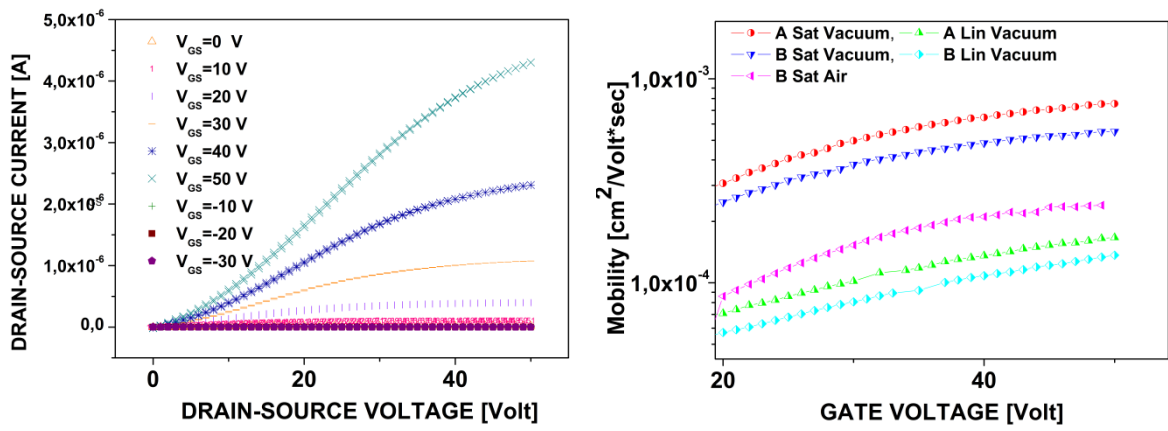
Contrarily regarding mobility measurement of TR-C7, no conduction and field effect were observed. We have supposed that this behavior could be related by the degradation compound during evaporation process.

Table 13: Comparison of the mobility values of TDZ-ST and TDZ-C13.

TDZ-ST	Si/SiO ₂	Si/SiO ₂ /HMDS
μ (cm ² volt ⁻¹ sec ⁻¹)	1.4*10 ⁻⁵	7.5*10 ⁻⁴

TDZ-C13	Si/SiO ₂	Si/SiO ₂ /HMDS
μ (cm ² volt ⁻¹ sec ⁻¹)	1.6*10 ⁻²	8.2*10 ⁻³

TDZ-ST



TDZ-C13

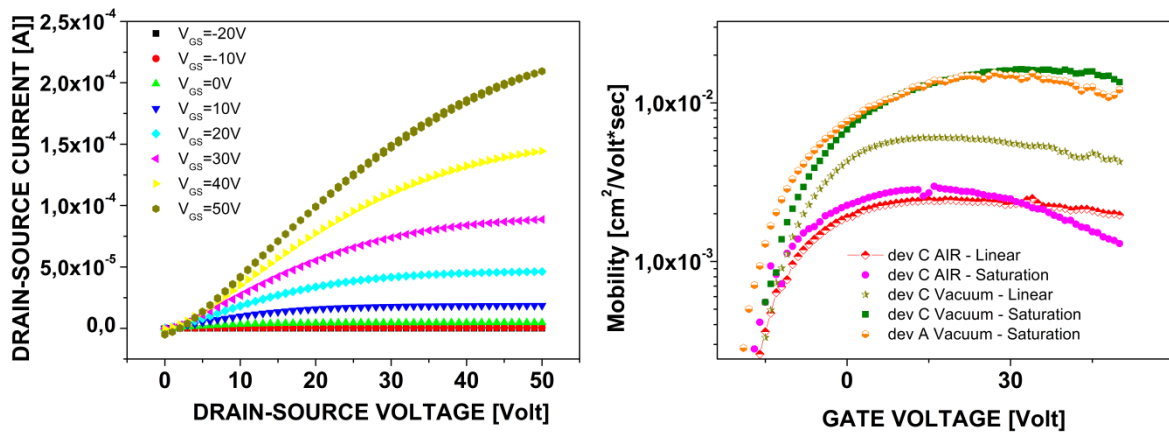


Figure 71: Current-voltage characteristics and mobility trends of OTFT devices.

On the base of such deeply investigation, it seems that the mobility values measured on functionalized and bare substrates are quite similar, thus we can suppose that the performance devices are not affected by superficial treatment. Moreover there is not difference between measurements carried out under vacuum and in air, thus we can consider that the OTFT devices obtained are very stable under operating conditions.

Another important parameter that we have considered is the ratio $I_{\text{on}}/I_{\text{off}}$ in order to value OTFTs performances. This value was extracted from the transfer characteristics for TDZ-ST and TDZ-ST based devices and both show an $I_{\text{on}}/I_{\text{off}} > 10^3$.

Notably, this value is highly dependent on the voltages used, the device geometry, and the dielectric material. Therefore, this value provides a qualitative measure of semiconductor performance, but identical parameters must be used to quantify the results when comparing different materials. The $I_{\text{on}}/I_{\text{off}}$ ratio is also a useful measure of purity, because a high off current can be indicative of high extrinsic doping levels in the semiconductor [60]. Thus, such $I_{\text{on}}/I_{\text{off}}$ ratio can be considered a very encouraging result considering that further optimization of the devices can be performed.

The devices based on TDZ-C13 and TDZ-ST exhibit respectively V_{th} of 9.45 and 24 V. Such values are in good agreement with ones reported in literature for PDI derivatives [61].

The surface morphology of the films obtained by thermic evaporation of TDZ-C13 and TDZ-ST were deeply analyzed with the atomic force microscopy (AFM) images. The films of TDZ-C13 show a growth through elongated islands both on functionalized and bare substrates (see Figure 72).

TDZ-C13

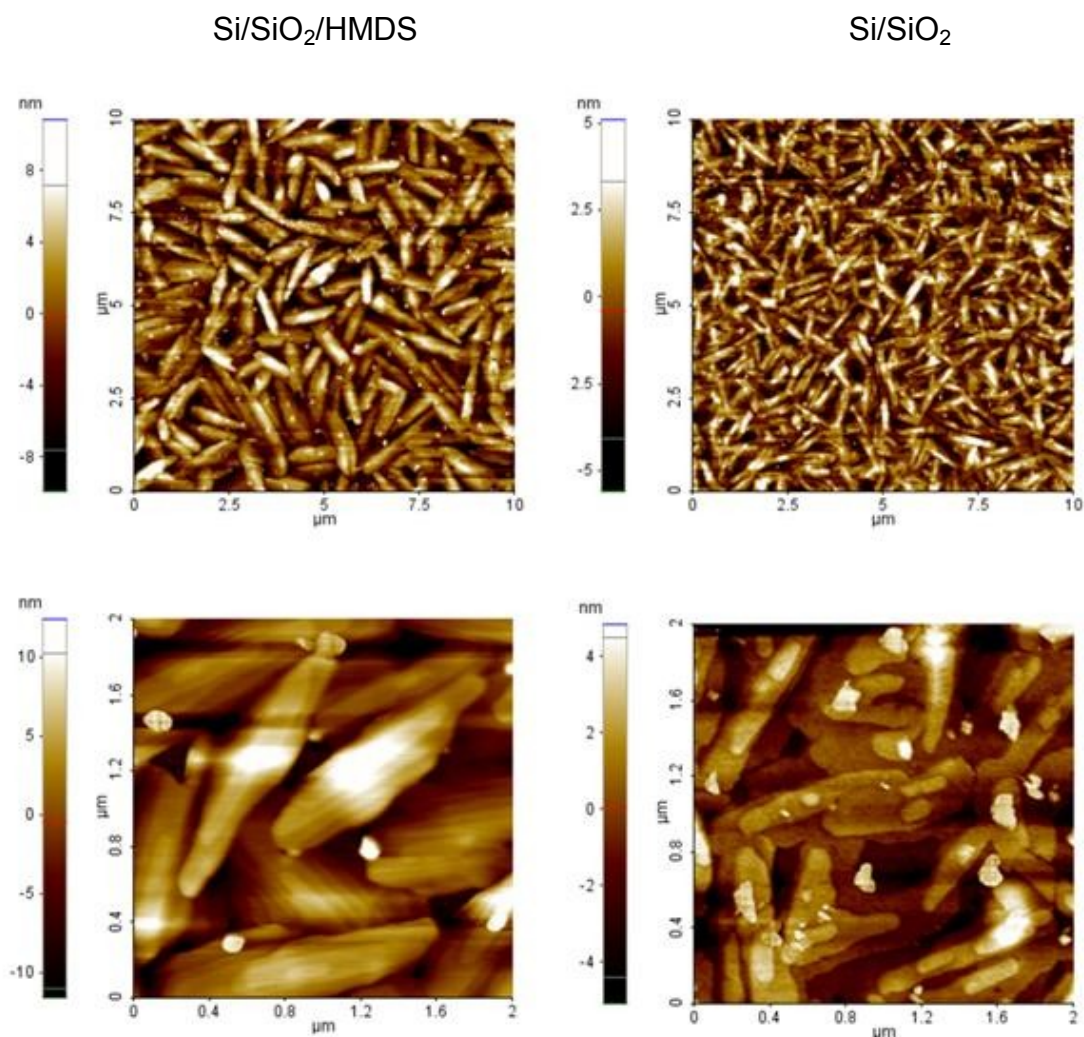


Figure 72: AFM images of TDZ-C13 films obtained by thermic evaporation.

The average grain size of the functionalized substrate is greater than one bare, but these islands seem more separate, furthermore the average surface roughness of the functionalized substrate is greater (thickness film of 20 nm with roughness of 4 nm) than

one bare (2 nm). In fact TDZ-C13 film is constituted by islands better connected and with squared line. These morphological differences appear to affect the electrical response (see Table 13).

Regarding TDZ-ST, the AFM images show that the films obtained by thermic evaporation on functionalized and bare substrates are quite similar (AFM images of the film obtained on functionalized substrate is reported in Figure 73). The films show the presence of columnar structures with height of 30-40 nm and an area of 100-200 nm².

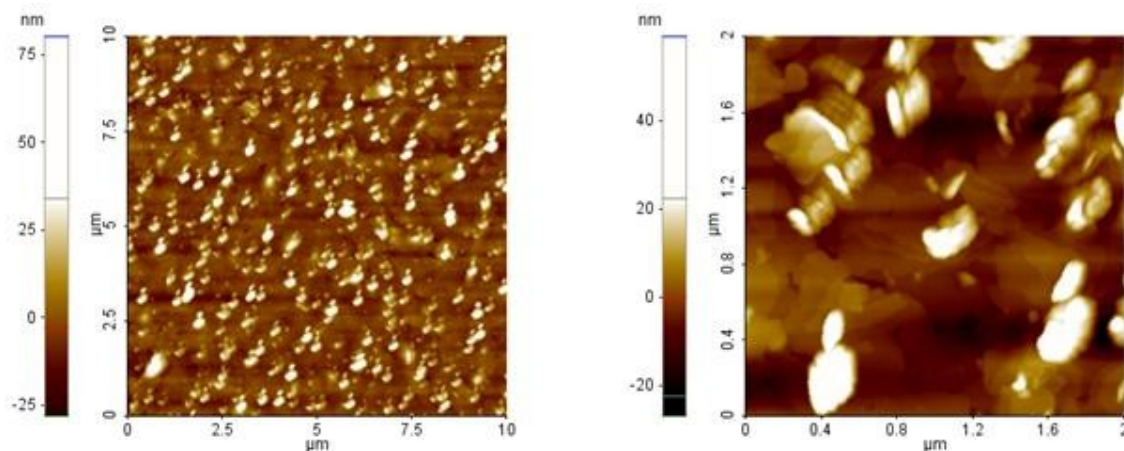


Figure 73: AFM images of TDZ-ST film obtained by thermic evaporation on functionalized substrate.

This type of morphology leads to an average surface roughness up to 10 nm (with thickness of 20 nm). Furthermore it is possible to observe the presence of circular islands around the columnar structures. On the base of the such considerations, we can affirm that the films are partially amorphous.

The films obtained by solution (5 mg/ml in 1,2-dichlorobenzene) via spin-coating are reported in Figure 74.

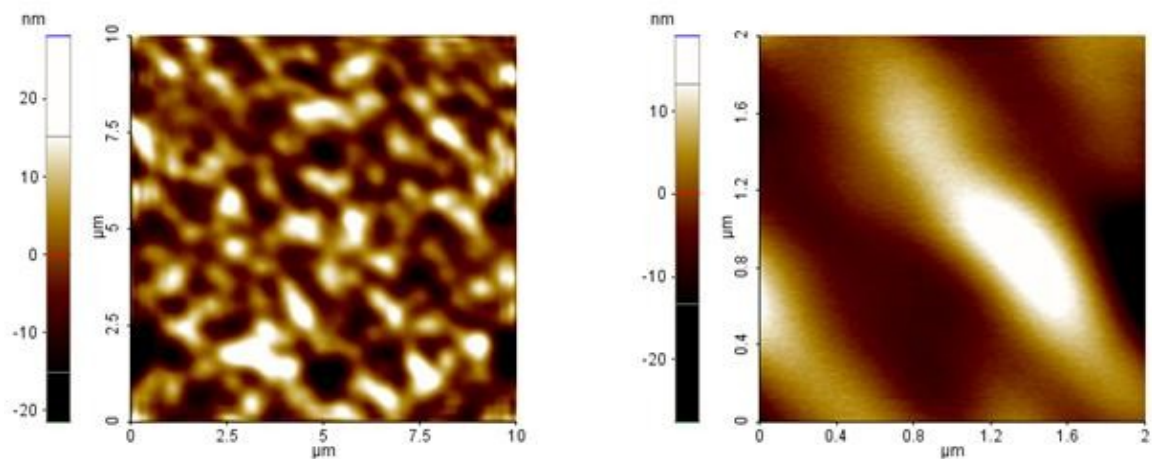


Figure 74: AFM images of TDZ-ST film obtained by spin-coating on functionalized substrate

The films seem amorphous, with corrugated surface. In this case the average surface roughness is 10 nm (with thickness of 90 nm).

The measurements and AFM images were carried out in the laboratories of the Physics Department, University of Naples “Federico II” (Italy), Research Group of Prof. Antonio Cassinese.

5 OPTOELECTRONIC AND ELECTRICAL PROPERTIES INVESTIGATION OF PT8-Cu(Ald1) AND TDZ-C7 AS DONOR AND ACCEPTOR MATERIALS IN SOLAR ORGANIC CELLS

5.1 Introduction

In principle, the optimization of organic solar cell is based on fine-tuning of the electronic properties and interactions of the donor and acceptor components so to absorb more light, generate the greatest number of free charges, with minimal concomitant loss of energy, and transport the charges to the respective electrodes at a maximum rate and a minimum of recombination.

Starting from these considerations, We have decided to investigate the optoelectronic and electrical properties of PT8-Cu(Ald1) TDZ-C7 for their possible application, respectively as donor and acceptor materials in a heterojunction solar cell.

5.2 Chemical-Physically Characterizations

Preliminary analysis were carried out through cyclic voltammetry (CV) in combination with UV-Vis optical absorption spectra in order to estimate molecular frontier orbital levels and E_g values of PT8-Cu(Ald1) and TDZ-C7.

We have performed CV measurements on thin film, using acetonitrile- NaClO_4 as electrolytic solution and the redox data were standardized with Ag/AgCl couple. Cyclic voltammograms of PT8-Cu(Ald1) and TDZ-C7 are shown in Figure 75. Frontier orbital level energies were obtained from onset of oxidation and reduction peaks (values indicated by arrows onto voltammograms of Figure 75).

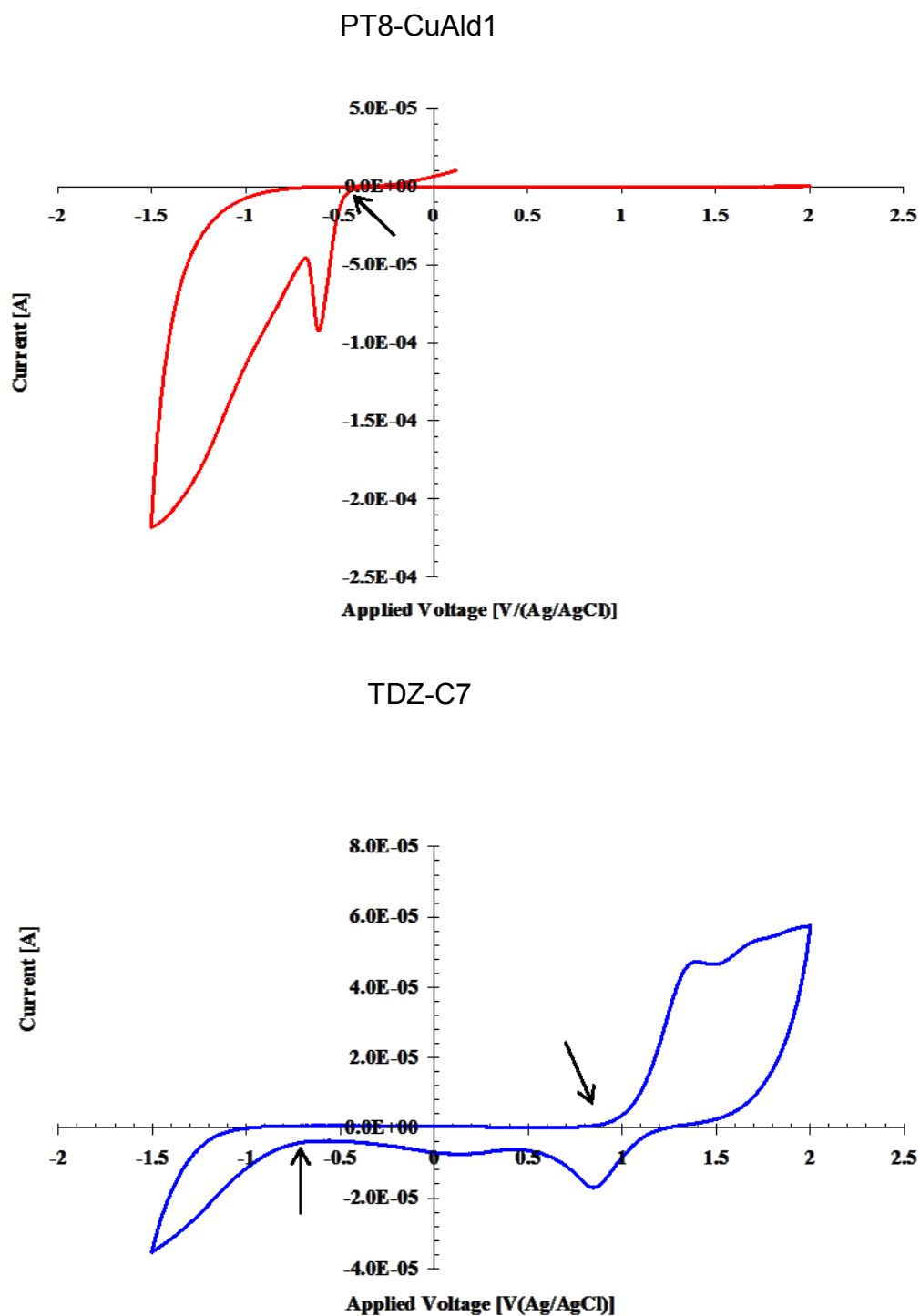


Figure 75: Cyclic voltammograms of PT8-CuAld1 and TDZ-C7.

From the CV trace it was possible to estimate the HOMO and LUMO energy values of the materials under investigation as earlier discussed (using Equation 7 described in 1.4.5 Paragraph). In particular for PT8 a HOMO energy of -5.55 eV was derived from CV measurements and combining this result with the optical bandgap measured by UV-Vis analysis, the LUMO energy was estimated in 3.94 eV. For what concerns instead TDZ-C7, since both a reduction and an oxidation process is observable in CV graphs, both HOMO and LUMO can be directly calculated and a value, respectively for HOMO and LUMO energy, of -6.52 and -4.30 eV was found.

Band-offset of a possible heterojunction is reported in Figure 76.

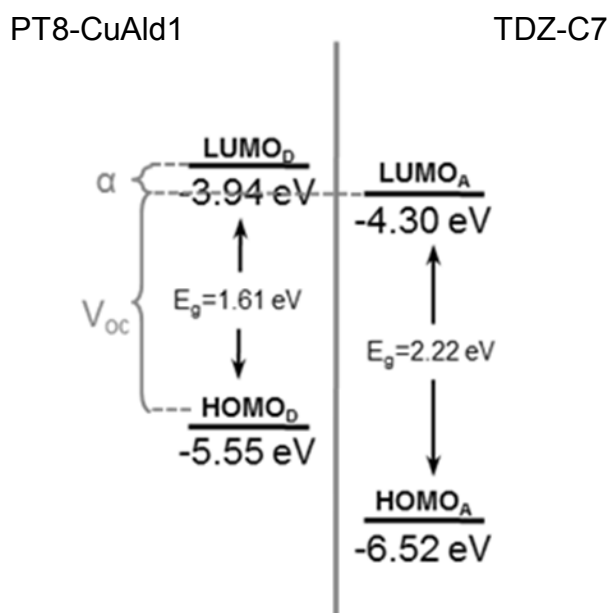


Figure 76: Energy diagram of the orbital frontiers belong to PT8-CuAld1 and TDZ-C7.

On the base of such preliminary investigation, we can assume that PT8 and TDZ-C7 are excellent candidate materials in order to assemble photovoltaic cells.

In fact, the first requirement concerning the electronic levels energy of possible donors and acceptors in a heterojunction organic solar cell, is the fact that the donor must be capable of transferring charge to the acceptor material upon excitation. A downhill energetic driving force is necessary for this process to be favorable and this driving force must exceed the exciton binding energy. This binding energy is the Coulombic attraction of the bound electron-hole pair in the donor, and typical values are estimated to be 0.4–0.5 eV. It appears that a minimum energy difference of 0.3 eV [34] is required to affect the exciton splitting and charge dissociation, thus the value of $\alpha = 0.36$ eV owned by our system is compatible with dissociation energy of exciton.

There are other two important parameters to be considered in the choice of materials for the fabrication of an efficient organic solar cell. First, the used materials should be capable in a wide range of the solar emission spectrum. One limitation of P3HT is for instance an optical bandgap of ~ 1.9 - 2.0 eV and thus a bad overlap with the low energy zone of the solar spectrum. One strategy to increase the efficiency is therefore to use low bandgap organic materials to better match solar spectrum [62]. With a E_g of about 1.61 eV, PT8 is definitely an interesting material to be used in this context. The second strategy followed in the recent works is to use donor materials characterized by a low lying HOMO level [63]. This in turn would allow a higher theoretical V_{oc} that has been proved to be dependent from the energy difference LUMO(acceptor)-HOMO(donor) [63], [64]. The HOMO energy measured for PT8 is low enough to make this material very appealing also in the

framework of this second strategy for increasing organic solar cells efficiency. To sum up, the electronic features of PT8 and TDZ-C7 indicate these materials as a very interesting couple of donor-acceptor materials for the fabrication of an organic heterojunction solar cell.

A optical characterization of film of PT8 and TDZ-C7 was successively carried out. This technique of thin film deposition was chosen to overcome the problem of low solubility affecting both the materials. In fact film are deposited from very diluted solution (in this case 1,2-dichlorobenzene was the solvent). Three different systems were prepared: a four LB layer structure of PT8 (PT8), a four LB layer structure of TDZ-C7 (TDZ) and a mixed structure composed by 4 LB layers of PT8 and 4 LB layers of TDZ-C7 (HJ, the PT8 films on the bottom). Uv-Vis and emission spectra are reported in Figure 77. Uv-Vis spectra confirms the good control on the thickness of the film obtained by LB technique since the spectrum of the mixed structure corresponds exactly to the sum of the 4 layers film of the single materials. TDZ shows a broad absorption between 430 nm and 600 nm, while PT8 shows a absorption maximum at 630 nm. When they are deposited together (HJ film) a broad absorption between 400 nm and 650 nm coinciding with the more intense part of the solar emission spectrum, condition highly desirable in a solar cell.

Emission spectra of TDZ and HJ (obtained through two excitation wavelength: $\lambda = 470$ and $\lambda = 570$ nm) show photoluminescence (PL) quenching of the 46% in the mixed film as compared to pure TDZ film. We have assumed that the quenching may be related with

energy transfer from TDZ-C7 toward PT8-(CuAld1). In fact there is a partial overlay of the absorption of PT8 PT8-(CuAld1) with emission spectrum of TDZ-C7.

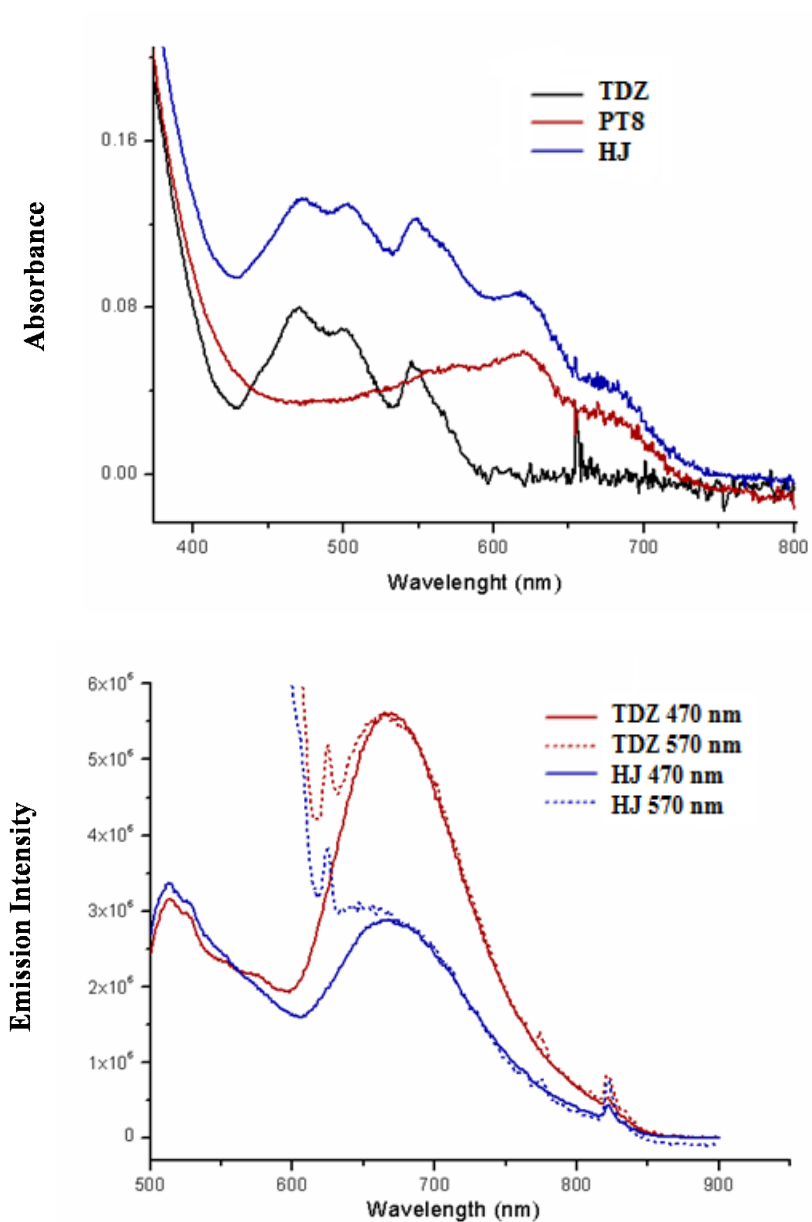


Figure 77: Absorbance and emission spectra of PT8(CuAld1) and TDZ-C7 film obtained by Langmuir-Blodgett method.

Furthermore such PL quenching indicates that efficient charge separation occurred at the PT8/TDZ interface, limiting the PL emission from the active layer. For organic photovoltaic devices, the separation of excitons into separated electrons and holes only occurs at the donor-acceptor interface. In the generally accepted mechanism, direct electron transfer from the donor to the acceptor occurs following the diffusion of the exciton to the donor-acceptor interface. However, another possible mechanism involves a Förster resonance energy transfer (FRET) from the donor to the acceptor after excitation, thus generating an exciton in the acceptor. Electron transfer from the donor to the acceptor by oxidation of the donor through the excited-state acceptor then leads to a free electron and free hole, if the difference between the HOMOs of the two components is sufficient to drive the charge transfer [34].

Therefore, the limited interfacial surface area of the abrupt and flat heterojunction can limit device efficiency because excitons generated are far from the interface recombine prior to dissociation. If the distance between conjugated polymer and acceptor material is larger than the exciton diffusion length, some excitons cannot reach a domain of n-material and subsequently recombine to give a PL signal. In contrast, a well-mixed heterointerface, ensures more-efficient exciton diffusion and charge separation. As the miscibility of the donor and acceptor increases, the size of the phase-separated domains decreases and the interfacial surface area between the two components is larger. The excited-state energy can, therefore, contribute to the photocurrent of the device instead of being emitted as a PL signal.

The measurements were carried out in the laboratories of the Chemical Department “S. Cannizzaro”, University of Palermo (Italy), Research Group of Prof. Bruno Pignataro and Dr. Sebastiano Cataldo.

6 CONCLUSIONS

The aim of this work was the synthesis and characterization of different classes of organic semiconducting materials using various types of synthesis strategy in order to realize electronic devices based on these organic semiconductors are employed as active materials, with respect to their properties.

In particular, the first part of the work dealt with the synthesis of a particular class of p semiconductor like polythiophenes 3-substituted by alkoxyphenilic and alkenoxyphenilic groups by adapting a particular synthetic methodology reported in literature [44], based on oxidative catalysis using vanadyl acetylacetonate ($\text{VO}(\text{acac})_2$) complex. We chose this synthetic procedure because it can be considered very simple and inexpensive if compared with Rieke [41] and McCullough [42] methods: in fact this method does not require any leaving groups or removal of the byproduct in the preparation of aromatic polymers, the procedure is very simple and it is possible to obtain regioregular polythiophenes with over 90% HT content. The choice of using alcoxy and alkenoxy-phenyl substituent on the polythiophene chain was taken in order to red-shift the polymer absorption as compared to the traditional P3HT. For what concerns the alkeneoxyphenyl substituent, they were moreover chosen with the idea of improving structuring and stability of polymers through the possibility of performing crosslinking reaction on film in different conditions.

The so prepared materials have been used as active layers in the fabrication of sensor devices for VOCs detection, in particular some of them were successfully used for detection of acetone, ethanol and toluene vapors. Such sensor devices have shown a linear

response of analyte concentration, good sensibility values, low detection limits and the efficiency device did not decrease even after three weeks of working.

Successively we have developed a new synthetic procedure in order to obtain poly[3-(4-alkoxyphenyl)thiophene]s with very high regioregularity. Thus such synthesis strategy was developed in order to realize polythiophenes that could be employed in a broader range of applications of the organic electronic, not only for application in organic sensors. In fact, increasing the regioregularity degree of this polymer class it is possible to improve their electrical properties, and to design photovoltaic cells where highly regioregular polythiophenes can be employed as active materials.

To achieve this goal, a deep investigation of the activity of different oxidation catalysts in alkoxyphenylthiophene polymerization was carried out. At the beginning, our research was addressed towards vanadyl complexes with different ligands but the results were not satisfactory. Successively several complexes were investigated to find a metal center able to catalyze regiospecific oxidative reaction between thiophene rings. In fact oxydant complexes of metals as Mn(II), Fe(II), Co(II), Ni(II), Nb(II) were employed in a wide range of conditions, but no one given satisfactory results. After a preliminary investigation of copper acetylacetonate catalyst, which did not afford interesting results, we finally develop a set of catalysts like Cu(Im), Cu(Ald1), Cu(Ald2) and Cu(Ald3) that gave excellent results. Thus we have optimized experimental condition through the variation of conditions in a wide range of experiments and deeply investigated regioregularity degree of the polymers obtained using both UV-vis spectra and $^1\text{H-NMR}$ analysis. As a result of such deep investigation, we found that a extremely high regioregularity can be obtained using

Cu(II) complexes, with a minimum of 96 % up to a maximum of 99 %. These values are significantly higher than the regioregularity obtained for the same polymers prepared by using VO(acac)₂ as catalyst and are comparable to the values reached by using the classical McCullough and Rieke methods for PAT's synthesis. Moreover it is possible to obtain highly regioregular poly[3-(4-alkoxyphenyl)thiophene]s through a very simple and inexpensive procedure: the step of monomer dibromination is in fact avoided and the employed catalyst is cheaper and not air sensitive so that a protected environment is not required.

An Italian patent request has been submitted for the this novel synthesis of poly-(3-(4-alkoxyphenyl)thiophenes) endowed with high regioregularity.

Finally we have carried out preliminary measurement of FET mobility and in particular the FET device prepared with PT8-Cu(Ald1) as active material, shown hole mobility up to $\mu = 1.0 \cdot 10^{-4} \text{ cm}^2 \text{ V}^{-1} \text{ s}^{-1}$. This mobility value is only one magnitude order lower than value shown by P3HT in both the same measurement conditions and device utilized.

The second part of the thesis work concerns about the synthesis of a new class of n-type semiconductor materials as PDI derivatives functionalized at the imide nitrogen with a thiadiazole and triazole group. In the latter case, by means of a double condensation reaction a molecule with an extended conjugation frame, as compared to classical PDI, have been obtained. We have developed this particular synthetic strategy because thiadiazole and triazole have electron withdrawing properties that can help in stabilizing, for inductive effect, the LUMO energy of the molecule.

Different PDI derivatives have been prepared, functionalized on the thiadiazole or the triazole with different alkyl tails some linear and the other swallow-tail like in order to increase the solubility.

The purity of the compounds was checked by elemental analysis, $^1\text{H-NMR}$ and MALDI mass spectrometry and all the data are consistent with the structure proposed for PDI derivatives.

A thermal analysis of all the molecules was carried out: no solid phase transition was detected neither melting point, being the compounds characterized by a decomposition temperature lower than melting temperature. The decomposition temperature were then determined by means of thermogravimetric analysis and in all the case a high thermal stability was found, with decomposition occurring beyond 300 °C.

PDI derivatives were moreover characterized for what concerns their emission properties: the thiadiazole derivatives presented a good photoluminescence quantum yield, up to 78 %. In the case of triazole derivative a lower quantum yield was measured (38 %) and a different emission pattern, less structured and more red-shifted. The synthesized PDI derivatives were used as active layers in the fabrication of organic thin film transistors: to avoid thermal degradation, the temperature set for the evaporation of the films was carefully chosen. The FET, characterized by a bottom contact configuration, feature SiO_2 as gate dielectrics or SiO_2 functionalized with a HMDS monolayer. The functionalization of SiO_2 gate dielectrics was performed in order to obtain a decrease charge carrier traps by shielding the conduction path from surface hydroxyl groups and tailoring the surface energy of the dielectric in order to control the molecular orientation, assembly, packing and film morphology of semiconductor layer. From the electrical characterization of the so

obtained transistors, carried out both in vacuum and air atmosphere, it was possible to determine the mobility of some of the materials under investigation in this thesis project.

Good mobility, up to $10^{-2}\text{cm}^2\text{volt}^{-1}\text{sec}^{-1}$, was measured for the evaporated thiadiazole derivative. The mobility was good both in air and in vacuum, suggesting a good ambient stability of the prepared materials. In one case, a transistor was prepared by depositing the active layer by solution technique (spin-coating) and also in this case a clear field effect was observed, and a mobility in the order of 10^{-5} was found. For what concerns transistors based on the triazole derivative, no field effect was observed probably because of the degradation of compound during evaporation process.

In the final part of thesis work, we have investigated the optoelectronic and electrical properties of PT8-Cu(Ald1) as donor and TDZ-C7 as acceptor materials in order to realize an heterojunction solar cell. Preliminary analysis were carried out through cyclic voltammetry (CV) in combination with UV-Vis optical absorption spectra in order to estimate molecular frontier orbital levels and E_g values of PT8-Cu(Ald1) and TDZ-C7. On the base of such preliminary investigation, we can assume that PT8 and TDZ-C7 are excellent candidate materials to assemble photovoltaic cells: the electronic levels are in fact positioned so that electron transfer from the acceptor (TDZ-C7) to the donor (PT8) is possible, the PT8 bandgap is very low and therefore a good matching with solar emission spectrum is obtained and finally, PT8, the possible donor material, feature a low lying HOMO energy (-5.55 eV) that is expected to have a positive influence on the V_{oc} of an actual solar cell device containing it and so on its overall efficiency.

In future, we will propose to improve further the new synthesis method of highly regioregular poly[3-(4-alkoxyphenyl)thiophene]s by using Cu(II) complexes in order to obtain higher yields. Moreover we will apply this innovative synthesis strategy in order to prepare polythiophenes 3-substituted with different groups that will can provide better conductivity performances in electrical device when will be employed.

Concerning n-semiconductor materials, we will synthesize new polymers using PDI derivatives functionalized with thiadiazole and triazole groups as monomers. In this way it will be possible to obtain new n-semiconductors that will own the remarkable electrical properties of the repetitive units whose are formed, and in addition these new polymers will hopefully show remarkable stability and processability in order to assemble OTFT devices. Moreover we will attempt to assemble a heterojunction solar cell when PT8-Cu(Ald1) as donor and TDZ-C7 as acceptor materials will be employed.

7 REFERENCES

- [1] A. Operamolla, G. M. Farinola, *Eur. J. Org. Chem.*, **2011**, 423-450.
- [2] S. R. Forrest, M. E. Thompson, *Chemical Reviews*, **2007**, 107, 4.
- [3] A. Pochettino, *Atti. Reale Accad. Lincei*, **1906**, 1, 355.
- [4] M. Volmer, *Ann. Phys.*, **1913**, 40(4), 775-796.
- [5] W. G. Pfann., *J. Metals*, **1952**, 4(7), 747-753.
- [6] W. G. Pfann., *Science*, **1962**, 135(3509), 1101-1109.
- [7] K. H. Probst, N. Karl., *Phys. Status Solidi*, **1975**, A 27(2), 499-508.
- [8] R. G. Kepler., *Phys. Rev.*, **1960**, 119(4), 1226-1229.
- [9] M. Pope, H. Kallmann, P. Magnante., *J. Chem. Phys.*, **1963**, 38, 2042-2043.
- [10] M. Pope, C. E. Swenberg., "Electronic Processes in Organic Crystals and Polymers", Oxford University Press, New York, 2. edition **1999**.
- [11] C. K. Chiang, Jr. Fincher, C. R., Y. W. Park, A. J. Heeger, H. Shirakawa, E. J. Louis, S. C. Gau, A. G. MacDiarmid., *Phys. Rev. Lett.*, **1977**, 39(17), 1098-1101.
- [12] C. W. Tang., *Appl. Phys. Lett.*, **1986**, 48(2), 183-185.
- [13] J. H. Burroughes, C. A. Jones, R. H. Friend., *Nature*, **1988**, 335(6186), 137-141.
- [14] C. W. Tang, S. A. VanSlyke., *Appl. Phys. Lett.*, **1987**, 51(12), 913-15.
- [15] R. H. Friend, R. W. Gymer, A. B. Holmes, J. H. Burroughes, R. N. Marks, C. Taliani, D. D. C. Bradley, D. A. Dos Santos, J. L. Brédas, M. Logdlund, W. R. Salaneck., *Nature*, **1999**, 397, 121-128.

- [16] Alan Heeger, Alan G. MacDiarmid, Hideki Shirakawa, "Press Release: The 2000 Nobel Prize in Chemistry", Nobelprize.org. 4 Sep **2011**, Advanced Information.
- [17] Bowden, M., et al., *Advances in Chemistry*, American Chemical Society: Washington, DC, **1988**.
- [18] Bredas J. L., Street G. B., *Acc. Chem. Res.* **1985**, *18*, 309.
- [19] R.A. Marcus, *J. Chem. Phys.* **1956**, *36*, 966-979; *Annual Rev. Phys. Chem* **1964**, *15*, 155
- [20] S. Larsson, L. Rodriguez-Monge, *Int. J. Quant. Chem.* **1997**, *63*, 655.
- [21] X. Zhan, A. Facchetti, S. Barlow, T. J. Marks, M. A. Ratner, M. R. Wasielewski, S. R. Marder, *Adv. Mater.*, **2011**, *23*, 268-284.
- [22] Website: <http://www.brewerscience.com/products/cee-benchttop-products/cee-technical-information/spin-coater-theory/#scept1>
- [23] V. C. Goncalves, B. M. Nunes, D. T. Balogh, C. A. Olivati, *Phys. Status Solidi A* **2010**, *7*, 1756-1759.
- [24] A. Dodabalapur, *Materials Today*, **2006**, *9*, 4.
- [25] J. Zaumseil, H. Sirringhaus, *Chem. Rev.*, **2007**, *107*, 1296-1323.
- [26] "Introduction to organic electronic and optoelectronic materials and devices" S.-S. Sun, L. R. Dalton, CRC Press.
- [27] X. Zhan, A. Facchetti, S. Barlow, T. J. Marks , M. A. Ratner, M. R. Wasielewski, S. R. Marder, *Adv. Mater.*, **2011**, *23*, 268-284.
- [28] A. Hierlemann, R. Gutierrez-Osuna, *Chem. Rev.*, **2008**, *108*, 563-613.
- [29] J. Janata, M. Josowicz, *Nat. Mat.*, **2003**, *2*, 19-24.
- [30] R. A. Potyrailo, C. Surman, N. Nagraj, A. Burns, *Chem. Rev.*, **2011**, in press.

- [31] A. Moliton, J. M. Nunzi, *Polym. Int.*, **2006**, 55, 583-600.
- [32] A. C. Mayer, S. R. Scully, B. E. Hardin, M. W. Rowell, M. D. McGehee, *Materials Today*, **2007**, 10(11), 28-33.
- [33] H. Spanggaard, F. C. Krebs, *Solar Energy Materials & Solar Cells*, **2004**, 83, 125-146.
- [34] B. C. Thompson, J. M. J. Fréchet, *Angew. Chem. Int. Ed.*, **2008**, 47, 58-77.
- [35] C. Li, M. Liu, N. G. Pschirer, M. Baumgarten, K. Müllen, *Chem. Rev.*, **2010**, 110, 6817-6855.
- [36] Website: <http://pvcadrom.pveducation.org/CELLOPER/QUANTUM.HTM>
- [37] Sheldrick, G. M. SADABS, Program for empirical absorption correction, University of Göttingen, Germany, **1996**.
- [38] A. Altomare, M. C. Burla, M. Camalli, G. L. Cascarano, C. Giacovazzo, A. Guagliardi, A. G. G. Moliterni, G. Polidori, R. Spagna, *J. Appl. Cryst.* **1999**, 32, 115.
- [39] G. M. Sheldrick, SHELX-97 University of Göttingen, Germany, **1997**.
- [40] M. Barra, M. Biasucci, A. Cassinese, P. D'angelo, A. C. Barone, A. Carella, A. Roviello, *J. Appl. Phys.*, **2007**, 102, 093712.
- [41] T. A. Chen, X. M. Wu, R. D. Rieke., *J. Am. Chem. Soc.*, **1995**, 117, 233.
- [42] R. D. McCullough, *Adv. Mater.*, **1998**, 10, 93.
- [43] M. Ganström, K. Petritsch, A. C. Arias, A. Lux, M. R. Andersson, R. H. Friend, *Nature*, **1998**, 395, 257-260.
- [44] T. Hayakawa, K. Fukukawa, M. Morishima, K. Takeuchi, M. ASAI, S. ANDO, Ueda, *Journal of Polymer Science: Part A: Polymer Chemistry*, **2001**, 39, 2287-2295.
- [45] R. D. McCullough, R. D. Lowe, M. Jayaraman, D. L. Anderson, *J. Org. Chem.* **1993**, 58, 904-912.
- [46] J. H. Kim, S. Y. Ban, S. Kaihua, D. H. Choi, *Dyes and Pigments*, **2003**, 58, 105.

- [47] Y. Sasada, Y. Shibasaki, M. Suzuki, M. Ueda, *Polymer*, **2003**, 44, 355-360.
- [48] U. Caruso, A. Roviello, A. Sirigu, *Liq. Crystals*, **1990**, 7, 431.
- [49] M. A. Sato, H. Morii, *Macromolecules*, **1991**, 24, 1196-1200.
- [50] A. Roviello, L. Ricciotti, F. Borbone, G. Roviello, A. Carella, *Italian Patent Request n NA2011A000030*.
- [51] W. Herbst, K. Hunger, *Industrial organic pigments*, 3rd completely revised edition, Wiley WCH, Weinheim, **2004**.
- [52] E. B. Faulkner, R. J. Schwartz, *High Performance Pigments*, second revised and expanded edition, Wiley WCH, Weinheim, **2009**.
- [53] B. A. Jones, M. J. Ahrens, M. H. Yoon, A. Facchetti, T. J. Marks, M. R. Wasielewski, *Angew. Chem. Int. Ed.* **2004**, 43, 6363-6366.
- [54] M. Sadrai, L. Hadel, R. R. Sauers, S. Husain, K. Krogh Jespersen, J. D. Westbrook, G. R. Bird, *J. Phys. Chem.*, **1992**, 96, 7988-7996.
- [55] S. Chai, S.-H. Wen, K.-L. Han, *Org. Electron.*, **2011**, 12, 1806-1814.
- [56] A. T. R. Williams, S. A. Winfield, J. N. Miller, *Analyst*, **1983**, 108, 1067-1071.
- [57] W. H. Melhuish, *J. Phys. Chem.*, **1961**, 65, 229.
- [58] H. Ma, H.-L. Yip, F. Huang, A. K.-Y. Jen, *Adv. Mat.*, **2010**, 22, 1-15.
- [59] P. Fontaine, D. Goguenheim, D. Deresmes, D. Vuillaume, M. Garet, F. Rondelez, *Appl. Phys. Lett.*, **1993**, 62, 2256.
- [60] A. R. Murphy, J. M. J. Fréchet, *Chemical Reviews*, **2007**, 107 (4), 1066-1096.
- [61] B. A. Jones, M. J. Ahrens, M-H Yoon, A. Facchetti, T. J. Marks, M. R. Wasielewski, *Angew. Chem. Int. Ed.*, **2004**, 43, 6363-6366.
- [62] J. Hou, H-Y Chen, S. Zhang, R. I. Chen, Y. Yang, Y. Wu, G. Li, *J. Am. Chem. Soc.* **2009**, 131, 15586-15587.
- [63] X. Zhan, D. Zhu, *Polym. Chem.*, **2010**, 1, 409-419.

- [64] C. J. Brabec, A. Cravino, D. Meissner, N. S. Sariciftci, T. Fromherz, M. T. Rispens, L. Sanchez, J. C. Hummelen, *Adv. Funct. Mater.*, **2001**, 11, 374-380.

